UNIVERSITÉ DE NANTES
FACULTÉ DES SCIENCES ET DES TECHNIQUES

ÉCOLE DOCTORALE SCIENCES POUR L'INGENIEUR, GEOSCIENCES, ARCHITECTURE (SPIGA)

Année 2015

The Magnetic Field of Mercury as Measured by the MESSENGER spacecraft

Le Champ Magnétique de Mercure tel que Mesuré par la Sonde MESSENGER

THÈSE DE DOCTORAT
Discipline : Sciences de la Terre et de l'Univers
Spécialité : Planétologie

Présentée
et soutenue publiquement par

Joana S. OLIVEIRA

Le 1er avril 2015, devant le jury ci-dessous

Président	M. Antoine MOCQUET, Professeur, LPG Nantes, Université de Nantes
Rapporteurs	Mme. Mioara MANDEA, Physicienne (CNAP), CNES
	M. Michael PURUCKER, Chief Scientist, SGT Inc. at NASA/GSFC
Examinateur	M. Philippe CARDIN, Directeur de Recherche, ISTerre, Université Joseph Fourier

Directeur de thèse : M. Benoit LANGLAIS, LPG Nantes
Co-Encadrante de thèse : Mme. Ma Alexandra PAIS, Universidade de Coimbra
Invité : M. Hagay AMIT, LPG Nantes

Acknowledgments

À mes encadrants

Aos meus supervisores

To my supervisors

When I look back, I see how much I have evolved as a scientist. This has been possible because I had three excellent supervisors that guided me in the right direction to a successful PhD. I want to thank Benoit Langlais who took a gamble on me after an Erasmus internship during my masters for his words of encouragement during the four years. I also thank Alexandra Pais, because without her nothing of this would have been possible. She taught me that Planetology actually exists during my first steps on science as a bachelor student! I want also to thank Hagay Amit who accepted to take part on my supervision, giving always an interestingly different understanding of things.

À mon Jury de thèse

Ao meu júri de doutoramento

To my thesis jury

I want to thank Doctor Mioara Mandea and Doctor Michael Purucker to have accepted to be my external examiners and by reporting my dissertation. I also want to thank Doctor Philippe Cardin for being part of my jury. And finally, I thank Professor Antoine Mocquet who have accepted to chair the PhD defense jury.

Au Comité Suivie de Thèse

Ao Comité de Avaliação do Doutoramento

Merci à Erwan Thébault et à Antoine Mocquet pour votre suivi de mes travaux de thèse et pour votre disponibilité. Vos commentaires (parfois exigeants) m'ont permis d'évoluer comme scientifique!

Aux responsables des cours

Aos responsavéis das disciplinas

Pendant ma deuxième année de thèse j'ai eu l'opportunité de faire un monitorat. Cela m'a permis d'apprendre à transmettre mes connaissances. Je remercie donc Olivier Verhoeven, Sabrina Carpy (qui sait où son co-bureau cache ses chocolats !), Martin Sanchéz-Angulo et Olivier Grasset de m'avoir fait découvert le monde de l'enseignement.

Support Bureautique et Informatique

Secretariado e apoio informático

Merci à Isabelle Berthaud, à Marie-Claire Bréhier, à Stéphanie Beaunay, à Colette Boulard et à Sophie Parroco pour la gestion des différentes missions au long de ces années. Et du côté informatique à Eric Boeuf et Sébastien Guiffan même si mon clavier portugais pouvait perturber!

À mes co-bureaux

Aos meus colegas de gabinete

Je remercie pour les moments de complicité, partage et rigolade dans le B028 : Julien Monteux, Patrick Thollot, François Civet, Jean Charles Fedini, et finalement Elodie Brothelande. Ma culture française a bien augmenté grâce à vous tous!

À mes collègues de tous les jours

Aos meus colegas do dia a dia

Je remercie aussi les personnes qui ont contribué à la bonne ambiance autour d'un repas, d'un café, d'un verre, pendant les conférences ou même au tour d'un goûter (à 16h piles !). Tout d'abord à mes compagnons de thèse de ma promotion : Marine Gourronc qui a bien aidé à mon intégration en France (de même pour sa famille !), à Thibault Fougeroux, à Axel Lefèvre, à Klara Kalousova et à Philipe Cance. Et à tous les docs ou postdocs plus ou moins anciens : Adriana Oancea, Jonathan Besserer, Olivia Golle, Gaëlle Plissart, Melanie Drilleau, Zeneib Kassouk, Colleen Milbury, Mélanie Segard, Thomas Cornet, Patrick Thollot, Erwin Dehouck, Susan Conway, Téodolina Lopez, Ondrej Soucek, Delphine Nna Mvondo, Armelle Braud, Katia Pinheiro (não esquecendo do Bimbim e da Gal), Marion Nachon, Geoffrey Aertgeerts, Maïwenn Lothode, Boris Chauviré, Clémence Herny, Nadia Marounina, Alice Hazotte, Francesco Salese, Diana Saturnino, Filipe Terra-Nova, Mélanie Douarin, Méric Haugmard, Laetitia Le Deit, Marion Massé, Antoine Ba, Dorine Bouquet, Mathieu Bouffard, Bertrand Manhaval, Katerina Sladkova, Livia Kother, Camilo Arias Ruiz, Anaïs Schmitt et Antoine Triantafyllon. Finalement, je tiens à remercier Laurent Lenta et Rose-Marie Baland pour leurs discussions très intéressantes et sincères.

Aux "sportifs" du Touch rugby

Aos desportistas de Touch rugby

Aux gens bien motivés pour bouger autour d'un ballon pas rond : Susan Conway, Erwin Dehouck, Benjamin Guillaume, Mélanie Drilleau, Thomas Cornet, Colleen Milbury, Patrick Thollot, Philippe Cance, Olivier Bollengier, Thibault Fougeroux, Olivier Jaffrezic, Boris Chauviré, Ianis Gaudot, Fany Belhadjar, Diana Saturnino, Jassin Petersen, Marion Nachon, Antoine Ba, Matthieu Bouffard, Romain Guyard, Alexis Bloch, Marine Gourronc, Livia Kother et Katerina Sladkova.

Au monde des Phasmes

Ao mundo dos insectos

Moi aussi je pensais que les insectes étaient des trucs moches, jusqu'au jour où Olivier Jaffrezic et Olivier Bollengier m'ont fait découvrir des bestioles tellement bien camouflées : "Une oeuvre d'art de la nature!" - je l'ai pensé! Je remercie aussi les gens avec qui j'ai partagé ma passion des Phasmes feuilles, notamment Nadia Marounina, Caroline Dumoulin, Alice Hazotte, et parfois Diana Saturnino, Clémence Herny et François Civet (même si obligés)!

Aux gens lusophones que j'ai pu rencontrer à Nantes

Às pessoas lusófonas que fui encontrando por Nantes

Conseguir matar saudades só pelo simples facto de se exprimir em português vale ouro, e por isso agradeço à Diana Saturnino, à Katia Pinheiro, ao Filipe Terra Nova (mesmo se o português dele fica muito aquém!), à Raissa Baldez e à Beatriz Funatsu!

Au laboratoire CITEUC à Coimbra au Portugal (deuxième labo de ma thèse)

Ao laboratório CITEUC em Coimbra (segundo laboratório da minha tese)

Nuno Peixinho, Teresa Barata, João Fernandes, Senhor Claudino Romeiro, Sara Carvalho, Tiago Abreu, Telma Esperança, Ricardo Gafeira, Alexandra Pais, Anna Morozova, Fernando Figueiredo, Fernando Pinheiro, David Vaz, Ana Andrade e Dra Adriana Garcia, agradeço o bom ambiente e bons momentos partilhados durante o mês que passei lá em missão. E à equipa em geral com as suas mensagens de apoio para a minha defesa! Regressar ao CITEUC é sempre uma sensação de regressar a casa!

Aux gens qui étaient toujours là, loin, de l'autre côté de mon écran ou du téléphone

Às pessoas que sempre estiveram lá longe do outro lado do meu écran ou telefone

Carina Fernandes pelas longas discussões ou apenas conversas "informativas" à distância, para ficar a par das novidades em Portugal! João Cunha (ou Eng Cunha para parecer importante) pela ajuda e apoio cruciais sobretudo no inicio desta aventura. Ivo Moreno pelo fornecimento de doces conventuais da sua região sem falha. Fernanda Fava pela simpatia e amizade. Luís Silva um elemento chave na minha carreira profissional mesmo se ele o desconhece (sim... a escolha do curso de Física foi muito repensada depois duma longa conversa contigo)! Majda Machraa pelo sorriso e bom humor e/ou feitio (!) sempre que a encontro. Miguel Machado e família pelas várias estadias em vossa casa (de 6 estrelas) para não perder o avião cedinho de manhã, e já agora ...Linha!! Solmaz Adeli pour le partage régulier des bons et mauvais moments (et pour tes conseils précieux de communication)!

Aux plus proches

Aos mais próximos

À minha família que torceu por mim e que bem me ajudou quando precisei. Às pequenas grandes atenções em termos culinários! À ma Belle-famille pour tout le support inconditionnel et leur bonne volonté. Et finalement, à Thomas pour m'avoir soutenue et écoutée pendant ma thèse, et pour avoir veillé à ce que tout se passe bien!

Contents

List of Figures

Resumé

L'étude du champ magnétique planétaire est l'un des moyens qui peut être utilisée pour contraindre la structure interne d'une planète. Toutes les planètes ne possèdent pas un champ magnétique global, interne et dynamique comme celui de la Terre. Des planètes telluriques, et en dehors de la Terre, seule Mercure a un champ magnétique global, qui a été découvert par la mission Mariner 10 en 1974.

Non seulement cette planète possède un champ magnétique, mais elle est caractérisée par d'autres propriétés atypiques. C'est la plus petite planète tellurique, avec un rayon de 2440 km. Elle a une densité très importante (5,3 g.cm^{-3}), à comparer à la densité de la Terre (4,45 g.cm^{-3}). Ceci est probablement dû à un très grand (en proportion) noyau métallique, avec des estimations récentes de l'ordre de 2000 km pour son rayon (soit plus de 80% du rayon de la planète). Son atmosphère est très ténue avec une densité de 10^5 atomes.cm^{-3}. Elle est constituée d'Hydrogène (H), Oxygène (O), Sodium (Na), Potassium (K) et Calcium (Ca), et interagit directement avec le vent solaire. Mercure est en résonance 3:2 autour du Soleil, ce qui signifie qu'elle effectue trois rotations sur elle-même alors qu'elle fait deux rotations autour du soleil (pendant ces deux années de Mercure, le soleil passe au-dessus de toutes les longitudes, ce qui correspond à un jour solaire). Sa surface est très caractérisé, indiquant une surface très ancienne, et présente des escarpements lobés, structures géologiques résultant d'une contraction de la planète.

En 2004 a été lancée la mission MESSENGER. Cet acronyme signifie MErcury Surface Space ENvironment GEochemestry and Ranging, ou Surface, Environnement Spatial, Géochimie et Télémétrie de Mercure). Cette mission a été conçue par la NASA. Les

objectifs scientifiques sont les suivants : déterminer la composition chimique de la surface de Mercure ; comprendre l'histoire géologique de la planète ; comprendre la nature de son champ magnétique ; comprendre l'état du noyau et en déduire sa taille ; observer les dépôts polaires pour en déterminer la composition ; comprendre les processus de couplage entre l'exosphère et la magnétosphère.

La phase de croisière a duré six années. Pendant cette phase ont eu lieu trois flybys (en 2008 pour les deux premiers et en 2009 pour le troisième). Des observations importantes ont été effectuées. Pour la première fois on a ainsi pu observer l'autre hémisphère de Mercure qui n'avait pas été vu par Mariner 10. Le champ magnétique de Mercure a aussi été mesuré, ce qui a confirmé les résultats des années 70. Anderson et al. (2008) ont estimé le moment dipolaire de Mercure, via un traitement du champ externe simpliste, et à partir des flybys de Mariner 10 et du premier flyby de MESSENGER. Ils ont obtenu une estimation dans l'intervalle de 230 à 290 nT.R_M^3 (soit environ 1% de celui de la Terre). L'accord avec les mesures est amélioré quand des termes quadrupolaires sont considérés, avec une intensité du quadrupole égale à 60% de celle du dipole. Purucker et al. (2009) ont par ailleurs conclu que le champ lithosphérique Hermean doit être faible.

La sonde s'est mise en orbite en mars 2011. Pendant la première année (terrestre) de la mission, l'orbite de la sonde a été très excentrique. Le périapse (point le plus bas de l'orbite) était à une altitude d'environ 200 km, alors que l'apoapse (point le plus haut) était à plus de 15000 km. La période résultant de cette orbite était de 12 heures. Une autre particularité est que le périapse était fixe en latitude, à 60 degrés nord. Cette configuration orbitale fait que la sonde traversait la magnétopause pendant chaque orbite, permettant ainsi d'observer les particules présentes dans l'exosphère.

La présence d'un champ magnétique global, d'origine dynamique, mais très faible, est une énigme en ce qui concerne le régime de dynamo capable de générer un tel champ. En effet, une simple loi d'échelle, en considérant un équilibre relatif entre force de Coriolis (liée à la rotation) et force de Lorentz (ou électromagnétique) prédit que le champ magnétique de Mercure devrait être deux ordres de grandeur plus grand. Différentes hypothèses ont été avancées. Une dynamo opérant dans une couche épaisse ou mince (Heimpel et al. 2005, Stanley et al. 2005), une dynamo opérant dans un noyau partiellement stratifié (Christensen et al. 2006), une dynamo gouvernée par une cristallisation du fer (Vilim et al. 2010), ou une dynamo contrôlée par un effet de feedback par le champ externe (Glassmeier et al. 2007). Toutes ces dynamos peuvent expliquent un champ faible à la surface de Mercure. Il existe des différences importantes entre ces hypothèses, et en particulier en ce qui concerne les caractéristiques spatiales et temporelles du champ magnétique produit et mesurable à la surface de Mercure.

Deux des scénarios les plus probables sont détaillés ici. La dynamo qui opère dans une couche fine du noyau peut produire un champ dipolaire (comme celui observé autour de Mercure) mais aussi un champ non-dipolaire (Takahashi and Matsushima, 2006). Ce type de dynamo est cependant associé des structures (à la surface de la planète) du champ localisées au dessus du cylindre tangent au noyau interne. En ce qui concerne la dynamo dans un noyau stratifié, le champ est plus simple en termes de structures présentes à la surface de Mercure. La couche liquide stable, présente au dessus de la zone de la dynamo au sommet du noyau, filtre les petites structures du champ, qui devient très zonal, axisymétrique, et varie très lentement dans le temps.

Les mesures (et les modèles dérivés de ces mesures) du champ magnétique de Mercure par la sonde MESSENGER devraient permettre de différencier les hypothèses avancées pour la dynamo de Mercure, et ainsi déterminer le régime de dynamo le plus probable. Les mesures de champ magnétique fournis par la sonde MESSENGER n'ont cependant qu'une couverture partielle, due à son orbite très excentrique. Les mesures permettant de caractériser le champ interne de la planète ne sont donc acquises qu'au dessus de l'hémisphère nord.

Les méthodes habituelles de modélisation mathématique du champ magnétique telles que les harmoniques sphériques (notamment utilisées pour décrire le champ magnétique de la Terre), ne sont pas les plus adaptées au cas de Mercure, à cause de la couverture partielle des mesures de MESSENGER. Il est nécessaire de considérer des méthodes alternatives, qui permettent de modéliser un champ magnétique interne et dynamique mesuré localement tout en limitant les effets de bord liés à la couverture spatiale.

L'objet de ce travail de thèse est de proposer, tester et appliquer une telle méthode. J'utilise pour cela les sources dipolaires équivalentes, ou Equivalent Source Dipole (ESD). Cette méthode a initialement été développée pour réduire à une altitude constante des mesures d'anomalie (c'est-à-dire d'origine crustale ou lithosphérique) du champ magnétique de la Terre. Le principe (simplifié) est le suivant : le champ mesuré en un endroit situé en dehors des sources crustales (donc en dehors de la planète) résulte de la contribution d'une distribution finie et homogène de sources d'aimantation (équivalente) crustale à une certaine profondeur. Cette méthode a été utilisée avec succès sur Terre, sur Mars et sur la Lune, et a permis de proposer les premières cartes à altitude constante du champ magnétique crustal de Mars (Purucker et al., 2000) ou d'estimer les variations latérales des contrastes d'aimantation (Langlais et al., 2004). Dans cette étude nous adaptons cette méthode en vue de modéliser un champ dynamique d'origine profonde et qui peut varier avec le temps. L'aimantation équivalente des dipoles peut donc avoir une composante temporelle, qui pour cette étude est linéaire (c'est-à-dire ressemblant à une variation séculaire constante). Les dipoles sont aussi placés à une surface plus profonde, pour mieux représenter le champ provenant du noyau. La nouvelle méthode est appelée sources dipolaires équivalentes temporellement variables, ou Time-Dependent Equivalent Source Dipoles (TD-ESD).

J'ai tout d'abord validé cette nouvelle approche en faisant plusieurs tests. Un modèle synthétique du champ de Mercure a été créé, basé sur un modèle terrestre et mis à l'échelle pour tenir compte de la plus faible distance au sources et de l'intensité plus faible du moment dipolaire de Mercure. Ce modèle a été utilisé pour prédire des mesures du champ magnétique, soit sur des grilles régulières à différentes altitudes, soit sur des orbites extraites des éphémérides de MESSENGER.

La performance de la méthode a été évaluée. Une résolution horizontale de 9.6° entre chaque dipole permet une bonne représentation des mesures tout en maintenant le coût computationnel à un niveau acceptable. Les résultats sont peu sensibles au choix de la profondeur exacte de la grille de dipôles lorsque celle-ci est proche de celle que nous avons utilisée pour mettre le modèle à l'échelle. Une profondeur de 640 km est choisie, mais d'autres profondeurs pourraient être aussi considérées.

L'intervalle d'altitude où le champ magnétique peut être modélisé vers le haut et vers le bas va de -300 à +1460 km lorsque les données sont acquises de manière idéale, c'est-à-dire sur une grille homogène à plusieurs altitudes. Pour une distribution plus réaliste, restreinte géographiquement, cet intervalle devient +10/+970 km. Un résultat important est que cette méthode permet de bien modéliser le champ magnétique dans la région où les données sont disponibles (i.e., l'hémisphère nord), avec des effets de bord qui restent limités. La limite sud de fiabilité du modèle est de 7° N pour les orbites considérées (cette limite dépend de la géométrie de l'orbite, qui varie dans le temps). Cependant, les tests réalisés démontrent que la modélisation de la variation temporelle est difficile voire impossible dans le cas considéré (deux jours sidéraux séparés par une année terrestre).

La méthode est appliquée aux mesures de MESSENGER. Pour ne sélectionner que les mesures pertinentes (quand le champ interne domine le champ externe), j'ai défini un analogue ou proxy du champ externe, basé sur le contenu fréquentiel du signal mesuré, et limité par une altitude maximale fixée à 1000 km.

Une première application de la méthode est faire aux quatre premiers jours sidéraux des mesures MESSENGER (correspondant à 235 jours terrestres, ou plus de 2,66 années de Mercure). Deux types de modèles sont considérés. Tout d'abord, quatre modèles basés sur les quatre jours sidéraux de Mercure sont calculés. Puis un modèle moyen, basés sur les trois premiers jours sidéraux, ou jour solaire.

Les modèles basés sur les jours sidéraux présentent un champ principalement axisymétrique. Cependant des petites échelles sont observées, qui varient d'un jour à l'autre en faisant une rotation autour de la planète. Ces petites échelles reviennent à des positions similaires le premier et le quatrième jour sidéral. Ceci est interprété comme étant très probablement d'origine externe. Lorsque le champ est modélisé en utilisant les mesures acquises pendant trois jours sidéraux successifs (c'est-à-dire pendant un jour solaire), ces petites échelles disparaissent presque totalement, ce qui confirme l'origine externe. Le champ magnétique de ce modèle basé sur un jour solaire est encore plus axisymétrique, avec un très petit rapport de champ non-zonal/champ zonal. Il montre également un équateur magnétique décalé dans l'hémisphère nord, ce qui est compatible avec d'autres études. Un résultat important est que le champ ainsi modélisé est de très grande échelle spatiale, alors que la méthode est faite pour pouvoir modéliser des petites échelles spatiales si elles existent. La méthode ne permet pas une séparation au sens propre des sources internes et des sources externes (elles ne sont pas prises en compte, mais leur effet - variable dans le temps - ne peut pas être modélisé), mais le champ obtenu est très zonal et de très grande échelle. Même si celui-ci peut être contaminé par quelques sources externes de grande échelle, il n'en reste néanmoins que le champ interne doit être lui aussi presque exclusivement zonal et de très grande échelle, ce qui constitue un challenge pour les modélisateurs de la dynamo herméenne. Ces travaux (test de la nouvelle méthode et application aux premières mesures de MESSENGER) font actuellement l'objet d'une publication en révision à Journal of Geophysical Research - Planets.

Dans un deuxième temps, j'ai traité l'ensemble des mesures MESSENGER disponibles, qui s'étalent sur 18 jours sidéraux (presque 3 années terrestres). Deux changements importants des paramètres orbitaux ont lieu. Tout d'abord la période a été réduite à 8 heures (en avril 2012) ce qui a pour conséquence que les données disponibles à moins de 1000 km d'altitude couvrent une zone géographique légèrement plus importante). Mais cet effet est contrebalancé par une migration vers le nord du périapse, ce qui a pour effet inverse de réduire la zone géographique des données disponibles à moins de 1000 km d'altitude. Le deuxième effet est plus important que le premier, et donc la zone couverte se réduit jusqu'au treizième jour, avec une latitude minimale proche de 30°N. Cette variation contraint fortement nos modèles et peut produire des effets de bords variables d'un modèle à l'autre.

Six modèles indépendants sont calculés, basés sur les six jours solaires successifs. Une forte variabilité est observée entre les différentes modèles. Le niveau de cette variabilité est très proche du champ magnétique externe de la magnétopause d'après Johnson et al. (2012). Il est probable que nos modèles contiennent toujours une partie variable relié au champ externe de grande échelle. Il n'est cependant pas possible pour l'instant de savoir si cette variabilité a une source externe ou interne (induite dans la planète par la source externe).

En conclusion, la méthode présentée des Time-Dependent Equivalent Source Dipole a été validée et appliquée aux mesures de la sonde MESSENGER autour de Mercure. Nos premiers modèles confirment un champ interne très axisymétrique et de grande échelle, avec un équateur magnétique situé au nord de l'équateur géographique. Nos modèles peuvent contenir un champ d'origine externe, bien qu'il soit difficile à quantifier. Des approches complémentaires doivent être envisagées, soit en tenant compte de sources externes pendant l'inversion, soit en estimant a priori le champ externe à partir de représentation alternative. Il reste néanmoins que notre méthode pourra être utilisée dans le futur, lorsque par exemple les mesures de la future mission BepiColombo seront disponibles.

Preface

Planetary magnetic field have been used as a tool for both practical purposes and fundamental research. During the early age of discovery by navigators in the XVth century, the geomagnetic field was used to find the route towards new lands. Nowadays, planetary magnetic fields are studied in order to understand the origin, formation and evolution of a planet, and to better characterize planetary internal structure and dynamics which generates it. The Earth is the perfect example of a planet where a magnetic field is sustained, but it is not the only one. With the advent of space missions, where most missions have a magnetometer onboard, new planetary worlds and cores have been investigated through the observation of their magnetic fields.

Possessing a planetary magnetic field of a dynamo origin is not a requirement for a planet. For instance, Venus, Mars and the Moon do not have a present active dynamo generating a planetary magnetic field. However, Mars and the Moon possess a crustal remanent magnetic field indicating that in the past dynamos existed on these bodies. Today, the Earth and Mercury are the only telluric planets of the Solar System that possess an active dynamo generating a magnetic field.

The geomagnetic field is by far the best measured field, spatially and temporally, thanks to ground observatories and satellites acquiring data on a regular basis. For the other planets, only spacecrafts have measured the magnetic fields, in relatively short time intervals compared to the Earth, often through flybys. Such flybys provided vital information on the magnetic field morphology of the Moon, Mars, Jupiter, Ganymede, Saturn, Uranus and Neptune. Mercury has been visited by the Mariner 10 spacecraft in 1974/75, which has revealed a planetary magnetic field of dynamo origin. Forty years later, the planet is revisited with an orbiting spacecraft called MESSENGER (MErcury Surface, Space ENvironment, GEochemistry, and Ranging).

The MESSENGER mission is orbiting Mercury since March 2011. Because of the particular eccentric orbit designed to protect the spacecraft from radiation, the magnetic field measurements are only acquired over the northern hemisphere. New methods that allow to model a magnetic field over a partial spatial coverage are required in this case. A method that models the magnetic field over one hemisphere is developed in this thesis. It is later applied to MESSENGER measurements, leading to new insights about the Hermean magnetic field including its internal core field.

In Chapter 1, I present an overview of Mercury's planetary characteristics, first as known before the current MESSENGER mission, and later the state of the art knowledge after its flybys. A particular emphasis is given to the evolution of the knowledge of Mercury's magnetic field. In Chapter 2, I review the different physical internal processes that were proposed to explain the weak magnetic field of Mercury. In Chapter 3, I outline the main goal of this thesis and introduce the new magnetic field modeling method over a limited coverage with a first application to MESSENGER's data. In Chapter 4, this method is applied to all MESSENGER measurements available in the moment of writing, leading to new insights about the Hermean magnetic field. I conclude this manuscript with a general conclusion and future work prospects.

Chapter 1

Mercury: From Mariner 10 to MESSENGER's flybys

In this chapter I present a brief overview of the state of the art knowledge of the first planet of our solar system. This includes the most important known global features, from the Mariner 10 mission and MESSENGER flybys. Only data and information from the Mariner 10 and MESSENGER flybys was available by the time I started my PhD thesis. Meanwhile, data from the orbiting MESSENGER spacecraft have become available and this thesis focuses on their analysis.

1.1 Pre-MESSENGER mission

Before the MESSENGER mission from which magnetic field measurements are used in my thesis, only Mariner 10 spacecraft and Earth's ground observations provided information on Mercury. It was thanks to the Mariner 10 flybys in 1974 and 1975 (Ness et al., 1974, 1975) that the idea of a completely frozen planet was abandoned. A very high mean density and a global internal magnetic field were discovered. The Hermean interior structure and evolution models had to be updated to explain these unexpected new features. New ideas to explain the very weak and probably global magnetic field were proposed since then. Consequently, the origin of Mercury's debate began.

1.1.1 Internal structure, dynamics, origin and evolution

The origin, evolution and magnetic field generation are linked to the internal structure. The knowledge of the Hermean interior comes from imaging the surface structures and through geodetic observations as the gravity field, rotation and tides (van Hoolst et al., 2007). A total mass of 3.302 $\times$ 10^{23} kg and a radius of 2439 $\pm$ 1 km were obtained from analysis of Mariner 10 Doppler data and radio occultation observations. These two quantities result in a mean density of 5.4 g cm^{-3} (Anderson et al., 1987), corresponding to an uncompressed mean density of 5.3 g cm^{-3} (Cameron et al., 1988). This is much higher than the uncompressed mean density of the Earth of 4.45 g cm^{-3} (Lewis, 1972), suggesting a silicate-to-iron ratio much smaller than those of the other terrestrial planets. In addition, the likely presence of sulfur in the core may lead to even smaller silicate-iron ratios (Harder and Schubert, 2001). Figure 1.1 shows the mean density as a function of the radius for all terrestrial planets, Moon and Io. Note that the mean density of Mercury is not typical for its actual size when comparing to the other planets, suggesting that Mercury contains a larger proportion of heavier elements. In addition, the Hermean surface gravity of 3.7 m s^{-2} is also high comparable to Mars'gravity value.

Only two gravity coefficients, J_2 and C_{22} can be inferred from Mariner 10 mission. These values are found to be small, suggesting that Mercury does not attain an hydrostatic equilibrium. Confirming this hypothesis, the ground-based radar ranging data suggests an equatorial elliptic shape. Moreover, results from libration and orientation of Mercury show evidence for a partially liquid core (Margot et al., 2007). A light alloying element such as sulfur should be present in the core, in order to lower the melting temperature with respect to that of pure iron. However, the sulfur concentration should be very low if Mercury planetesimals were formed at the actual Hermean orbit.

Mariner 10 surface imaging shows the presence of lobate scarps (Strom et al., 1975) that may be related to a radial contraction of about 2 km of the planet. This contraction

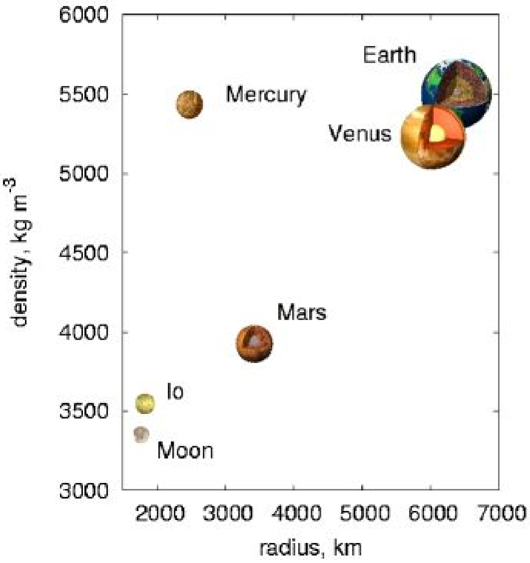

Figure 1.1: Planetary mean density as a function of radius for the terrestrial planets and Moons (from van Hoolst et al. (2007)).

may be linked to the inner core growth and mantle cooling. The Hermean mantle composition is unknown. Smooth plains that have morphological features consistent with lava are low in FeO. Assuming that lava composition is similar to that of the mantle composition, the latter has a very low FeO content.

In order to explain the anomalously high mean density of Mercury, different models often invoke processes of fractionation between iron and silicates during very early phases of the solar system formation. The removal of a large fraction of silicate mantle from the proto-Mercury by one or more giant impacts is one of the most interesting ideas to explain the high mean density of Mercury (Benz et al., 2007). A destructive collision is required in order to remove the mantle. The velocity of the impactor should be high enough for a violent impact, which is possible in regions near the Sun. After the impact, most of the ejected material remains in the proto-planet orbit, and may be reaccreted. But, the loss of ejected particles into the Sun due to the Poynting-Robertson effect (process by which solar radiation causes a dust grain to loose angular momentum) with time-scales of less than a few million years is shown to be more efficient than reaccretion.

1.1.2 Surface

The Mariner 10 cameras have allowed to image, with quiet good resolution, almost half of the Hermean surface during the three flybys. Only half of the Caloris basin (the most known morphological structure of the planet, an impact crater situated at the northern hemisphere) was captured by Mariner 10. The core and intercrater plains were formed 3.8 and 3.2 billion years ago, respectively. It is thought that the planet was no longer tectonically active after the intercrater plains formation.

The surface of Mercury is highly covered with impact craters (Murray et al., 1974) except for the vast smooth plains structures. The impact craters give important clues about the composition of the crust, mainly the complex crater peak or ring(s) constituted by underground material. The minimum diameter of a complex crater is 10.3 km for Mercury (Pike, 1988), which is higher than for the Moon (Pike, 1976) due to Mercury's higher gravity. The craters of Mercury show some differences compared to those of the Moon and Mars because of the gravity difference and because of the impactor velocity (which is higher close to the Sun).

Another surprise of Mariner 10 was the discovery of a scarp system extended over all the Hermean surface. At some locations, these scarps have cliffs of 1.5 to 3 km high. According to Strom et al. (1975) this scarp system indicates that Mercury had a period of contraction where the surface reduced about 31.000 to 63.000 km^2 corresponding to 1-2 km of diameter shrinking. This event occurred during the late heavy bombardment up to the smooth intercrater plains formation (Strom et al., 1975) and is evidenced by complex craters and plains traversed by scarps (Fig. 1.2-left). In addition, it is also characterized by a grid of lineaments of the different geological structures as scarps, ridges, valleys and linear portions of central peaks, extending from the Caloris basin to its antipode as shown in Figure 1.2-middle (Thomas et al., 1988). This is an evidence of a change in shape of the lithosphere due to tidal despinning (Melosh and McKinnon, 1988). However, some of these lineament structures do not seem to be associated to despinning but with a large-scale activity (Thomas, 1997). These features, principally the thrust faults, have been

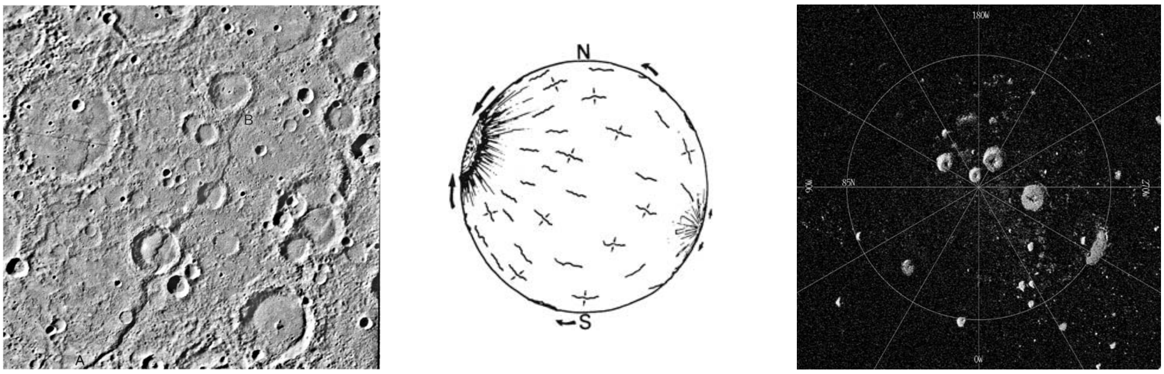

Figure 1.2: Lineament trends seen at Mercury's surface (Thomas et al., 1988) (left), surface seen by Mariner 10 during its third encounter (Strom and Sprague, 2003) (middle), and radar-bright regions at the north pole of Mercury as seen by ground-based radar imaging observations on August 14-15, 2004 (Harmon, 2007) (right).

used in models to estimate the elastic lithosphere thickness, leading to values of 40 to 125 km (Nimmo and Watters, 2004). In the same study, the thickness of the Hermean crust is estimated to be 125 to 140 km.

Hermean surface composition is accessed exclusively through ground-based observations, as Mariner 10 conducted no direct measurements of it. Mercury's surface has regions with rocks containing Na-rich feldspar with significant Mg-rich or Ca-rich pyroxene. The FeO content is very low at the surface but may be higher locally at small scales (see Sprague et al., 2007, and references therein). A new unexpected discovery was the presence of radar-bright features at the poles shown in Figure 1.2 (right). These features are inside craters and constantly shaded, and have specific scattering properties that are consistent with clean water ice or some other radar-transparent material such as sulfur or cold silicates (Harmon et al., 1994, 2001).

1.1.3 Atmosphere

Mercury's atmosphere is in fact a surface-bounded exosphere. It was discovered during the Mariner 10 mission through ultraviolet airglow and occultation experiments. The exosphere has a low density of 10^5 atoms/cm^3 (Broadfoot et al., 1976; Hunten et al., 1988). Mariner 10 ultraviolet airglow spectrometer detected neutral particles such as hydrogen

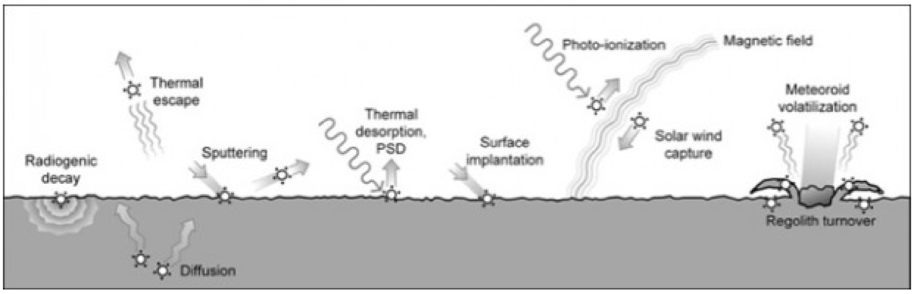

Figure 1.3: Different processes relating surface, exosphere and magnetosphere of Mercury (Domingue et al., 2007).

(H), helium (He) and oxygen (O) (Broadfoot et al., 1976). Later, from ground-based observations the elements of sodium (Na), potassium (K) and calcium (Ca) were also detected (Potter and Morgan, 1985, 1986; Bida et al., 2000). Moreover, ground-based telescopic observations show a strong variability of Na and K elements around Mercury, that depends on location, time and space weather. Na emission was observed to be greater in polar regions. In addition, there is a dichotomy of Na emission between the morning (where the emission is stronger) and evening side.

There are two possible sources for these exosphere particles: the solar wind and/or the Hermean surface, each maintained by different physical processes. The surface of Mercury is constantly exposed to the strong solar wind particles which are mostly protons and alpha particles (99% of ions) (Wurz and Blomberg, 2001). Many processes may occur between the solar wind and Mercury's surface as illustrated in Figure 1.3. The main source of heavy ions is the sputtering process, which consists in solar wind ions colliding with the Hermean atoms regolith, and ejecting them to the atmosphere. However, it is not clear if the source of Ca and O elements is the solar wind or Mercury's surface (Sprague et al., 2007). The exosphere particles may precipitate onto Mercury's surface being later reintroduced again in the exosphere.

1.1.4 Magnetic field measured by Mariner 10

Although the Mariner 10 spacecraft performed three flybys, only two of them were close enough to measure the weak internal magnetic field. Figure 1.4 shows the magnetic field measurements of the first and third flybys (M10-I and M10-III) and Table 1.1 summarizes the different characteristics of each. For each flyby, the crossings of the bow shock (BS) and magnetosphere (MP) were identified, as well as the planet's closest approach (CA). Figure 1.4 shows that the first flyby occurred during a disturbed period (see the less smooth curve near to the closest approach). It was attributed to a magnetospheric substorm during which an augmentation of energetic particles were detected (Siscoe et al., 1975). The BS and MP bounds correspond to a drastic change of the magnetic field intensity or/and vector direction. Figure 1.4 shows for both M10-I and M10-III smooth crossings, with the magnetic field nearly orthogonal to the shock normal. However, a very disturbed magnetic field is observed when the magnetic field lies almost parallel to the shock normal. For the first flyby the orthogonal and parallel configurations occurred for the inbound and outbound crossings, respectively (see Table 1.1). The inverse situation happened for the M10-III flyby. Notice that multiple BS crossings may occur (e.g. inbound BS of M10-I pass) because the boundary moves back and forth faster than the spacecraft velocity. Figure 1.5 show the magnetic field vector for these two flybys, when the spacecraft is inside the magnetosphere. The equatorial and polar flybys correspond to the first and second encounters of Mariner 10, respectively. The field vector of the first flyby shows a clear drop in intensity attributed to a magnetospheric substorm. The second flyby show a planetary dipole field behavior.

1.1.4.1 Magnetosphere

By definition, a magnetosphere is formed when a flow of charged particles, such as the solar wind, interacts with and is deflected by the intrinsic magnetic field of a planet or similar body. The solar wind conditions in Mercury are different than those in the Earth. The pressure of the solar wind at Mercury's magnetopause is expected to be around 5 to

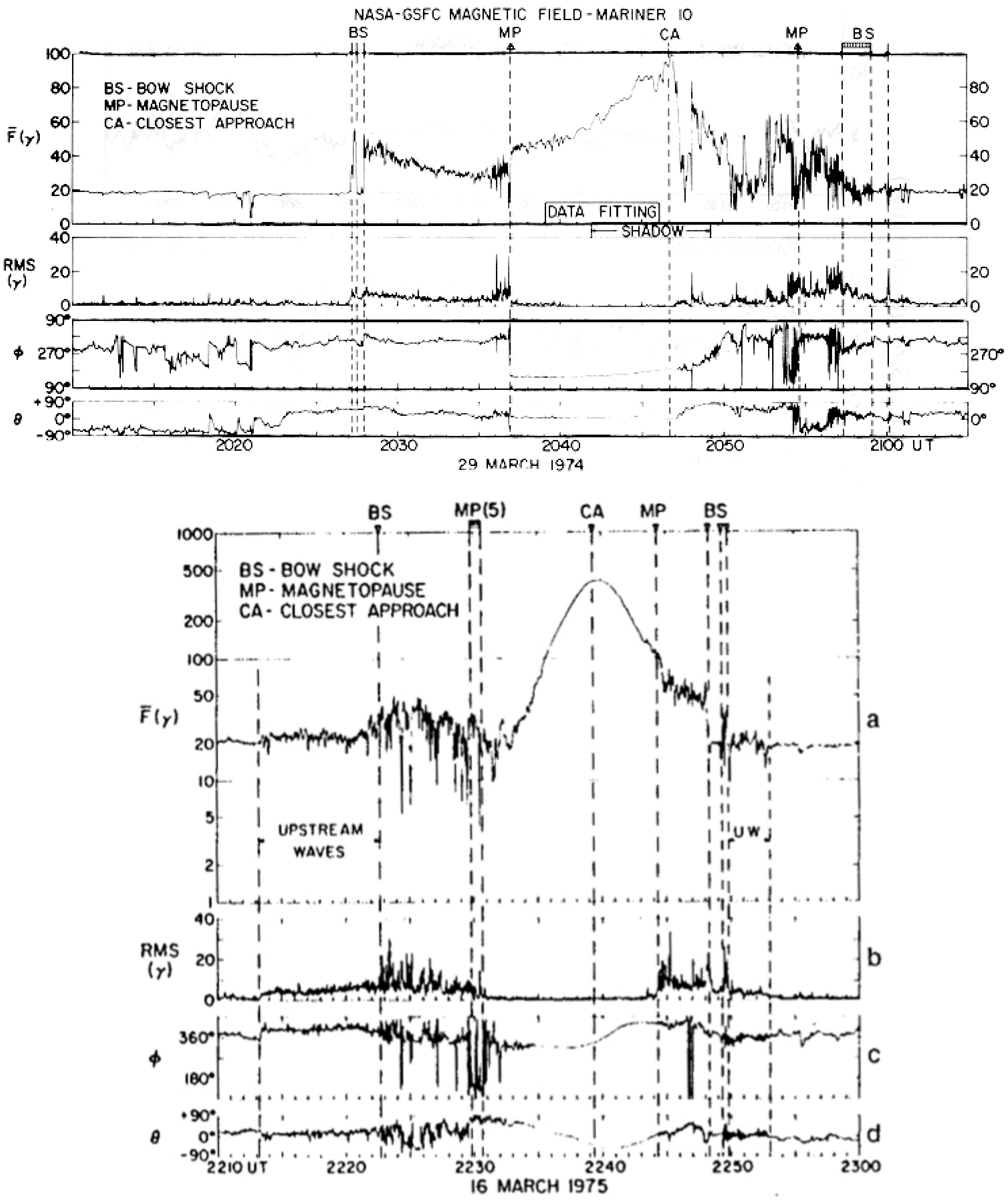

Figure 1.4: Mariner 10 magnetic field measurements during the first flyby (M10-I) on 29 March, 1974 (top) and during the third flyby (M10-III) on 16 March 1975 (bottom). For both figures, from top to bottom panels: magnetic field magnitude in nT, its standard deviation, ecliptic longitude of the field in MSO (0° is sunward, 90° is duskward), and ecliptic latitude (or polar angle, 0° is north, normal to Mercury's orbital plane). Vertical dashed lines indicate the bow shock (BS), the magnetopause (MP) and the closest approach (CA). UW denotes Upstream Waves. Figures from Connerney and Ness (1988).

Table 1.1: Magnetometer observations and orbit characteristics for Mariner 10 encounters the M10-I and M10-III (Connerney et al., 1982). BS denotes bound shock and CA the closest approach.

Feature	M10-I (29 March 1974)	M10-III (16 March 1975)
Interplanetary Field	$\sim$ 18 nT	$\sim$ 20 nT
BS inbound	$\sim$ perpendicular	$\sim$ parallel (upstream waves)
BS outbound	$\sim$ parallel (upstream waves)	$\sim$ perpendicular
CA altitude above surface	705 km $\simeq$ 0.29 R_M	327 km $\simeq$ 0.13 R_M
CA latitude	2°S	68°N
CA intensity field	98 nT	400 nT

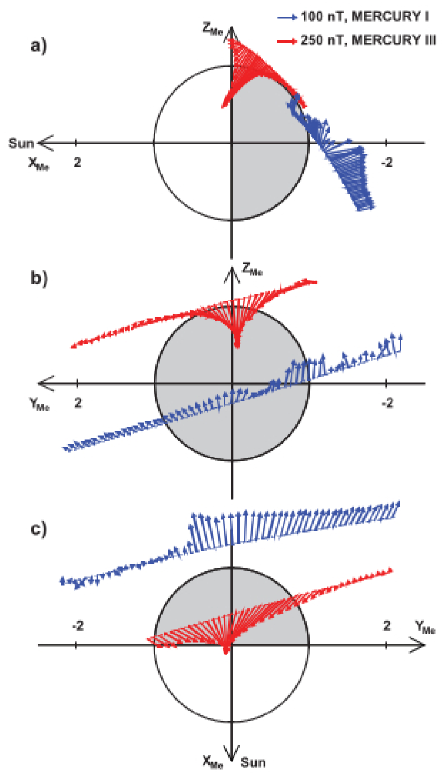

Figure 1.5: Magnetic field vector of Mariner 10 passages inside the Hermean Magnetosphere in MSO Cartesian coordinates, centered at the center of the planet. X coordinate is toward the Sun, the Z coordinate is parallel to the planet rotation axis, and the Y coordinate completes the right hand system (Wicht et al., 2007).

10 times larger than the Earth's due to the $1/r^2$ increase in plasma density, where r is the distance to the Sun. In addition, a very rarefied atmosphere gives rise to a different magnetosphere. In the Earth, neutral atoms from the atmosphere are ionized by the Sun and are affected by the magnetic field, and these same ions affect the magnetic and electric fields at the same time. The absence of a significant atmosphere on Mercury is expected to give rise to a different current system in the Hermean magnetosphere.

Models and extrapolations of BS and MP bounds were performed, despite a huge uncertainty of these bounds shape. Values for the subsolar magnetopause (where the sun's rays are parallel to the normal bound) distance of 1.35 $\pm$ 0.2 R_M and for the subsolar shock standoff distance of 1.9 $\pm$ 0.2 R_M were obtained (Ness et al., 1974; Russell, 1977). From the size of the magnetopause and magnetosphere detected by Mariner 10 spacecraft, a different dynamic magnetosphere compared to Earth's is inferred, with a reconfiguration timescale of the order of tens of seconds to a minute (Slavin et al., 2007). When normalized by the planetary radius, the Hermean magnetosphere size is a factor of 7.5 smaller than the Earth's. Figure 1.6 shows the Mercury planet scaled so that its magnetosphere occupy the same volume as the Earth's. For instance, the plasmasphere region and the energetic radiation belts probably would not exist on Mercury. The plasma sheet would almost touch the surface of the planet near midnight. Moreover, the polar cap field would be extended to lower latitudes on the night side.

1.1.4.2 Internal field

Internal magnetic field models were obtained from Mariner 10 magnetic field measurements. However, two main constraints limit severely their resolution: the strong external field variability and intensity and the lack of a continuous coverage of magnetic field measurements around Mercury. These main constraints certainly affect any internal model and render the models non-unique (Connerney and Ness, 1988).

Separating the external and internal contributions is challenging. In order to produce their internal models, many authors chose one of two ways: a selection of quiet data of

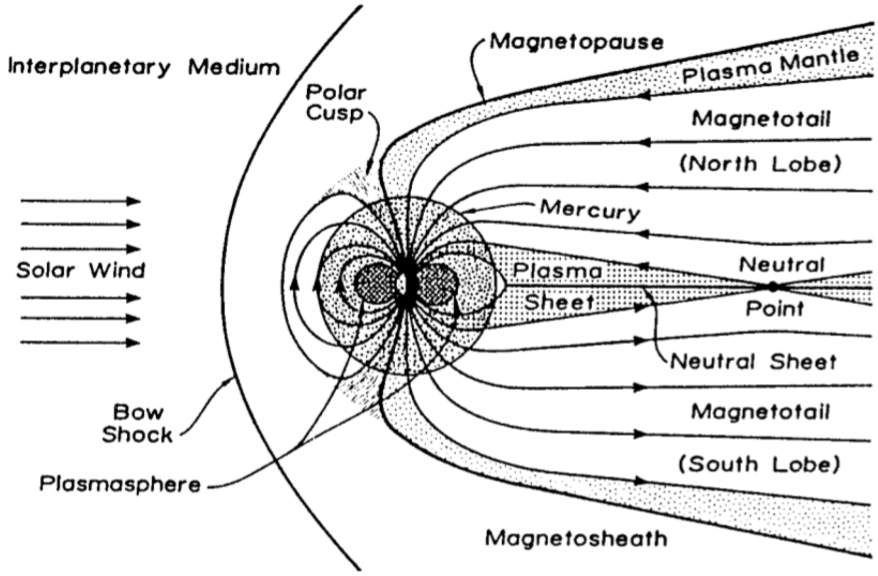

Figure 1.6: Planet Mercury scaled so that its magnetosphere has the same size as Earth's (Russell et al., 1988). The illustration is in a Noon-midnight meridian plane.

M10-I and M10-III, or only from the third pass (the quietest one); and/or to model the magnetosphere currents simultaneously with the internal field. It is common to describe the planetary magnetic field using Schmidt semi-normalized spherical harmonic coefficients g_n^m and h_n^m, the cosine and sine contributions of degree n and order m, respectively (Merrill et al., 1998). For the magnetic field of Mercury measured by Mariner 10, the internal field model parameters were often limited to an axisymmetric dipole (g_1^0) alone or an additional axisymmetric quadrupole (g_2^0), and rarely with an axisymmetric octupole (g_3^0). During the M10-III flyby the field has changed smoothly and significant higher order contributions seem unlikely at spacecraft altitudes. A displaced dipole along the rotation axis was also used as a model for the internal field, and in that case the model parameters are the dipole moment and the displacement distance. External field parameters, when modeled, were the parameters characterizing the Earth analog tail and/or magnetopause currents. Alternatively, the image dipole approximation was used, where the field of the magnetopause and current sheet are modeled (Whang, 1977).

Figure 1.7 shows internal field models obtained by different authors through different approximations. The dipole coefficient g_1^0 varies from -350 nT to -70 nT, and for those

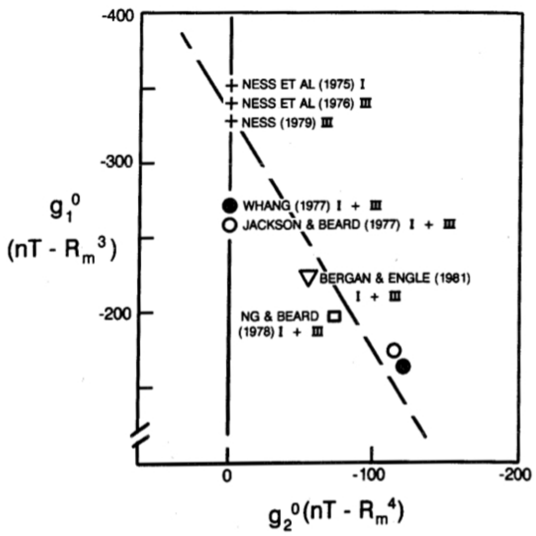

Figure 1.7: Estimated internal axisymmetric field dipole and quadrupole terms. Different symbols correspond to different authors identified in the Figure. Figure from Connerney and Ness (1988).

models with an axisymmetric quadrupole contribution g_2^0 varies from -120 nT to 0 nT (Connerney and Ness, 1988). Accounting for g_2^0 causes a reduction of the g_1^0 estimate by $\sim$80 nT.

1.2 MESSENGER mission

More than 30 years after Mariner 10, the MESSENGER spacecraft is presently in orbit around Mercury. This NASA mission, designed to better understand the structure and dynamics of the enigmatic innermost solar system's planet, has been acquiring data since 18 March 2011. MESSENGER's mission has six main scientific objectives consisting in characterizing (Solomon et al., 2001):

- the chemical composition of Mercury's surface;
- the planet's geological history;
- the nature of the Hermean magnetic field;
- the size and the state of the core;
- the volatile inventory at Mercury's poles;
- and the nature of Mercury's exosphere and magnetosphere.

In this Section I describe the spacecraft instruments. I give a special attention to the magnetometer (MAG). Finally I describe the mission design.

1.2.1 The spacecraft

The six scientific objectives listed above require a suite of instruments represented in Figure 1.8. The spacecraft include the Mercury Dual imaging System (MDIS), a Gamma-Ray and Neutron Spectrometer (GRNS), an X-Ray Spectrometer (XRS), a Magnetometer (MAG), the Mercury Laser Altimeter (MLA), the Mercury Atmospheric and Surface Composition Spectrometer (MASCS), the Energetic Particle and Plasma Spectrometer (EPPS), and the Radio Science (RS). The MDIS instrument includes a wide-angle (WA) and a narrow-angle (NA) imagers, the MASCS intrument includes an Ultraviolet-Visible Spectrometer (UVVS) and a Visible-Infrared Spectrograph (VIRS), and the EPPS instrument includes an Energetic Particle Spectrometer (EPS) and a Fast Imaging Plasma Spectrometer (FIPS).

In addition to this suite of instruments the spacecraft contains a telecommunications system. All the instruments are protected from sun particles and high temperature by a sunward sunshade. In addition all electronics, thermal accommodations, booms, brackets and cables are limited to 40 kg (Gold et al., 2001).

The primary scientific objectives of the magnetometer are: the study of the Hermean internal field structure and its interaction with the solar wind; the characterization of the geometry and time variability of the magnetospheric field. The magnetometer is a tri-axial fluxgate instrument. The instrument consists of an electronic box and a sensor mounted at the end of a deployable boom of 3.6 m (see Fig. 1.8). The distance between the sensor and the spacecraft is introduced to reduce measurements contamination by the intrinsic spacecraft field. In addition, the sensor has a small conical shade which is made of a non-magnetic material, in order to protect it from direct solar illumination. The magnetometer operates in two ranges: fine range of $\pm$ 1530 nT for each three orthogonal axes, with an accuracy of 3 nT or 0.2% of full scale; and a coarse range of $\pm$ 51300 nT that simplifies

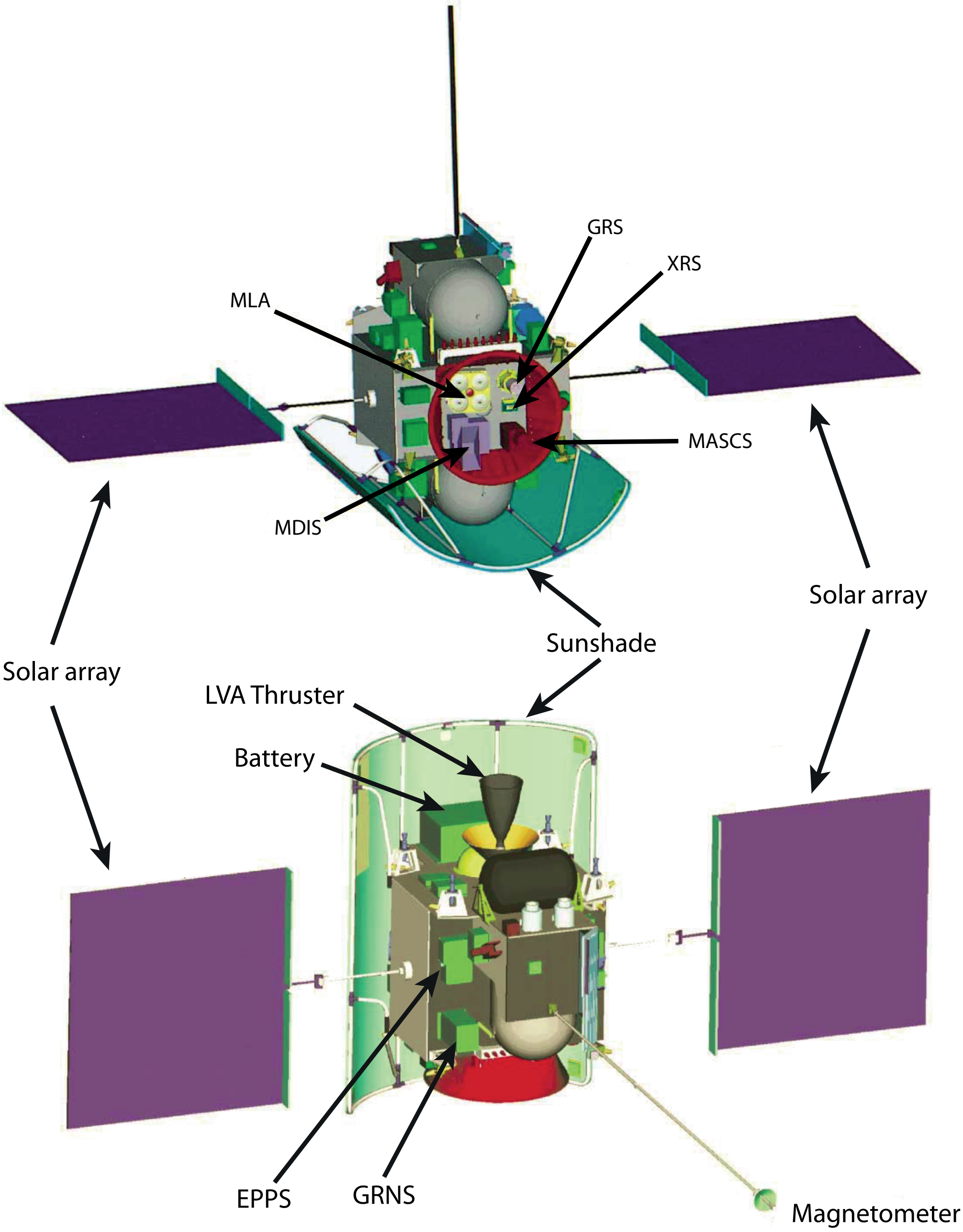

Figure 1.8: MESSENGER's payload (Gold et al., 2001; Santo et al., 2001). Two different views of the spacecraft are shown in order to identify the different instruments. The sunshade is always pointing towards the Sun. The magnetometer (MAG) is mounted on a 3.6-m boom in the anti-sunward direction (bottom Figure).

ground tests and operations in Earth field. In order to measure variable telemetry rates of the magnetosphere, magnetopause crosses and the internal field, the magnetometer may acquire samples with rates varying between 0.01 s^{-1} and 20 s^{-1} (Anderson et al., 2007).

Magnetic field measurements used in this thesis The magnetic field data used in this thesis are displayed by the NASA Planetary Data System, at http://ppi.pds.nasa.gov site. In addition, the data chosen is the MAG calibrated data in MSO and MBF coordinates system. As a NASA policy, the publication of the MESSENGER mission data has a delay of 6 months at least.

1.2.2 Mission design

After its launch at August 3, 2004, the MESSENGER spacecraft took more than 6 years to be in orbit around Mercury. During its journey the spacecraft encountered the Earth, Venus and Mercury for gravitational assists, reaching the good direction and velocity. Figure 1.9 shows the different phases during MESSENGER's cruise until the Mercury orbit insertion (MOI), including deep space maneuvers (DSM) and flybys. The three flybys around Mercury led to the first scientific data from the planet since the Mariner 10 mission. For instance, the unknown surface of the planet was mapped and the magnetic dipole moment was confined to a smaller range of possible values. Gravity models were also obtained from these flybys to better program the probe orbit insertion with lower risk.

1.2.2.1 Primary mission

During the primary mission MESSENGER had a very eccentric polar orbit with a 12h period (Fig. 1.10). Its minimum orbit altitude (periapsis) varied from 200 to 500 km with latitudes between 60°N and 74°N. Its maximum orbit altitude (apoapsis) was more than 15000 km. In addition, the inclination of the orbit varied between 82° and 84° resulting in a coverage hole around the north pole. The choice of this type of orbit was a compromise between scientific requirements and thermal constraints (Santo et al., 2001). Six orbit

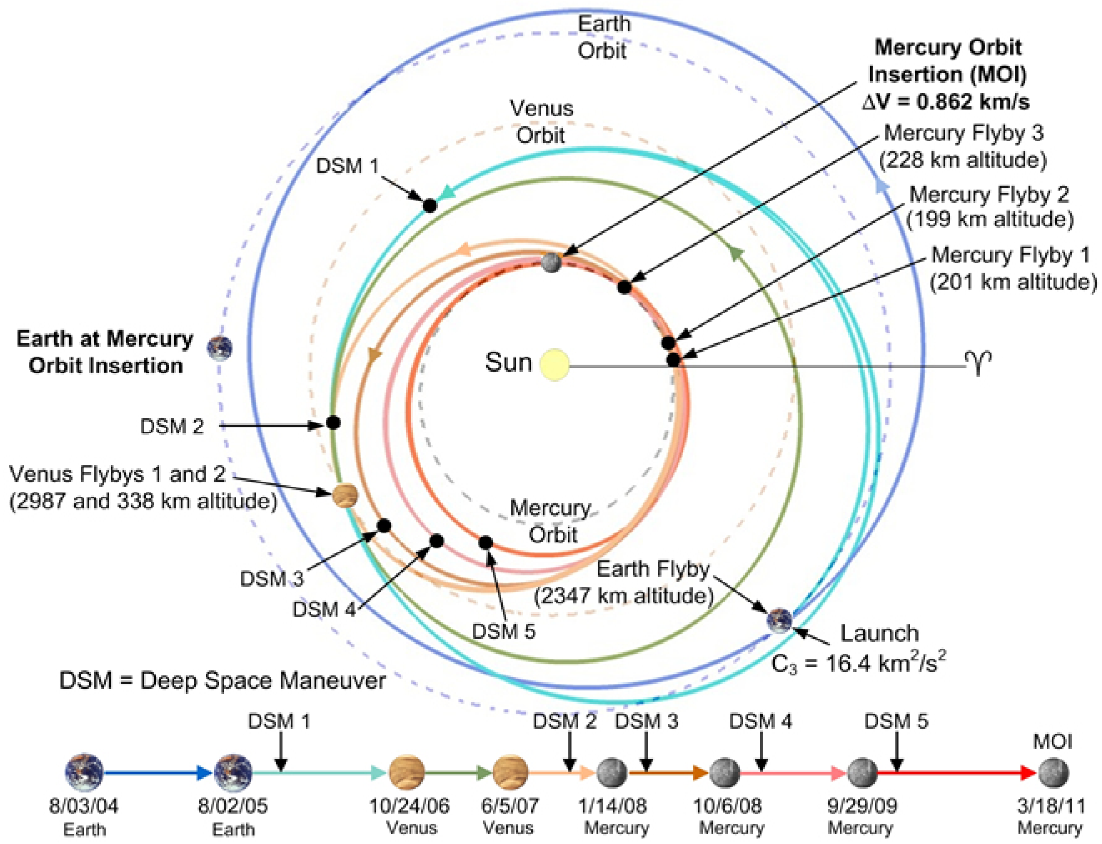

Figure 1.9: MESSENGER timeline since the launch to the MOI, specifying the many planetary flybys during its journey (O'Shaughnessy et al., 2014).

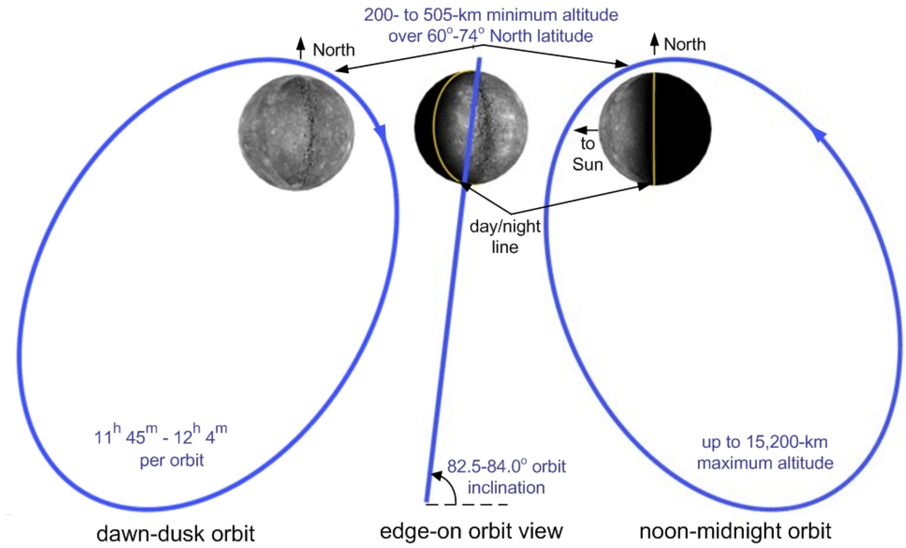

Figure 1.10: MESSENGER's primary mission orbit. The periapsis altitude varies from 200 to 500 km over 60° to 74° North latitude. The orbit period also varies from 11h45 to 12h04 time-periods. Figure from http://messenger.jhuapl.edu/.

correction maneuvers (OCMs) were needed in order to maintain the periapsis altitude and the orbit period. Table 1.2 shows the different OCMs applied during the primary mission, usually followed by a magnetometer turn off and consequently a gap of measurements or an abrupt altitude change.

1.2.2.2 Extended missions

The mission was initially programmed to acquire scientific measurements during one Earth year (corresponding roughly to two Herman solar days). The success of the long first year mission and the need for more data to accomplish the scientific objectives were a good justification for a mission extension. In addition, solar sailing technique developed and applied during the probe cruise saved propellant that can be used for a possible mission extension (O'Shaughnessy et al., 2014). Two mission extensions were programmed: the one year long extended mission 1 (XM1) and the two years long extended mission 2 (XM2). The XM1 started in march 2012 finishing one year later. One month after XM1 began, the spacecraft orbit period was reduced from 12h to 8h, maintaining the periapsis altitude range (OCMs 7 and 8). In the end of XM1 the probe reached a maximum

Table 1.2: List of orbit correction maneuvers (OCM) during all MESSENGER mission.

Maneuver	Calendar Date	Purpose
MOI	18 Mar 2011	Insert spacecraft into orbit around Mercury
OCM-1	15 Jun 2011	Lower minimum altitude to 200 km
OCM-2	26 Jul 2011	Increase orbit period to 12 hr
OCM-3	07 Sep 2011	Lower minimum altitude to 200 km
OCM-4	24 Oct 2011	Increase orbit period to 12 hr
OCM-5	05 Dec 2011	Lower minimum altitude to 200 km
OCM-6	03 Mar 2012	Lower minimum altitude to 200 km
OCM-7	16 Apr 2012	Decrease orbit period to 9.1 hours; deplete oxidizer
OCM-8	20 Apr 2012	Decrease orbit period to 8 hours
OCM-9	17 Jun 2014	Target 25-km minimum altitude on 12 Sep 2014
OCM-10	12 Sep 2014	Target 25-km minimum altitude on 24 Oct 2014
OCM-11	24 Oct 2014	Target 25-km minimum altitude on 21 Jan 2015
OCM-12	21 Jan 2015	Target 15-km minimum altitude on 1 Mar 2015
Impact	Mar 2015?	-

inclination of 84.1°N at its periapsis, and started the decrease of periapsis altitude until an eventual impact. The XM2 began in march 2013 and will finish in march 2015 when the spacecraft impact is expected. In addition, in 2014 MESSENGER also surprisingly observed two comets that passed near the planet, the Encke and the ISON comets. In the end of XM2, four OCMs to periapsis-altitude-raising purposes are planned. Figure 1.11 shows the periapsis altitude between the MOI until the impact. OCMs are also indicated. The periapsis altitude varies between 200 km and 500 km during almost all the mission time, except for the last 10 months when periapsis altitude is lower than 200 km. The periapsis latitude started at 60°N, then moved northward up to 84°N and it started moving southward reaching 58°N in the end. Table 1.2 also shows the list of OCMs applied during the extended missions.

1.3 Post-MESSENGER flybys

With MESSENGER flybys, knowledge about many of the topics concerning Mercury mentioned in the previous chapters has increased. Here I detail the advances achieved in the understanding of the Hermean internal structure and dynamics of its magnetic field.

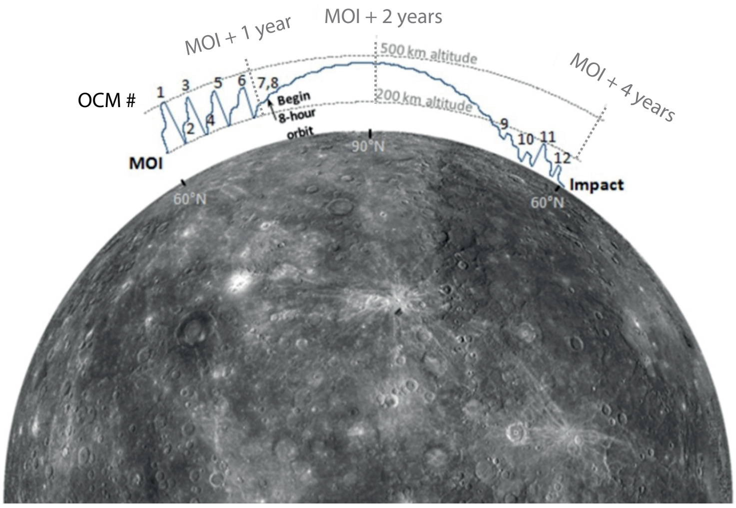

Figure 1.11: MESSENGER's periapsis altitude during the primary and extended missions. Orbit correction maneuvers (OCMs) are also indicated in the figure (McAdams et al., 2014).

1.3.1 Magnetic field measured by MESSENGER flybys

From the first (M1) and second (M2) flybys, there is evidence of a strong magnetospheric dynamics, namely Kelvin-Helmholtz vortices and boundary waves. These magnetospheric structures are also observed at Earth (Slavin et al., 2008). Intense signatures of reconnection during the magnetopause passages are detected, but are particularly strong during the M2 flyby. In this case, the flux transfer was intense in order to produce field signatures stronger than that from the planet's interior (Slavin et al., 2009).

Figures 1.12 and 1.13 show the magnetic field data and proton observations from FIPS instrument (see Section 1.2.1), for both flybys M1 and M2. Flyby M1 passed inside the magnetosphere at Mercury longitudes 0 to 90° and at an altitude of 200 km above the surface, while flyby M2 passed at longitudes 180 to 270° and at same altitude as M1. Both flybys have measured roughly the same maximum level of field intensity near the closest approach: 159 nT for M1 and 158 nT for M2, an indication of a weak dependence on longitude. For both flybys, a rotation of the field is observed from anti-sunward to northward (see φ) corresponding to the transition from the magnetotail lobe to the region dominated by the planet's internal field. This transition is denoted by TL. In addition, after the closest approach (CA) both flybys display a sharp drop of field magnitude, with nearly no change in the direction. This transition is used to localize the dayside boundary layer (denoted by BL). From this limit outward the planetary magnetic field is no longer dominating.

Information of proton observations helps to understand some features of the magnetic field through the interaction between the plasma and the magnetic field. For instance, from the proton data, the proton energy and counts change significantly in all magnetic field transitions. For flyby M1, the spacecraft remained in the tail plasma sheet until TL, because particles are very energetic. For flyby M2, few particles were detected before TL, suggesting that the spacecraft has entered directly into the southern tail lobe region where particles density is low. Moreover, spikes of magnetic field intensity are usually correlated with proton count rates increase, indicating that particles influence strongly the magnetic field environment even in the region close to the planet ($< 0.5\ R_M$) (Anderson et al., 2008). Consequently, the standard assumption that the volume near the planet is current free (e.g. Backus 1970) does not seem appropriate for Mercury (Anderson et al., 2010). MESSENGER flybys do not allow to access the plasma structure around the planet in detail, but they show indications that the plasma distribution is very different compared to those of other planets.

1.3.2 Internal field

As described before, the magnetosphere is not well known, but it produces external magnetic fields of tens of nT, comparable to the planetary field. It is required to make corrections of the external field in order to access the internal field structure, but uncertainties still remain quite large. Three approaches can be used to estimate the external field: potential field theory, analytical empirical models and physics-based simulations. The potential field formalism treats the external field in the same way as the internal field, except for its different radial dependence for sources outside the sampled region. The analytical empirical models are based on a priori defined current systems constrained empirically

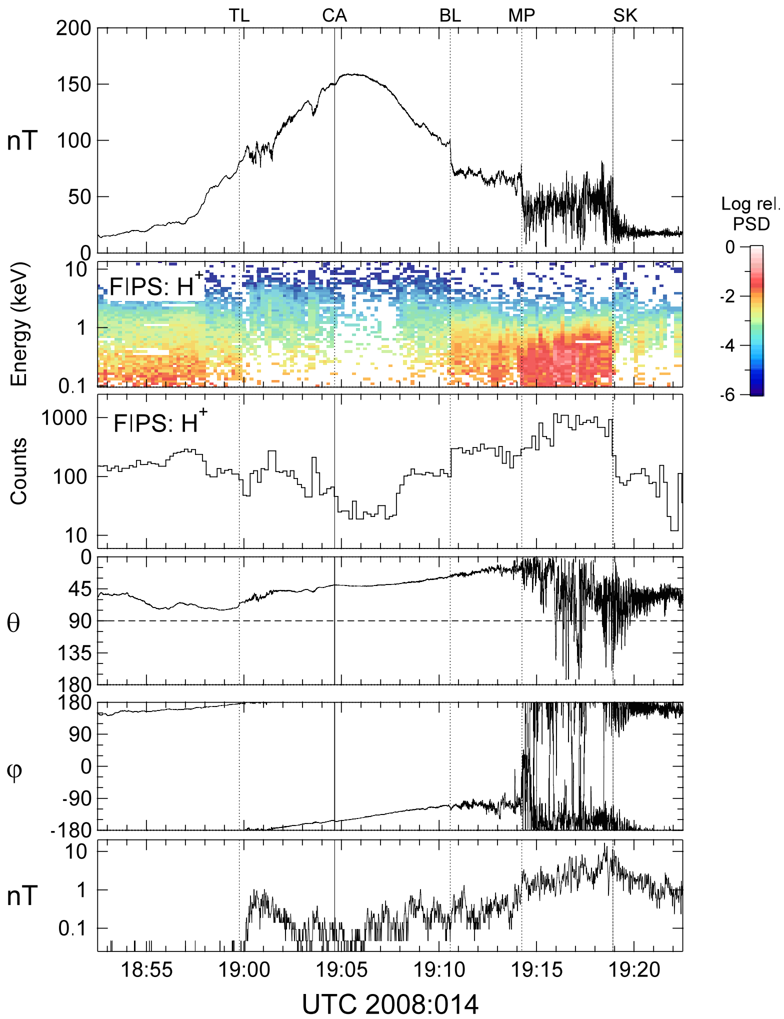

Figure 1.12: MESSENGER first flyby (M1) in MSO coordinates. From top to bottom panels: magnetic field intensity, proton particles energy spectra, particle counts, polar angle ($\theta = 0°$ is northward), azimuth angle ($\varphi = 0°$ is sunward and $\varphi = 90°$ is duskward) and the 1-10-Hz band pass fluctuation.

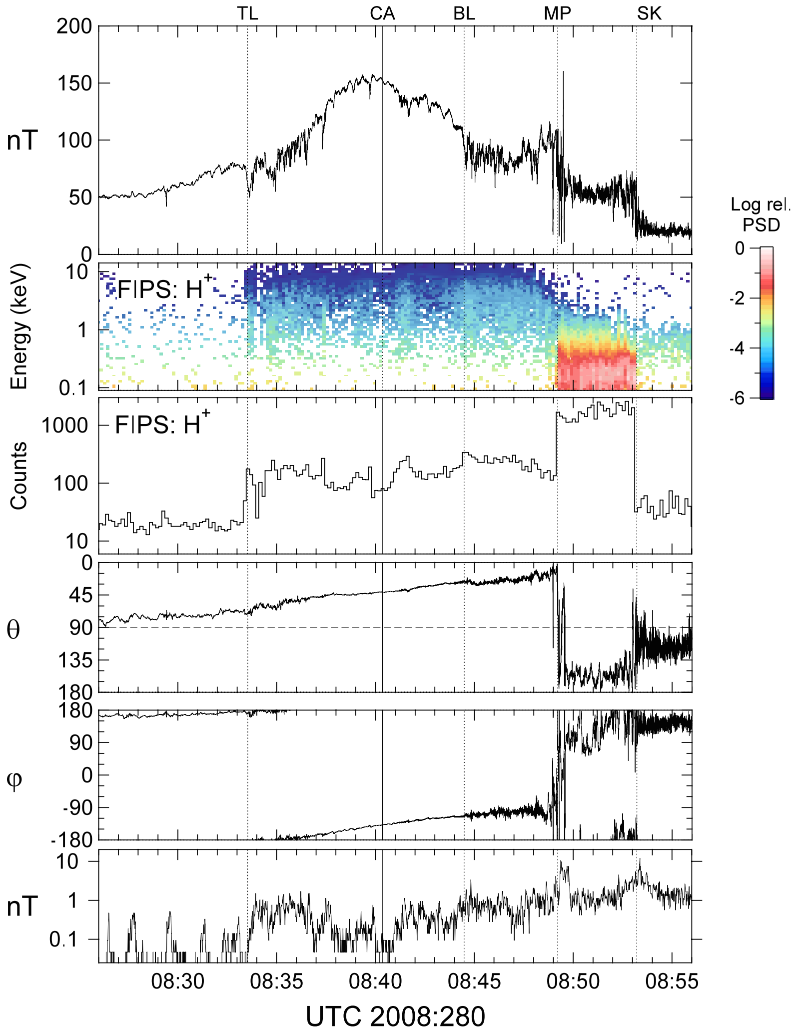

Figure 1.13: MESSENGER second flyby (M2) in MSO coordinates. From top to bottom panels: magnetic field intensity, proton particles energy spectra, particle counts, polar angle ($\theta = 0°$ is northward), azimuth angle ($\varphi = 0°$ is sunward and $\varphi = 90°$ is duskward) and the 1-10-Hz band pass fluctuation.

in intensity and location through some fitting parameters. The physics-based simulations allow for the dynamics of the system to converge for physical self-consistent structures and currents of the magnestosphere and plasma through numerical simulations with fluid and particles equations of motion.

Anderson et al. (2008) concluded that the planetary moment is probably in the range 230 to 290 nT.R_M^3, when using Mariner 10 and first MESSENGER flybys magnetic field measurements. Uno et al. (2009) and Purucker et al. (2009) investigated non dipole magnetic field structures. Uno et al. (2009) used smooth regularized inversions applied to the same data set as Anderson et al. (2008). They corrected for the external fields by a parameterized (empirical) magnetospheric model. For all inversions, a non-dipole component is required in order to fit the data with the 95$\%$ confidence limit, where the quadrupole (g_2^0) is the term that dominates the non-dipolar coefficients. However, terms with SH degrees higher or equal to 4 are determined almost entirely by the regularization constraint and are therefore not reliable. Purucker et al. (2009) studied the remnant magnetic field from crustal origin for the same data as Uno et al. (2009), concluding that both large and small-scale remanence are weak on Mercury. Anderson et al. (2010) used magnetic field measurements of the Mariner 10 and the two first MESSENGER flybys to estimate the internal magnetic field. The time-period limited by TL and BL (Fig. 1.12 and 1.13) contain the M1 and M2 measurements considered for the above referred studies.

Table 1.3 compiles the results for the internal magnetic field that were known from Mariner 10 and MESSENGER flybys. Models are denoted "Dipole" if only including an internal dipole and "Quadrupole" if also including a quadrupole. Concerning the external field correction, models "1 Dipole" and "4 Quadrupole" do not include any (they are labeled with "None"); models "2 Dipole" and "5 Quadrupole" use the TS04-correction developed for the Earth's magnetosphere by Tsyganenko and Sitnov (2005) and adapted for Mercury; models "3 Dipole" and "6 Quadrupole" use spherical harmonic decomposition of external contributions (SHA), and are from Uno et al. (2009). Model "7 Reg." from Uno et al. (2009) is a regularized solution allowing for higher degree terms as: $\mathrm{g}_3^0 = -2$,

Table 1.3: Inversion results for the Hermean magnetic field, using M10-I M10-III, M1 and M2 flybys. Table from Anderson et al. (2010). All coefficients are given in nanoTesla. See text for more details on the models.

Internal model	External model	g_1^0	g_1^1	h_1^1	g_2^0	g_2^1	g_2^2	h_2^1	h_2^2	Residual (nT)
1 Dipole	None	-216	-6	14						42
2 Dipole	TS04	-240	-1	5						29
3 Dipole	SHA	-249	-12	16						30
4 Quadrupole	None	-173	-7	15	-108	-9	-1	16	-17	19
5 Quadrupole	TS04	-213	-4	7	-66	9	4	5	-4	14
6 Quadrupole	SHA	-182	-15	9	-108	10	2	6	-15	15
7 Reg.	TS04	-222	12	2	-24	9	9	-6	8	24
External terms		G_1^0	G_1^1	H_1^1	G_2^0	G_2^1	G_2^2	H_2^1	H_2^2	
3 Dipole	SHA	47	26	8	10	-15	-3	-2	-8	
6 Quadrupole	SHA	7	-4	-15	-9	-9	-3	2	0.4	

$g_4^0 = -4$, $g_5^0 = -5$, $g_6^0 = 0$, $g_7^0 = 1$, $g_8^0 = 0$. "Dipole" models have higher misfit values, and even higher when any external correction is applied. For "Quadrupole" models, misfit values reduce significantly, in some cases by half. The regularized solution of Uno et al. (2009) does not show a better misfit value. It is interesting to note that model "6 Quadrupole" with a SHA external field correction shows a zonal quadrupole term g_2^0 of about 60% the dipole term. This is the same ratio as for the "4 Quadrupole" model which has no external field correction. The model that shows the lower misfit is "5 Quadrupole" where a TS04-correction is applied for the external field. In this case, the quadrupole term is around 30% of the dipole term.

For "Quadrupole" models 5 and 6, each with a different external field correction and nevertheless fitting the data in a very similar way, it is evident that it is not possible to obtain the Hermean internal model without ambiguity. This is particularly true for the quadrupole/dipole ratio, which is very different in the two cases. Improvement on external field modeling is required in order to access the internal magnetic field. Another question concerns the covariance between the different SH terms, due to the partial distribution of the data around the planet. In fact, the huge difference between the g_2^0/g_1^0 ratio between the "Quadrupole" models 5 and 6 may be due to the strong covariance between the dipole and quadrupole terms. In order to assess to the internal magnetic field of Mercury without ambiguity two issues should be solved: how to distinguish contributions from external or internal sources; and how different internal SH terms covary due to a poorly data coverage (an issue that will persist after MESSENGER insertion).

Chapter 2

Mercury's enigmatic weak internal field

During its first and third flybys Mariner 10 spacecraft discovered a global but weak magnetic field (Ness et al., 1974, 1975), as highlighted in Chapter 1. Since then it is known that Mercury possesses a magnetic field of internal origin but with too low intensity to be explained by an Earth-like dynamo. In order to explain this weak magnetic field many other possible mechanisms emerged such as: a thermoelectric dynamo (Stevenson, 1987), a remanent field (Aharonson et al., 2004), a thick and thin-shell dynamos (Heimpel et al., 2005; Stanley et al., 2005), a partly stably-stratified core dynamo (Christensen, 2006; Christensen and Wicht, 2008), a feedback dynamo (Glassmeier et al., 2007; Heyner et al., 2011), or even an iron snow dynamo (Vilim et al., 2010). In this Chapter I review these interesting proposed processes as possibly generating the weak internal magnetic field of Mercury measured by Mariner 10 and MESSENGER spacecraft.

2.1 Estimating the Hermean magnetic field strength

Planetary dynamos are in general thought to operate in a strong-field regime, where the Lorentz force balances the Coriolis and Pressure forces. The Elsasser number Λ measures the ratio of the Lorentz and Coriolis forces and is given by,

$$\Lambda = \frac{B^2}{\mu \lambda \rho_0 \Omega} \tag{2.1}$$

where B is the magnetic field, μ is the magnetic permeability of free space, λ is the magnetic diffusivity of the liquid core (related to the magnetic conductivity σ through $\lambda = 1/\mu\sigma$), ρ_o is the mean outer-core density and Ω is the mean rotation rate of the planet.

For the Earth, the Elsasser number is estimated to be of the order of unity, corresponding to a magnetostrophic state where the Lorentz and Coriolis forces are the leading terms (i.e. Christensen, 2011). For Mercury, extrapolating the observed field strength to the planet's CMB gives a value of $\Lambda \approx 10^{-5}$, which is very low compared to the value for Earth. Numerical dynamos find a range of $\Lambda \approx 10^{-2}$ - 10^2, none as small as Mercury's (Christensen and Aubert, 2006). However, the magnetostrophic balance may be reached through: a stronger small-scale field in the core meaning that the dipolar extrapolation would not be appropriate for Mercury; or a strong toroidal field that is not seen outside the core.

2.2 Dynamo models

The existence of a dynamo requires at least a partially liquid core. Margot et al. (2007) suggested the existence of a liquid layer in Mercury through observations of the longitudinal librations. This liquid layer may be explained by the presence of light elements such as sulfur that reduce the freezing point of iron. Neither the size of the core of Mercury, nor its sulfur content is well constrained.

2.2.1 Thin shell

Stanley et al. (2005) studied thin shell dynamos, with different inner core sizes from 70% to 90% the total core size of the planet. The Rayleigh number R_a (i.e., the ratio between the driving buoyancy forces and retarding effects that oppose convection) varies as well. One of the main interesting features of these models, is the ratio between the dipole field strength at Mercury's core-mantle boundary and the toroidal field strength in Mercury's core $B_{Dip}/B_T \sim 10^{-1} - 10^{-2}$. This range contains the corresponding Earth's ratio value of 10^{-1}. Note that using magnetostrophic balance arguments the ratio of these fields is $B_{Dip}/B_T \sim 10^{-2} - 10^{-4}$, what is much smaller comparing to the Earth's. Figure 2.1 shows a sketch of the convective flow behavior for different shell thicknesses. For Earth-like core thicknesses (Fig. 2.1a) the convection pattern is dominated by columnar rolls (red cylinders) distributed around the tangent cylinder (green line). For this type of convection the poloidal dipolar field generation is efficient in producing the B_{Dip}/B_T ratios similar to that of the Earth. When decreasing the dynamo shell thickness the columns become thinner and are confined to regions where the boundary slope is pronounced. For low Rayleigh numbers (Fig. 2.1b), the convection does not occur inside the tangent cylinder and the rolls are not efficient to convert the toroidal field to poloidal dipole field. In this first case, the B_{Dip}/B_T ratio is small. For higher Rayleigh numbers (Fig. 2.1c), the convection may occur also inside the tangent cylinder, and therefore the system is more efficient in generating the poloidal dipolar field. In this second case, B_{Dip}/B_T ratios may be large. For shell thicknesses small enough the convection both inside and outside the tangent cylinder will occur for similar critical Rayleigh numbers. Here the B_{Dip}/B_T ratio is again large.

Stanley et al. (2005) demonstrated that a dynamo operating in a shell thinner from the Earth's can explain the weak observed Hermean magnetic field. The magnetostrophic balance is established through a strong toroidal field in the core, allowing the dipole poloidal field magnitude to be much weaker than the toroidal field.

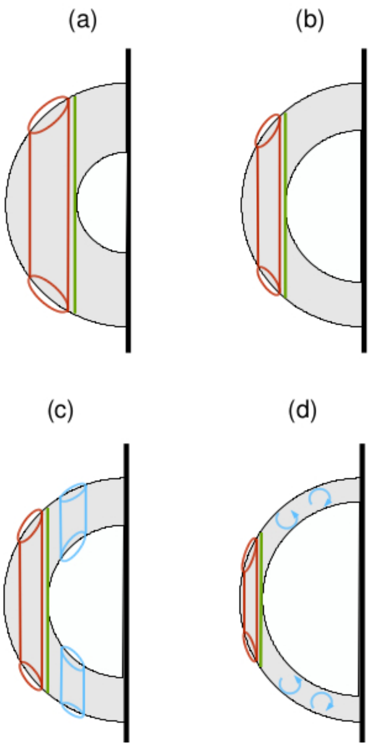

Figure 2.1: Thin shell dynamo model from Stanley et al. (2005): sketch of theoretical convective flow patterns. Meridional slices for models with different shell thicknesses. Black vertical line represents the rotation axis; vertical green line represents the tangent cylinder; fluid outer core is the grey region, and the inner core is in white. Figure from Stanley et al. (2005).

Takahashi and Matsushima (2006) consider in their dynamo model an inner core that occupies 70% of the core, and different Rayleigh numbers. In contrast to Stanley et al. (2005) a non dipolar magnetic field solution is also explored. A dipole dominated dynamo is found for low Rayleigh numbers. For higher Rayleigh numbers the dipole is no longer dominating (Kutzner and Christensen, 2002). Figure 2.2 shows snapshots of the radial magnetic field component from dynamos with low and high Rayleigh number cases, corresponding to $3.5 \times \mathrm{Ra}_c$ and $5.83 \times \mathrm{Ra}_c$, respectively (where Ra_c is the critical Rayleigh number for the onset of convection). For low Rayleigh numbers, magnetic flux patches are distributed at the same mid-latitudes (in north and south hemispheres) along all longitudes at the CMB surface (Fig. 2.2a). These signatures at fixed latitudes correspond to the tangent cylinder limit (Aurnou et al., 2003). At Mercury's surface the small scales have decreased in relative importance because these contributions decay more rapidly with distance (Fig 2.2b). A much simpler and axisymmetric field is found at Mercury's surface, and the tangent cylinder detection at satellite altitudes becomes more challenging. For higher Rayleigh numbers (non-dipolar case), the number of magnetic flux patches in-

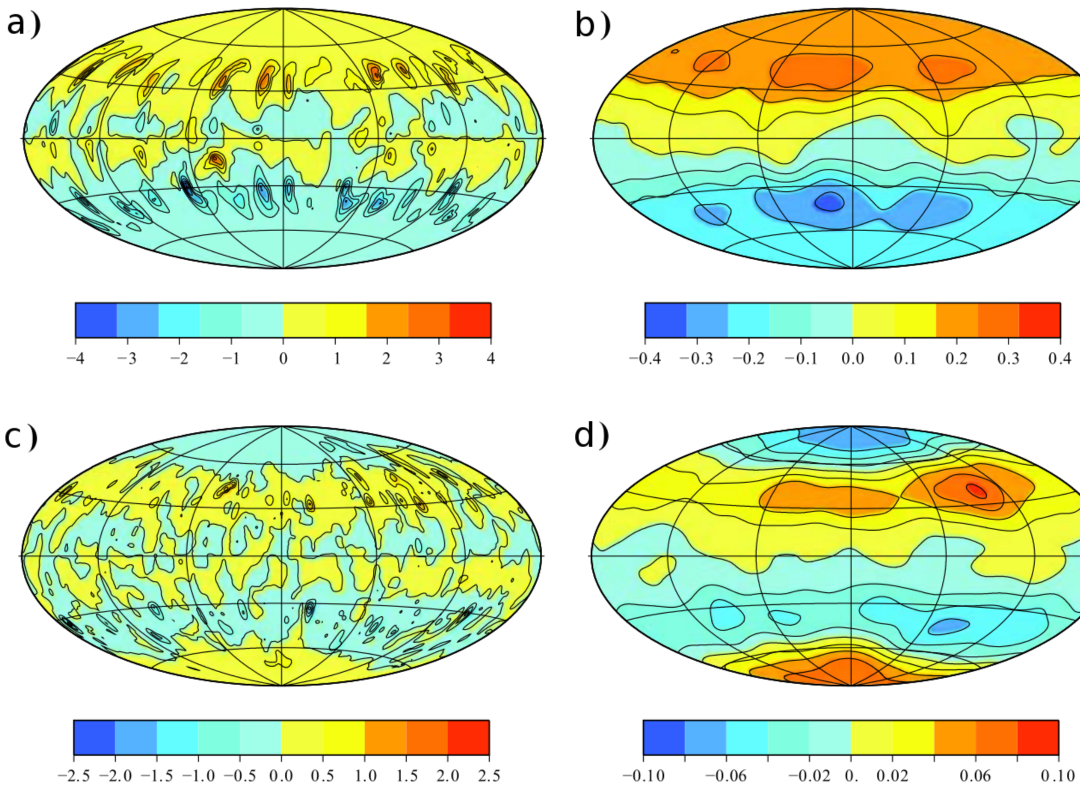

Figure 2.2: Thin shell dynamo model by Takahashi and Matsushima (2006): radial component of the magnetic field at Mercury's core surface (a and c) and at Mercury's surface (b and d), for lower (a and b) and higher (c and d) Rayleigh numbers. Figure from Wicht et al. (2007).

crease but these patches are smaller and distributed irregularly, at the core's surface (Fig. 2.2c). At the planet's surface the small-scale structures are not seen and the (non-dipolar) SH degree 3 axial field is apparent (Fig. 2.2d).

2.2.2 Stable stratification at the top of the core

Christensen (2006) showed that Mercury's magnetic field could be explained through the existence of a stably-stratified layer at the top of the core. In this model, the stable layer is the result of a subadiabatic CMB heat flow. The magnetic field produced in the convecting deeper core is diffused through this conducting outer layer. In this process the magnetic skin effect is relevant. Small-scales and fast time variations are filtered by the upper layer due to the skin effect. In addition, zonal flows that penetrate the stable layer do not produce a significant dynamo, but increase the skin effect for non-axisymmetric field.

Figure 2.3 shows a radial magnetic field snapshot for a model of Mercury magnetic field, with an inner core occupying 50% of the core’s size, at mid-shell (Fig. 2.3a) and at planet’s surface (Fig. 2.3b). Inside the core (Fig. 2.3a), strong small scales are present. At the planet’s surface a much smoother (larger-scale) field is observed. Here the field is dominated by an axial dipole, with also some significant contribution of the axial quadrupole. The power spectra (Fig. 2.3 right) confirm that the dipole is strongly dominant at Mercury’s surface, while inside the fluid shell SH intermediate-scales are the strongest. The dipole dominance at the surface despite its low importance at the core is a consequence of the skin effect.

The stable layer does not only filter the higher SH degree contributions, but also filter possible variations in time. Figure 2.4 shows that the low-frequency axial dipole temporal variation at the core is correlated with the axial dipole at the planet’s surface. The axial quadrupole has a smaller contribution at the surface. For the equatorial dipole the temporal variation at the surface has a very weak amplitude, and therefore can not be distinguished from noise. In conclusion, slow (long time) variations of the axial dipole having a 10,000 yrs time scale penetrate the stable layer, while the rapid fluctuations are filtered. This suggests that if a stable upper layer exists inside Mercury’s core, centuries of observations are needed in order to observe significant variations of the Hermean magnetic field.

2.2.3 Iron snow

Iron-sulfur alloys under high pressures allow the formation of iron precipitate. In the core, the iron precipitate sinks while the more sulfur-rich liquid rises. The movement of the iron ("snow") may act as a source of compositional convection to power the dynamo (Vilim et al., 2010).

Depending on the concentration of sulfur in the core, three different scenarios are possible. For sulfur mass concentrations between 7 wt% and 8 wt%, the iron precipitate forms near the CMB sinking toward the inner core. This condition is known as the "shal-

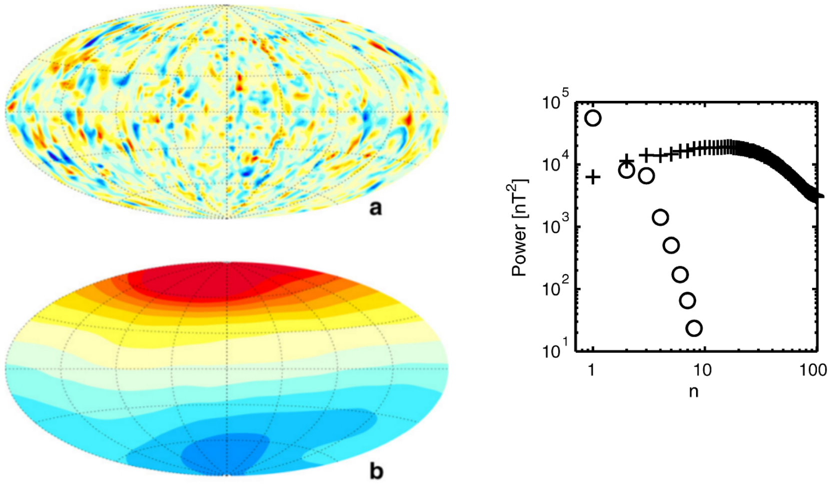

Figure 2.3: Dynamo model with a stably-stratified upper layer. Left: Radial magnetic field snapshot at: a) 0.44D (Where D is the shell thickness) and b) the planet's surface. Contour step is 60,000 nT for a) and 100 nT for b). Right: Time averaged power spectra of the magnetic field at the planet's surface (circles) and of the volume-averaged field inside the fluid shell (crosses) as a function of SH degree n. Note that the core field (crosses) is scaled down by a factor 10^{-4}. Figures from Christensen and Wicht (2008).

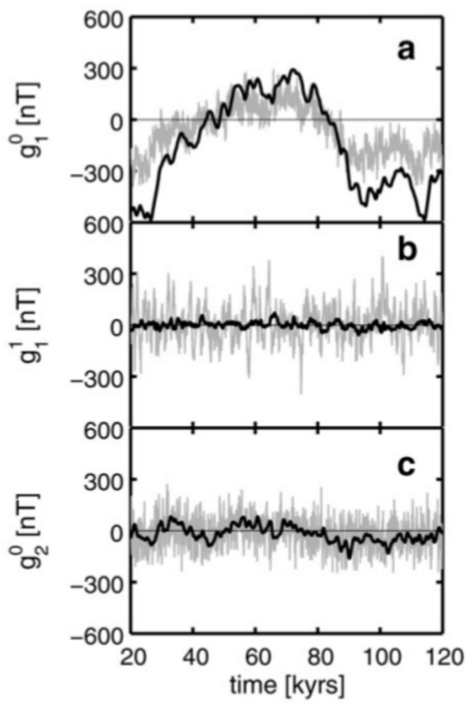

Figure 2.4: Dynamo model with a stably-stratified upper layer. Time series for surface Gauss coefficients a) axial dipole, b) equatorial dipole and c) axial quadrupole. Gray lines describe the poloidal magnetic field inside the fluid shell (scaled down by 0.1). Figure from Christensen and Wicht (2008).

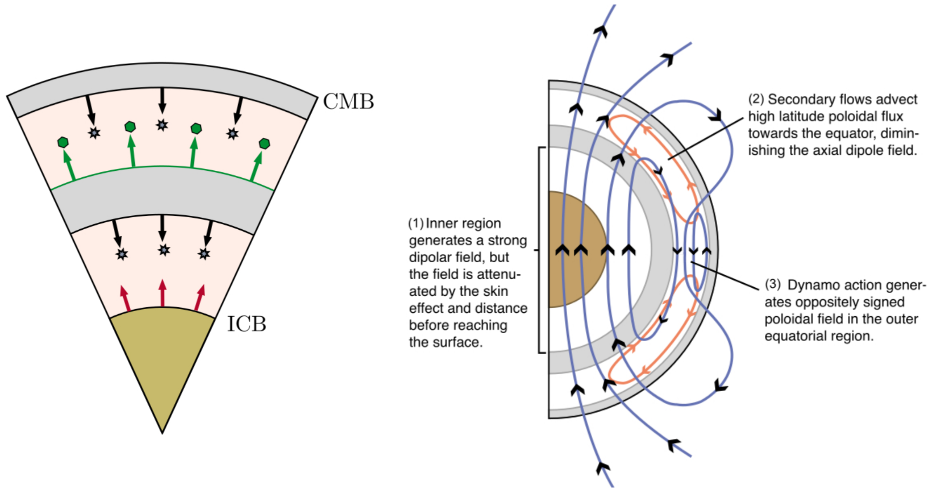

Figure 2.5: Left: Scheme of a core in a double snow state. The regions in gray indicate the snow layers. Black arrows indicate compositional convection while red arrows thermally driven convection. Iron driven effects denoted by stars, and sulfur driven effects by green hexagons. Right: Scheme of the poloidal magnetic field generation in a double snow dynamo model. Figures from Vilim et al. (2010).

low snow state". For concentrations between 8 wt% and 10 wt% two precipitation layers exist, one at the CMB and another at mid-shell. This configuration is called the "double snow state" (Fig. 2.5 Left). Finally, for mass concentrations of more than 10 wt%, the shallow layer disappears leaving only the deeper snow zone, leading to the "deep snow state".

The shallow snow state models produce a dynamo with Earth-like dipole intensities (Stanley et al., 2008). Vilim et al. (2010) studied the double and deeper snow state cases. These two cases successfully produced a weak dipolar field. Moreover, the mid-shell snow layer works as an insulator and the magnetic field originated by convection below that layer is highly filtered by a skin effect. This effect is represented in the schematic diagram (Fig. 2.5 Right). Inside the deeper region the convection produces a strong poloidal field, but only a weak part of it is observed outside the core. In addition, core flow in the outer convective region contributes to the weakening of the axial dipole by advecting high latitude poloidal field to the equator.

Figure 2.6 shows the radial magnetic field at the CMB and planet's surface for a double snow state dynamo model. The tangent cylinder effect caused by the deep snow layer is

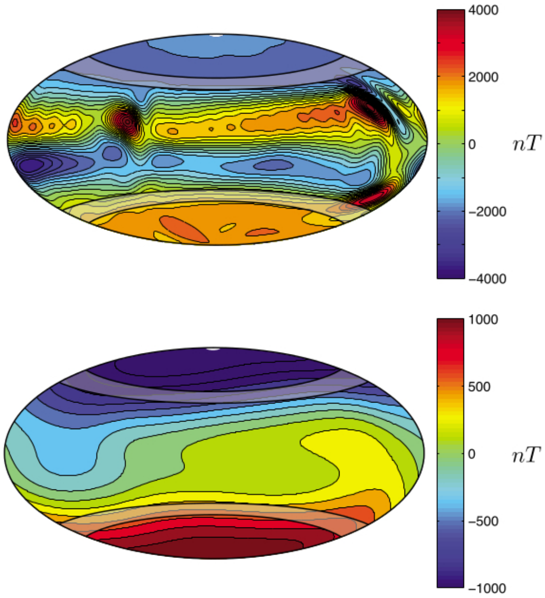

Figure 2.6: Double snow state dynamo model. Radial magnetic field at the CMB (top) and the planet's surface (bottom) for the same snapshot. The tangent cylinder effect caused by the deeper snow layer is shaded grey. Figure from Vilim et al. (2010).

shown in grey bands. As expected the field at the CMB is stronger than at the planet's surface and presents smaller scale features (Fig. 2.6 top). However, these features are concentrated at mid and low latitudes, between the two grey bands. As seen in the scheme of Figure 2.5 Right, the contribution of the outer convective core is important in this model. These small scale features diminish with distance, and at the planet's surface they are no longer apparent. In addition, at the CMB a dominant axial octupole signature is observed, while at the planet's surface axial dipole dominates.

2.2.4 External field negative feedback

Because of the weak internal magnetic field of Mercury and the proximity of the planet to the Sun, external field sources are much more important than in the Earth. Chapman-Ferraro (CF) currents at the magnetopause induced by the interaction between the Hermean magnetic field and the solar wind produce a strong external field of about 47 nT at the CMB depth (Glassmeier et al., 2007). As the planet is embedded in this ambient field it produces a secondary dynamo field that influences the core dynamo. As the CF currents

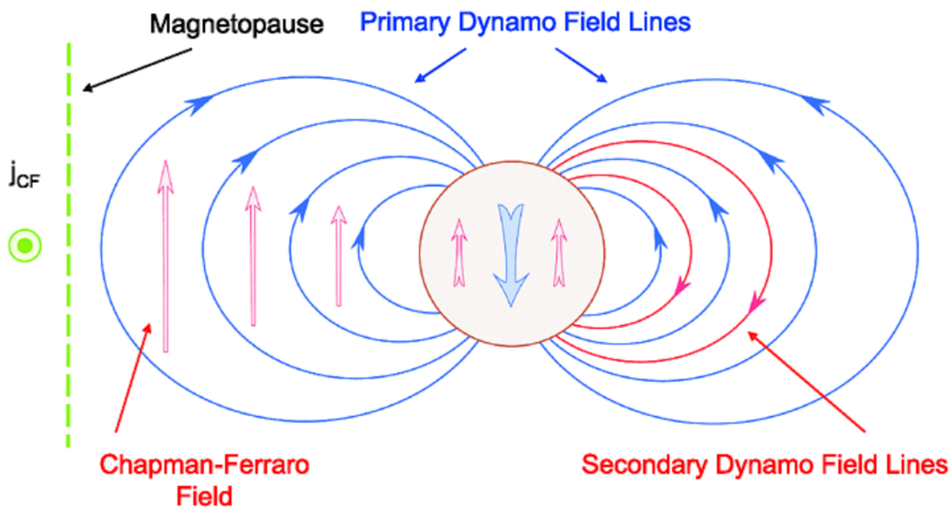

Figure 2.7: Scheme illustrating the feedback dynamo state for Mercury. Figure from Glassmeier et al. (2007).

are affected by this secondary dynamo magnetic field, a feedback state is reached (Fig. 2.7). The measured field becomes weaker because the external field direction opposes that of the internal field.

From the kinematic dynamo model of Glassmeier et al. (2007) a field strength of a few hundred nT is inferred. If no external currents are applied a field strength as that of the Earth is obtained (Heyner et al., 2011).

2.3 Alternative mechanisms

The magnetic field of Mercury may be explained by other processes apart from an MHD dynamo mechanism as described above. Even if MHD dynamo models remain the most plausible scenario, it is possible that other physical processes could also contribute for the actual magnetic field measurements from Mariner 10 and MESSENGER.

2.3.1 Thermoelectric dynamo

Stevenson (1987) proposed the thermoelectric dynamo theory to explain the weak magnetic field of Mercury. For this model he considered: a solid inner core, a relatively thin

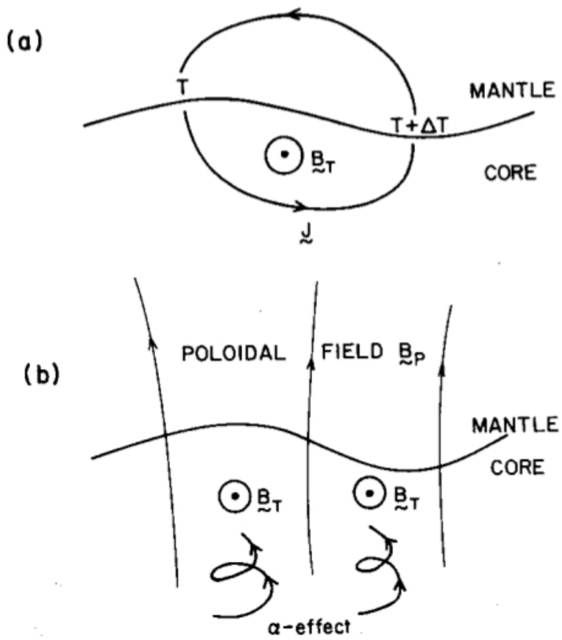

Figure 2.8: The thermoeletric dynamo mechanism: a) The topographic amplitude generates temperature variations and yields a current **J** and the associated toroidal field $\mathbf{B}_T$; b) The α-effect acts on $\mathbf{B}_T$ to induce a poloidal external field $\mathbf{B}_P$. Figure from Stevenson (1987).

convecting outer Fe-S core, and a convecting silicate mantle. The mantle convection distorts the CMB creating a topography of about 1 km amplitude and very long wavelength. This topography yields temperature variations along the CMB, generating a thermoelectric electromotive force between the liquid iron of the core and the solid silicate of the mantle. As Figure 2.8a illustrates, a poloidal current **J** is induced, and this current generates a toroidal field, $\mathbf{B}_T$. Finally, a poloidal field $\mathbf{B}_P$ is produced through the α-effect acting on $\mathbf{B}_T$ (Fig. 2.8b) which can be observed at the planet's surface.

This model predicts a dipole field of 300 nT when considering a mantle conductivity of $\sigma_m = 10^3\ \Omega^{-1}\ m^{-1}$. However this σ_m value is quite strong for Mercury.

2.3.2 Crustal remanence

Aharonson et al. (2004) considered the possibility of a remanent field of crustal origin. If the crust is magnetized, then signatures of remanent field are measurable. For a no homogeneous planetary crust, the Runcorn's theorem (which states a magnetic field from a uniform magnetized shell cannot be observed) it not applied. Different geological processes such as impact cratering, tectonics and magmatism produce the required crust irregularities. In addition, the shell thickness may also vary due to the laterally varying temperature field. To explain such a remanent field, a strong non-reversing dynamo should have existed in the early history of Mercury, during a long period of time corresponding to the crustal cooling duration. This crustal remanence model predicts that the magnetic field of Mercury is described by an axial dipole and octupole, and non-axial octupole SH terms.

2.4 Conclusion

The answer to the question "what is the weak Hermean magnetic field origin?" should be found on measurements with higher precision such as measurements from the present mission MESSENGER as well as measurements from the future mission Bepi-Colombo.

Looking for small-scales and a temporal variation of the magnetic field of Mercury, should help to constrain which of the presented models is the most likely. A magnetic field temporal variation, for instance, shows that a remanent source can not be the only field source. A dynamo model with a stagnant layer (Christensen, 2006) may be distinguished from other models that do not incorporate it (Stanley et al., 2005; Takahashi and Matsushima, 2006) based on its spatio-temporal variability: if the field is predominantly large scale and if the magnetic field of MESSENGER shows no variation compared to Mariner 10 measurements, then the dynamo in a partly stable core is the preferred model. If an effect of tangent cylinder is detected, namely different observed magnetic field structure at a certain latitude, then this may constrain the thickness of the outer core and may support a thin (or thick) shell dynamo.

Chapter 3

A new tool to model the magnetic field of Mercury

After a brief introduction about the context at the beginning of my PhD, I present the new technique to model the magnetic field of Mercury that was developed, validated and finally applied successfully to the first measurements from the MESSENGER mission.

3.1 Context

Mercury is the only other terrestrial planet possessing a global internal magnetic field, thought to be of convective dynamo origin. However, the magnetic field intensity is very weak to be explained by an Earth-like convective dynamo. In order to explain the magnetic field of Mercury different dynamo and physical models were proposed (see Chapter 2). Higher resolution observations allowing to retrieve small-scale features or the behavior of the temporal variation, should help to distinguish one model from the other.

To understand which process may explain the characteristics of the internal magnetic field of Mercury, is one of the main scientific questions that the actual MESSENGER and future Bepi-Colombo missions want to clarify. Models for the internal magnetic field and its temporal variation with good spatial and temporal resolution are a requirement to understand this exotic planetary magnetic field and consequently its internal structure, dynamics and evolution. The goal of my work is to provide an internal field model of Mercury as accurate and detailed as possible.

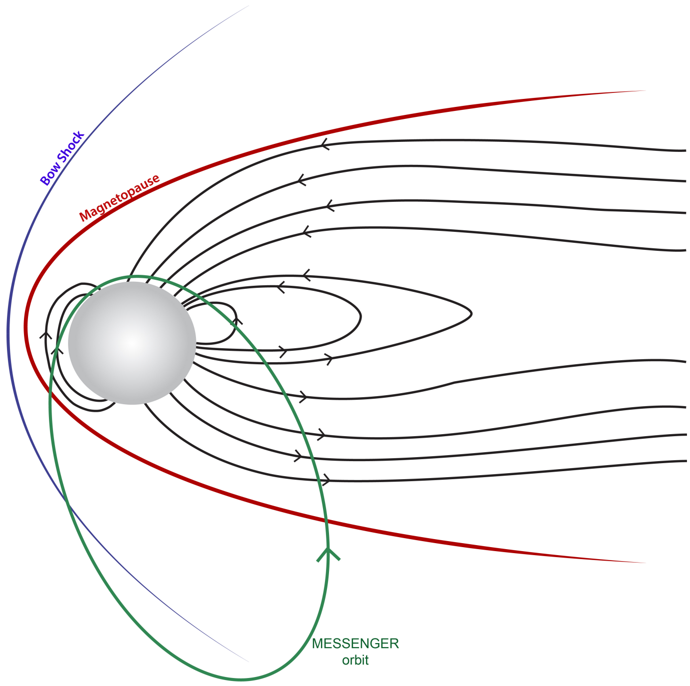

Figure 3.1: Scheme (not in scale) of MESSENGER's spacecraft orbit (green) around Mercury (grey) with an hypothetically scaled Earth-like magnetosphere. Magnetopause and magnetosphere bounds are in blue and red, respectively.

3.1.1 Problem statement

To study the magnetic field of a planet other than the Earth is a real challenge, because the measurements are from a satellite that, in principle, samples the field only through a short period of time and only along its orbit. This usually implies a bad spatial and temporal coverage. At the moment of this thesis writing, only two spacecraft have encountered Mercury: Mariner 10 and MESSENGER. Mariner 10 did only two flybys inside the magnetopause of the planet thirty years before the MESSENGER era. MESSENGER is orbiting the planet since March 2011 and has a very eccentric orbit, in order to cross the magnetosphere and advance the knowledge of its physics. Because only measurements inside the magnetosphere have dominant internal contributions, the eccentric orbit is not ideal to constrain the internal planetary magnetic field, since it doesn't allow for a global planetary coverage. Figure 3.1 shows a scheme of this configuration: MESSENGER orbiting around Mercury which possesses an hypothetically Earth-like scaled magnetosphere. The spacecraft flies inside the magnetosphere of the planet only during a portion of its orbit. Stronger internal to external field ratios are found close to the planet (< 1000 km) corresponding to the northern hemisphere.

Standard global methods to compute magnetic field models, such as spherical harmonics, applied to a partial data coverage will not explain the field correctly. Inversions of such measurements with partial distribution yield terms in the corresponding covariance matrix that are correlated. Figure 3.2 shows the correlation between the different Gauss coefficients for inversions of a constant altitude grid data only over the northern hemisphere. For this specific measurements geometry, the axial dipole coefficient g_1^0 is highly correlated with the axial quadrupole coefficient g_2^0, little correlated with g_3^0, and anti-correlated with g_4^0. Furthermore, the axial quadrupole g_2^0 is correlated with the axial octupole g_3^0 coefficient. Non-zonal coefficients present similar behavior as zonal coefficients. In addition, the correlation matrix shows that zonal coefficients are not correlated with non-zonal coefficients.

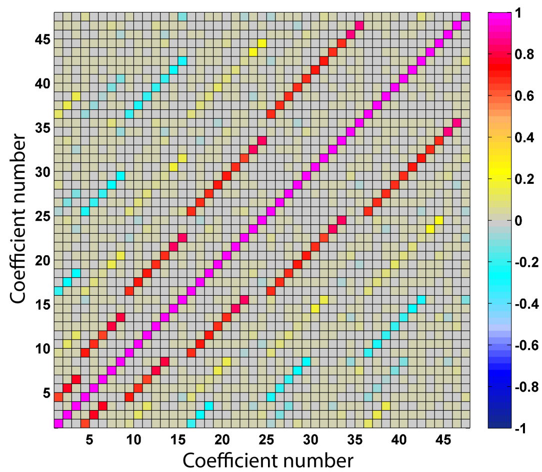

Figure 3.2: Correlation between the Gauss coefficients for an inversion of a constant altitude grid synthetic data over an hemisphere. Order of coefficients to be read: g_1^0, g_1^1, h_1^1, g_2^0, g_2^1, h_2^1, g_2^2, h_2^2 , and so on.

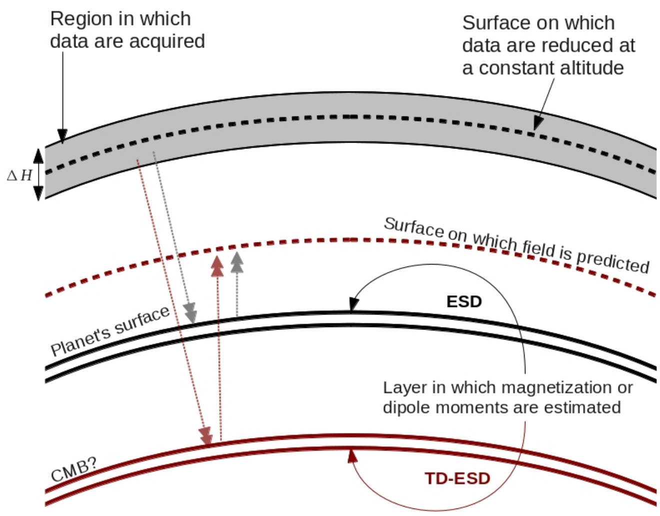

Figure 3.3: Scheme of ESD and TD-ESD methods, where principal differences are highlighted. Scheme adapted from Langel (1987).

3.1.2 Solution concept

Other new methods need to be developed to surpass this difficulty, in order to recover the internal magnetic field of Mercury, from the actual MESSENGER magnetic field measurements. That is the goal of this thesis. Here I present an original way to accomplish this goal based on the regional Equivalent Source Dipoles (ESD) method. In this study the ESD method initially developed to model the crustal geomagnetic field (e.g., Mayhew, 1979) is adapted to model the Hermean core field. The main differences between these two methods are highlighted in Figure 3.3. The dipoles are located at a surface deep inside the planet for the new method instead at shallow depths. Because the most plausible source for the Hermean internal magnetic field is a convective core dynamo, the method would allow for temporal variations. The new method is then called the Temporal Dependent Equivalent Source Dipole (TD-ESD) method. In the next Section this new method is tested and discussed. The first magnetic field maps (for the three spherical components) of the first MESSENGER measurements are also presented in the same Section. A methodical application of the method to all currently available MESSENGER magnetic field measurements is performed and interpreted in Chapter 4.

3.2 Article: A new method to model partially distributed magnetic field measurements, with application to Mercury

This Section describes the method developed in order to model the magnetic field of Mercury, over the northern hemisphere where selected measurements are available. The work presented here correspond to the manuscript submitted to and under review (at the moment of writing) at the Journal of Geophysical Reviews - Planets, by J. S. Oliveira, B. Langlais, M. A. Pais, and H. Amit. A final version of this publication is available online in the same journal, with DOI: 10.1002/2014JE004734. Details about the Equivalent Source Dipoles method and the Inverse Problem can be found in Appendices B and C, respectively.

A modified Equivalent Source Dipole method to model partially distributed magnetic field measurements, with application to Mercury

J. S. Oliveira [1 2], B. Langlais [1], M. A. Pais [2 3], H. Amit [1]

Abstract

Hermean magnetic field measurements acquired over the northern hemisphere by the MESSENGER spacecraft provide crucial information on the magnetic field of the planet. We develop a new method, the Time Dependent Equivalent Source Dipole, to model Mercury's magnetic field and its secular variation over a limited spatial region. Tests with synthetic data distributed on regular grids as well as at spacecraft positions confirm the validity of the new method. Our modeled magnetic field can be upward or downward continued in an altitude range of -300 to 1460 km for regular grids and in a narrower range of 10 to 970 km for spacecraft positions. We apply our method to model the magnetic field during the first four individual sidereal days as measured by MESSENGER and excluding the secular variation terms. We find a dominantly zonal field with small-scale non-axisymmetric features co-rotating with the Sun in the Mercury Body Fixed system and repeating under similar local time, suggestive of external origin. When modeling the field during one complete solar day these small-scale features decrease and the field becomes even more axisymmetric. The lack of any coherent non-axisymmetric feature recovered by our method, which was designed to allow for such small-scale structures, provides strong evidence for the large-scale and close-to-axisymmetry structure of the internal magnetic field of Mercury.

[1]Laboratoire de Planétologie et Géodynamique, LPGNantes, CNRS UMR6112, Université de Nantes, France.

[2]CITEUC, Geophysical and Astronomical Observatory, University of Coimbra, Portugal.

[3]Department of Physics, University of Coimbra, P-3004-516 Coimbra, Portugal.

FIND PUBLISHED VERSION AT JGR PLANETS DOI: 10.1002/2014JE004734

1 Introduction

The discovery of a magnetic field of internal origin on Mercury during the Mariner 10 mission flybys (*Ness et al.*, 1974, 1975) was a surprise. Because of Mercury's small size it was thought that its interior was completely solidified, with no liquid core capable of sustaining a dynamo (*Plagemann*, 1965). But the observed planetary scale of the Hermean magnetic field argues for a deep core dynamo origin. This hypothesis is supported by analyses of the gravity field and of planetary spin parameters from both Earth based radar and MESSENGER radio science measurements, which show that the metallic core of Mercury is at least partially molten (*Margot et al.*, 2007; *Smith et al.*, 2012).

First estimates have shown a weak intensity of Mercury's magnetic field, about 1% of the Earth's (*Ness et al.*, 1974; *Anderson et al.*, 2008) suggesting that the Hermean dynamo works differently. Numerical dynamo studies found that the field magnitude is not determined by a magnetostrophic force balance (i.e., between Coriolis, Lorentz and pressure forces) but instead by the buoyancy flux, with Elsasser numbers varying significantly between 0.06-100 (*Christensen and Aubert*, 2006). Given the estimated field intensity at Mercury's core surface ($\sim 10^{-4}$ mT), the Elsasser number would be on the order of 10^{-4}, well below the lower bound found by *Christensen and Aubert* (2006). Such low value of the Elsasser number is not consistent with any current model of planetary core dynamics, and is therefore very intriguing.

Characterizing the origin and the nature of the Hermean magnetic field are two of the main scientific objectives of the NASA MESSENGER mission (*Solomon et al.*, 2001) that has been in orbit since March 2011. The spacecraft orbits around Mercury on a very eccentric trajectory, with an initial 200-km-altitude periapsis set at 60°N latitude. Because of this very eccentric orbit, only when the satellite flies above the northern hemisphere it does reach an altitude low enough so that the magnetic field of internal origin can be constrained by its magnetometer (MAG) instrument (*Anderson et al.*, 2007).

 DOI: 10.1002/2014JE004734

The first analyses of MESSENGER magnetic field measurements were based on a simple approach as far as the internal part is concerned. *Anderson et al.* (2011, 2012) found that the magnetic equator (where the cylindrical radial field vanishes) is located in the northern hemisphere, with an offset of 0.196 R_M where $R_M = 2440$ km is Mercury's radius. A weak magnetic moment of 190 nT.R_M^3 was obtained via a grid search by *Johnson et al.* (2012), in agreement with previous estimates based on Mariner 10 measurements (*Ness et al.*, 1974, 1975). The location of the magnetic equator at the northern hemisphere motivated modeling the internal field with a simple dipole offset. The estimated dipole offset corresponds to an axial quadrupole to axial dipole ratio of g_2^0/g_1^0 = 0.392 $\pm$ 0.010 (*Anderson et al.*, 2012). In addition, these studies found that the dipole tilt is very small with an upper limit placed at 0.8°. Finally, a recent study attempted to detect the secular variation (SV) of Mercury's field by comparing MESSENGER and Mariner 10 data (*Philpott et al.*, 2014). It was found that the analyzed data are consistent with no SV, although some variations in the lowest zonal SH coefficients are possible.

Previous models of the Hermean magnetic field do not take full advantage of the available measurements as they contain no information on smaller spatial scale features. The standard spherical harmonics (SH) approach is commonly used to represent the global geomagnetic field and is especially appropriate when the data coverage is global (*Cain et al.*, 1989). For other planets or bodies, where measurements are much more sparse and only partially distributed, SH may also be applied when additional constraints or regularizations are imposed (*Connerney et al.*, 1987, 1991; *Holme and Bloxham*, 1996). Alternatively, local methods may be employed, such as the spherical cap harmonic analysis (*Thébault et al.*, 2006) to describe an internal magnetic field measured with a partial planetary coverage. In the case of magnetic field of lithospheric origin, continuous or discrete magnetization models can also be computed (*Langlais et al.*, 2004; *Whaler and Purucker*, 2005).

In this study we choose to adapt an existing method, the Equivalent Source Dipole scheme (ESD) initially developed for the crustal geomagnetic field (e.g., *Mayhew*, 1979), to model the Hermean field. Our method uses MESSENGER's partial data coverage without relying on arbitrary constraints or regularizations. We implement the new method to analyze measurements acquired by MESSENGER spacecraft orbiting Mercury, reaching low altitudes over an area of limited extent. The two main modifications with respect to ESD consist in having deep dipole sources and a linear time dependency for the dipole parameters. We term this method as the Time Dependent Equivalent Source Dipole (TD-ESD) method.

We present in Section 2 the theoretical foundations of the method. In Section 3 we explain the modeling technique and how solutions are chosen. Then in Section 4 the method is tested and validated with synthetic magnetic field data for both ideal and realistic cases. The method is tested against several criteria such as horizontal resolution, depth of the dipoles mesh and noise effect. In addition, we test the range of possible downward/upward continuation. In Section 5 we show the first maps of Mercury's magnetic field components derived using our TD-ESD method. In Section 6 we discuss our results and compare with previous studies. Finally, in Section 7 we summarize our main findings.

2 Theory

The Time Dependent Equivalent Source Dipole method is an extension of the Equivalent Source Dipole method. The ESD method applied to magnetism was introduced by *Emilia* (1973). It initially aimed at reducing to a common altitude magnetic field anomaly measurements of lithospheric origin acquired at various altitudes (*Mayhew*, 1979; *von Frese et al.*, 1981; *Purucker et al.*, 1996; *Dyment and Arkani-Hamed*, 1998). It is commonly used to produce global lithospheric magnetic field maps of the Earth (*Purucker et al.*, 1998), Mars (*Langlais et al.*, 2004) and Moon (*Purucker et al.*, 2012), and may be applied to local data coverage (*Purucker et al.*, 2002; *Langlais and Purucker*, 2007).

In the ESD method, the magnetic field measured at a given location results from individual contributions by dipolar sources located at some depth. The magnetic potential due to a single source is given by

$$V = -\frac{\mu_0}{4\pi}\mathbf{M}\cdot\nabla\frac{1}{l} \tag{1}$$

where $\mathbf{M}$ is the magnetization of the dipole located at spherical coordinates radius, colatitude and longitude (r_d, θ_d, ϕ_d). The magnetic field depends on the magnetic potential through $\mathbf{B} = -\nabla V$. The distance between the dipole and the observation point at (r, θ, ϕ) is

$$l = \sqrt{r_d^2 + r^2 - 2r_d r\left(\cos\theta\cos\theta_d + \sin\theta\sin\theta_d\cos\left(\phi - \phi_d\right)\right)} \tag{2}$$

For the ESD approach the dipole sources are placed at the surface of the planet or a few kilometers below (*Langlais et al.*, 2004), because the lithospheric magnetic field has a shallow origin. Here for the TD-ESD method the dipole sources are placed at a spherical surface deep inside the planet's interior in order to model the magnetic field of core origin. In addition we may let the magnetization vary in time, as the observed core field is also time-dependent. This is done through:

$$\mathbf{M}(t) = \mathbf{M}(t_0) + (t - t_0)\dot{\mathbf{M}} \tag{3}$$

where $\mathbf{M}(t_0)$ is the magnetization at a reference time t_0 and $\dot{\mathbf{M}}$ is its rate of change. We assume that the time-dependence is linear. This approximation may be too simplistic to model the field variations associated with core dynamics. We however note that using a more complex parameterization would not change the concept of the approach, and can be considered in the future if necessary. The TD-ESD method thus simultaneously describes the three observed magnetic field components B_r, B_θ, B_ϕ as being due to an internal distribution of the three magnetization components M_r, M_θ and M_ϕ and the three components of its time variation rate. This new method therefore requires fitting six parameters at each dipole position instead of three as in the original ESD method.

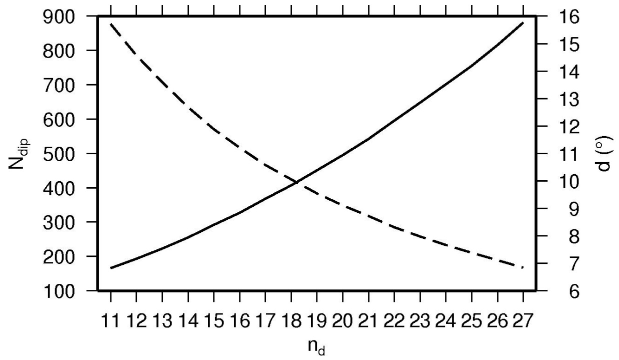

Figure 1: Total number of dipoles N_{dip} (solid line) and the mean distance between adjacent dipoles in degrees d (dashed line) as a function of the dipole mesh parameter n_d.

3 Method

3.1 Spatial resolution

The method searches for magnetization components and their variation rate for each dipole. These dipoles are located on an equisurface and equidistant mesh deep inside the planet at a depth R_d. We use the polar coordinate subdivision method (*Katanforoush and Shahshahani*, 2003) for distributing the dipole sources. The spherical surface is divided into n_d equally spaced latitude bands, where n_d is the dipole mesh parameter. At colatitude θ_j, where $\theta_j = \pi - \frac{\pi j}{(n_d+1)}$ and $j = 1, ..., n_d$, we place N_j equally spaced dipoles, where N_j is the integer of n_j, the latter given by

$$n_j = \left[\frac{1}{2} + \sqrt{3}(n_d+1)\sin\theta_j\right]. \qquad (4)$$

At alternate latitudes, a longitudinal phase shift is imposed to render the mesh more homogeneous. The relation between n_d and the total number of dipoles on the sphere N_{dip} is shown in Figure 1.

Increasing n_d corresponds to increasing N_{dip} and to decreasing the mean spacing d between adjacent dipoles, leading to a better spatial resolution. Figure 2 shows an example of a dipole mesh with $n_d = 15$. In the following we assume that each dipole is assigned to a

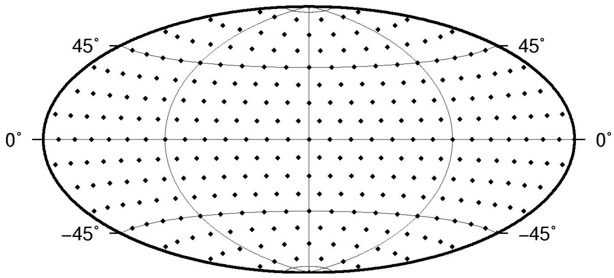

Figure 2: Example of a dipole mesh using the polar coordinate subdivision method for a dipole mesh parameter $n_d = 15$.

horizontal circular surface and that its associated magnetization is confined to a 10 km vertical layer. The choice of thickness affects the magnitude of the magnetization (which is not given any physical interpretation), but not the magnitude of the magnetic field, so this choice is not critical (*Purucker et al.*, 2012).

3.2 Inversion and model evaluation

The inverse problem is written as

$$b = Dx + \nu \tag{5}$$

where b is the column vector containing the magnetic field components, x is the column vector containing the magnetization and rate of change components and D is the matrix containing the partial derivatives relating b to x; ν is the error vector. The magnetic field due to an individual dipole is proportional to $1/l^3$ so observations too far away from a given dipole do not constrain its magnetization. As a result the matrix D is sparse (e.g., *Purucker et al.*, 1996) and includes only elements for which the observation-to-dipole distance is less than a threshold value or when the angle between the observation point and the dipole is less than 90°.

To determine x, we solve the linear inverse problem as successively described by *Purucker et al.* (1996, 2000); *Langlais et al.* (2004); *Langlais and Purucker* (2007), which seeks to minimize the sum of squares of residuals, $\nu^T \nu$. We use the iterative conjugate gradient technique to solve the inverse problem. This leads to a set of possible solutions, i.e., successive magnetization distributions, each one associated with a unique misfit to the observations.

We monitor the evolution of σ_{B_j}, the root mean square (rms) difference between the observed and modeled magnetic fields, with respect to σ_{M_j}, the rms magnetization, as a function of iteration number j. These quantities are written as:

$$\sigma_{\mathbf{B}_j} = \sqrt{\frac{\sum_{i=1}^{N_{obs}} (\mathbf{B}_i^{obs} - \mathbf{B}_{i,j}^{mod})^2}{N_{obs}}} \tag{6}$$

and

$$\sigma_{\mathbf{M}_j} = \sqrt{\frac{\sum_{i=1}^{N_{dip}} \mathbf{M}_{i,j}^2}{N_{dip}}} \tag{7}$$

where $\mathbf{B}^{obs}$ and $\mathbf{B}_j^{mod}$ are the observed and predicted (by $\mathbf{M}_j$) magnetic field vectors, respectively, and N_{obs} is the number of measurements. The full series of σ_{B_j} and σ_{M_j} are denoted σ_B and σ_M.

The vector correlation coefficient is also calculated during the tests according to:

$$r_{B_j} = \frac{\sum(\mathbf{B}_j^{mod} - \overline{\mathbf{B}_j^{mod}}) \cdot (\mathbf{B}^{obs} - \overline{\mathbf{B}^{obs}})}{\sqrt{\sum(\mathbf{B}_j^{mod} - \overline{\mathbf{B}_j^{mod}})^2}\sqrt{\sum(\mathbf{B}^{obs} - \overline{\mathbf{B}^{obs}})^2}} \tag{8}$$

where $\mathbf{B}^{obs}$ and $\mathbf{B}^{mod}$ are the observed and modeled magnetic field vectors and $\overline{\mathbf{B}^{obs}}$ and $\overline{\mathbf{B}^{mod}}$ their spatial averages, respectively. An r_B value close to 1 means that the modeled and observed magnetic field patterns are alike. Given the large amount of observations compared to the number of dipoles (large number of degrees of freedom), a correlation coefficient larger than ∼0.2 is statistically significant with 95% confidence (*Press et al.*, 1989).

We look for the iteration associated with low values in both σ_B and σ_M, for which the magnetization distribution satisfactorily explains the measurements without being unrealistically too energetic. This is illustrated in Figure 3a which shows a trade-off curve between σ_B and σ_M. The misfit to the observed magnetic field decreases while the magnetization

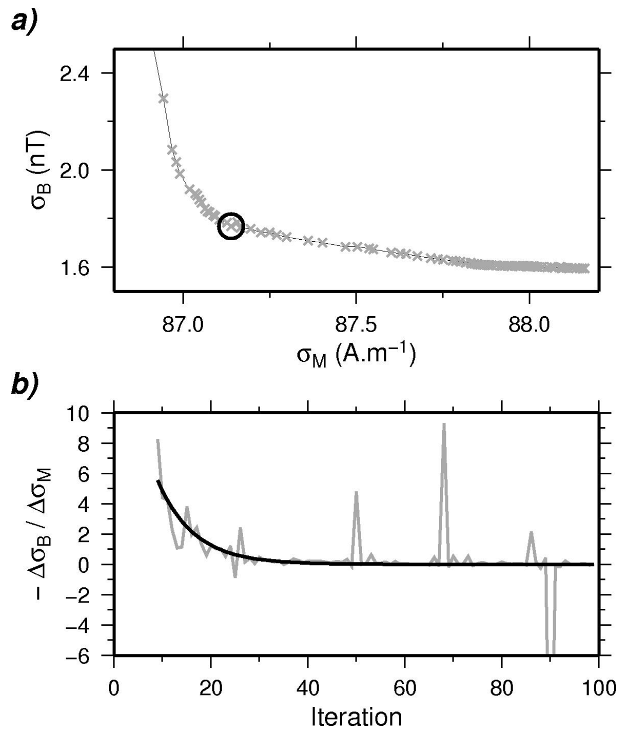

Figure 3: (a) Example of a trade-off curve between σ_B and σ_M as a function of the iteration number using synthetic data on grids. (b) $-\Delta\sigma_B/\Delta\sigma_M$ as a function of the iteration number (grey line), with its exponential fit of the filtered curve (black line). The black circle in (a) shows σ_B and σ_M for the iteration chosen using (b), see text for details. The synthetic data are composed of six regular grids at 300 km, 400 km and 500 km altitude and at two different epochs (with one terrestrial year difference). The dipole mesh is located at 640 km depth with n_d = 19 (see Section 4.2).

increases with increasing iteration number. After iteration 1, σ_B rapidly decreases to a low value with a small increase of σ_M. The following iterations show a slowly decreasing σ_B but more rapidly increasing σ_M. Finally σ_B approaches an asymptotic value while σ_M continues to increase. The solution is commonly chosen in the knee of the trade-off curve (*Gubbins*, 2004). To select the optimal iteration, we look for the iteration number when the slope of the trade-off curve (Fig. 3a) begins to flatten. The $-\Delta\sigma_B/\Delta\sigma_M$ curve can be very noisy but nonetheless shows a global decaying trend as a function of the iteration number (Fig. 3b). We use a pseudo-Gaussian filter which eliminates the spikes, and we fit the filtered curve with an exponential function. In the example shown in Figure 3b, the correlation coefficient between the filtered and fitted curves is 0.99. The solution is chosen when the fitted curve reaches a fixed percentage of its maximum value, which we arbitrarily set to 10%. In Figure 3b this corresponds to $j = 27$, as highlighted by the red circle in Figure 3a. We also tested the result with a threshold value of 1%, leading to an optimal solution at $j = 44$. The magnetization rms increases by 8.4 % while the rms difference between observed and modeled magnetic field only decreases by 0.35%, with correlation coefficients exceeding 0.99 between M_{27} and M_{44} and between B_{27}^{mod} and B_{44}^{mod}. This shows that additional iterations do not significantly improve the fit to the measurements while causing a significant increase of the magnetization, thus supporting our choice of selecting a smaller iteration number with a 10% threshold.

4 Validation

Before applying the TD-ESD method to invert the magnetic field measurements from MESSENGER, we test the method using synthetic measurements based on a scaled-to-Mercury geomagnetic field model. Measurements are mapped either on regular grids at different altitudes or at spacecraft positions. We evaluate the dependence of the misfit on the various parameters of the inversion, including the dipole mesh resolution and depth. We also esti-

 DOI: 10.1002/2014JE004734

mate the altitude range where the resulting magnetic field can be adequately modeled.

4.1 Synthetic data

A synthetic SH magnetic field model is generated by scaling an Earth's magnetic field model to Mercury's geometry and intensity, taking into account its higher core to surface radii ratio and weaker magnetic field intensity. We use the POMME-4.1 internal field model, an updated version of POMME-3.0 (*Maus et al.*, 2006), truncated to degree 10. First the model is downward continued to some depth $R_{\oplus}^{h}$ inside the Earth's mantle, so that

$$\frac{R_{\oplus}^{c}}{R_{\oplus}^{h}} = \frac{R_{M}^{c}}{R_{M}} \tag{9}$$

where $R_{\oplus}^{c}$ is the radius of the Earth's core, and R_{M}^{c} and R_{M} are the core and surface radii of Mercury, respectively. This determines the magnetic field pattern at Mercury's surface. In equation 9 we use a Mercury core radius of 1800 km, within the range of values proposed by *Verhoeven et al.* (2009). More recent studies proposed a core radius of about 2020 km (*Hauck et al.*, 2013; *Rivoldini and Van Hoolst*, 2013). The choice of this value is however not critical as it is only used here as a geometric scale factor. Second the Gauss coefficients are scaled by f with

$$f = \frac{g_{1M}^{0}}{g_{1\oplus}^{0}} \tag{10}$$

where $g_{1\oplus}^{0}$ is the axial dipole Gauss coefficient of the geomagnetic field model and g_{1M}^{0} is the corresponding coefficient of Mercury, taken as the average of models 5 and 6 of *Anderson et al.* (2010) from Mariner 10 and MESSENGER flybys (see their Table 1).

We use the same factor f to scale the geomagnetic SV to Mercury, corresponding to assuming SV correlation times (*Hulot and Le Mouël*, 1994) identical for Earth and Mercury. To establish a criterion for the SV detection time we also consider larger SV by multiplying the scaling factor f by 10 and 20. In the following the three SV models are denoted normal, fast and superfast. The scaling factors used are chosen only for testing the TD-ESD method and do not intend to simulate the actual temporal variation of the internal magnetic field at

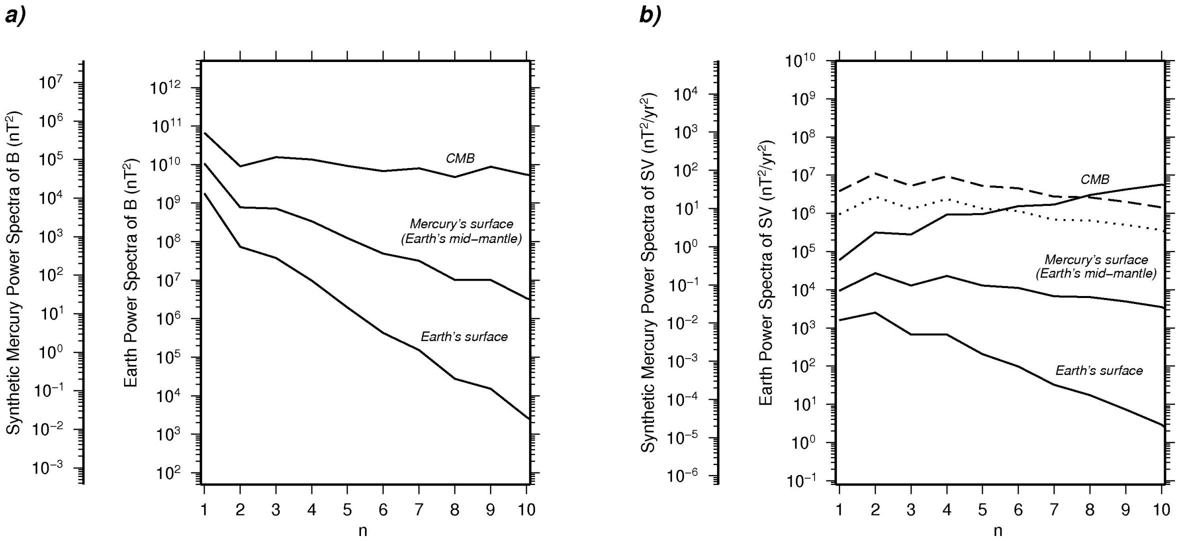

Figure 4: Power spectra of (a) the magnetic field and (b) the secular variation for the Earth (POMME4.1 model) and the synthetic scaled to Mercury model, with inside and outside y-axes, respectively. For both plots the spectra are computed at three surfaces: Earth's surface, Mercury's surface corresponding to Earth's mid-mantle and the CMB. Also shown on (b) the fast and superfast synthetic SV models at Mercury's surface (dotted and dashed lines, respectively).

Mercury. They nonetheless give us some insight about the time interval that should be covered by the data in our TD-ESD inversion method, in order to properly recover the Hermean SV.

The power spectra of the main field and its SV for the Earth and the corresponding synthetic spectra for Mercury are shown in Figure 4. As expected, the main field power spectrum at Earth's mid-mantle corresponding to Mercury's surface is steeper than at Earth's CMB, but flatter than at Earth's surface. The field spectra at Earth's mid-mantle and at Mercury's surface show a dominant dipole. The quadrupole and the octopole have roughly the same energy. The SV spectra at Earth's mid-mantle and at Mercury's surface are rather flat, as opposed to blue at Earth's CMB and red at Earth's surface. We note that degrees 2 and 4 dominate the SV spectra at Earth's mid-mantle (Mercury's surface).

 DOI: 10.1002/2014JE004734

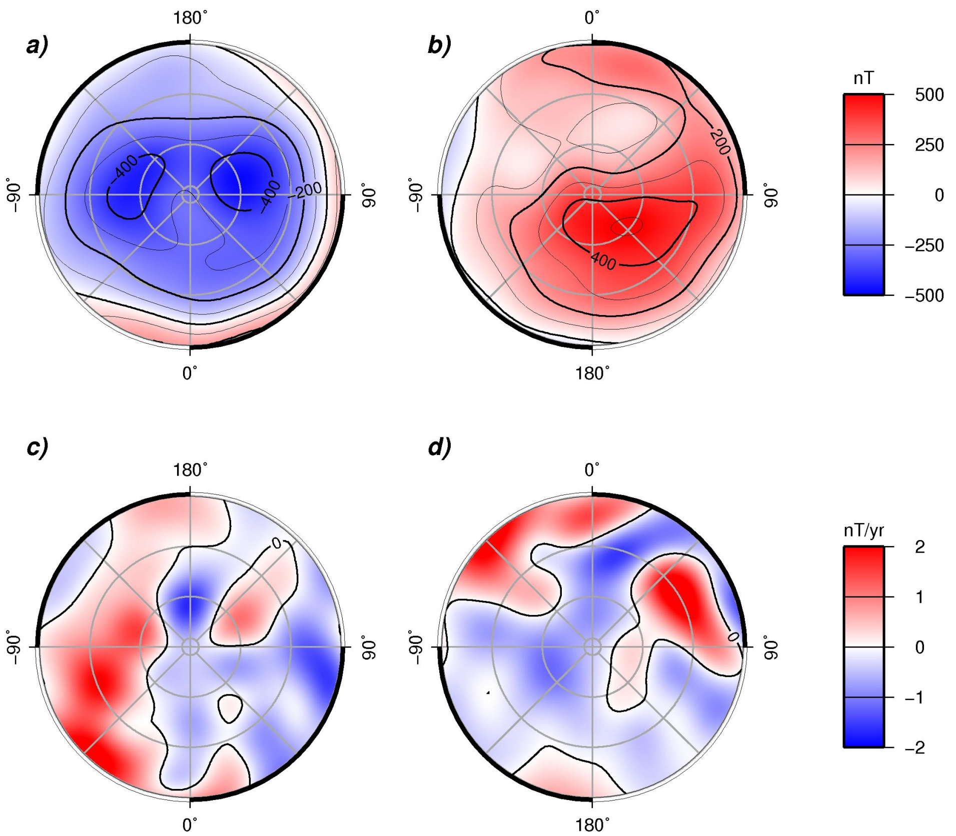

Figure 5: Synthetic magnetic field (a and b) and normal SV (c and d) at Mercury's surface in northern (a and c) and southern (b and d) polar views using a stereographic projection. Grid lines (grey) are drawn every 45° for longitude and every 30° for latitude.

Maps of the synthetic radial magnetic field and its normal SV at Mercury's surface are shown in Figure 5. The synthetic radial magnetic field varies between -488 and 512 nT, while the radial SV (normal case) varies between -1.7 and 2.65 nT/yr. Non-zonal main field contributions that are very strong at Earth's CMB (*Christensen et al.*, 2010) and rather weak at Earth's surface would still be very evident at Mercury's surface (corresponding to Earth's mid-mantle).

4.2 Ideal case: data on regular grids

We first test our TD-ESD method with synthetic data on regular grids. This represents the ideal case where measurements are acquired uniformly and globally. These grids have con-

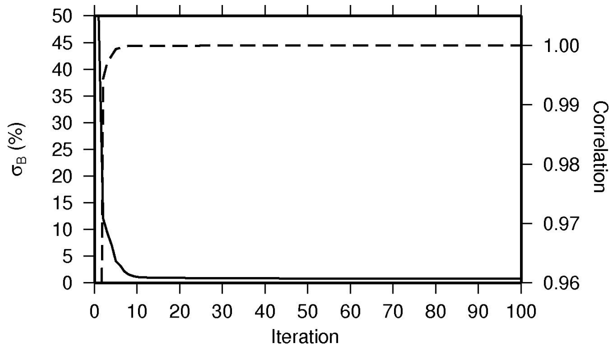

Figure 6: Relative misfit of the magnetic field vector (solid line, left axis) and the vector correlation coefficient (dashed line, right axis) vs. iteration number.

stant latitude and longitude 2° increments. Three different altitudes above Mercury's surface (300 km, 400 km and 500 km) are considered, as well as two epochs (separated by one year), leading to six synthetic grids. Several dipole mesh parameters n_d values are tested, between 8 and 24. Different dipole mesh depths R_d are also considered, between 0 km and 1300 km.

In Figure 6 we show the relative misfit (i.e., σ_B divided by the initial rms field σ_{B_0}) and the vector correlation coefficient as a function of the iteration number for $n_d = 19$ and for R_d = 640 km, corresponding to the case presented in Figure 3. Both the relative misfit and the correlation coefficient reach asymptotic values relatively early. The misfit reaches 2% of the initial field rms at iteration number 13. The correlation coefficient reaches its asymptote faster, and exceeds 0.99 after iteration 2.

We use the scheme described in Section 3.2 to choose the optimal solution at iteration number 27, as shown in Figure 3. For this solution, the relative misfit is 0.87% (1.79 nT) and the correlation coefficient is above 0.99. The synthetic normal SV is also recovered at Mercury's surface but with a degraded quality, with a relative misfit of 75% and correlation coefficient of 0.81. For the fast and superfast cases the situation improves with relative misfit values of 8.1% and 5.8%, respectively, and the corresponding correlation coefficients exceed 0.99.

The sensitivity of the solution to the resolution of the dipole mesh is tested by varying

n_d between 8 and 24 with R_d = 640 km (Fig. 7a). The relative misfit decreases from n_d = 8 to 15, and then there is only slight changes for larger n_d values. Odd n_d values are preferred in order to keep a symmetric dipole distribution with respect to the equator. In the following we use $n_d = 19$, which is a good balance between the computational cost (increasing with n_d) and the misfit to the measurements.

Next we test the impact of the dipole mesh depth choice on our results. Several R_d values are considered, from Mercury's surface down to 1300 km depth with a 50-km increment (Fig. 7b). Three main trends are found. From the surface down to 250 km depth, relative misfit values rapidly decrease from 28% to 0.9%. Between 300- and 850-km depth the misfit values are low and roughly constant, between 0.8% and 1%. Finally, for deeper dipoles the misfit values increase. From this test we conclude that the exact choice of R_d is not critical and that any depth between 300 and 850 km leads to comparably satisfying solutions. We also note that this interval contains the 640-km-depth value that we assumed to scale our synthetic SH model.

We further evaluate the altitude range at which the field can be reliably downward or upward continued (Fig. 7c). The field is computed at different constant altitudes from -400 to 2000 km (10-km increment) on regular grids of 2° resolution from both the initial SH model and from the TD-ESD resulting model, assuming R_d = 640 km and n_d = 19. The lowest misfit between the SH and TD-ESD models is found as expected at 400-km altitude, which is the average altitude of the synthetic data grids. Between -300 and 1460-km altitudes the relative error is lower than 8%, and we consider this to be the altitude range at which the resulting model can be used to reliably map the magnetic field.

Finally we also consider the effect of adding noise to the synthetic measurements (Fig. 7d). We assume a white noise with different amplitudes. Resulting measurements are then inverted with the TD-ESD method, again using R_d = 640 km and n_d = 19. We observe a linear increase of the misfit values with increasing noise amplitude. Without any noise the misfit is 1.78 nT (relative misfit of 0.87%). This may be considered as the lowest bound of

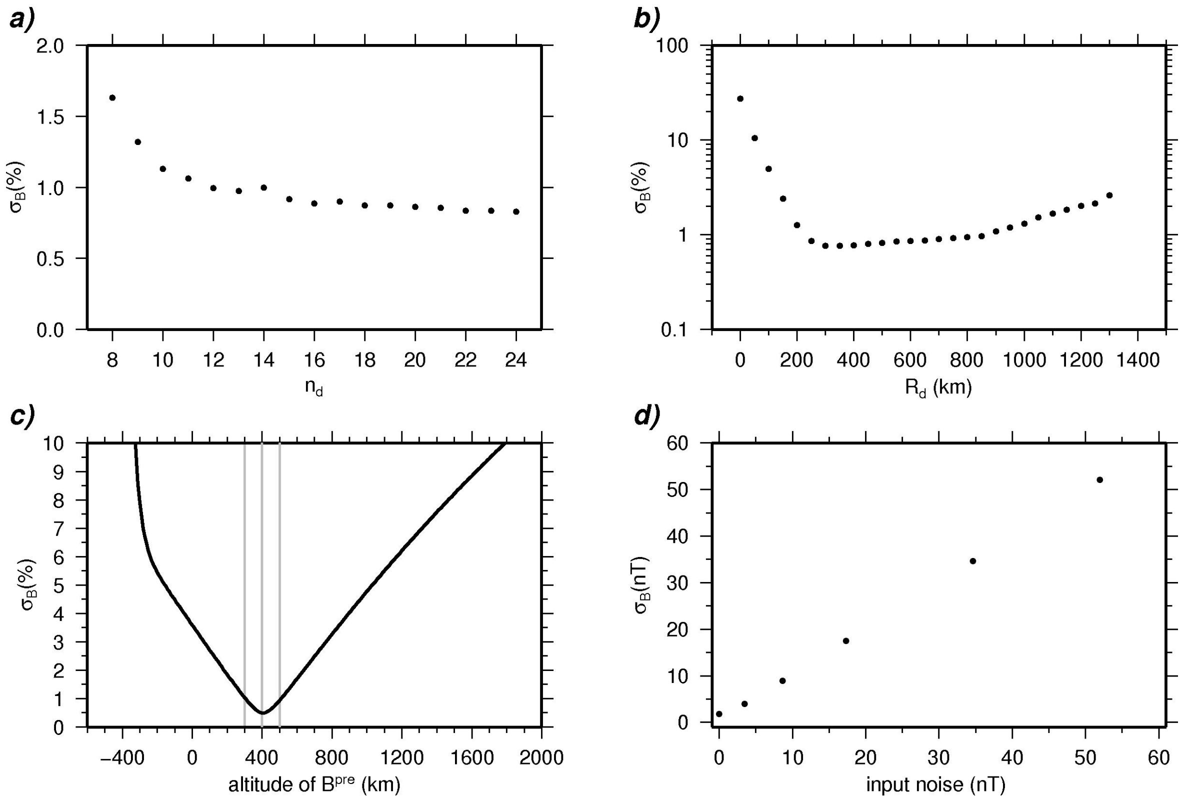

Figure 7: Relative magnetic field misfit as a function of (a) dipole mesh parameter n_d, (b) dipole mesh depth R_d, (c) modeled magnetic field altitude. The grey vertical lines on (c) represent the input grids altitude. On (d) the absolute misfit is shown vs. the input white noise amplitude. For (a-d) the dipole mesh is 640-km deep and the dipole mesh parameter is set to $n_d = 19$ unless specified. The synthetic data are predicted on six regular grids at 300 km, 400 km and 500 km altitudes and at two different epochs with one terrestrial year difference.

our method in the ideal case.

4.3 Realistic case: data along spacecraft orbits

Next we test the TD-ESD method with synthetic measurements at MESSENGER spacecraft positions in order to simulate realistic conditions. During its primary mission MESSENGER was on a very eccentric, near polar orbit, with a 200-km altitude periapsis at 60°N latitude. In the southern hemisphere the apoapsis was above 15000 km. Magnetic field measurements were thus acquired both inside and outside the magnetosphere. Here we are interested in measurements inside the magnetosphere, i.e., where internal source contributions dominate. The orbital positions of the first sidereal day are selected using an external field proxy (defined in next Section) and a 1000 km altitude limit, and span a total time interval of 58.6 days between March 23 and May 20, 2011. The same exact sidereal day spacecraft positions are used twice with a 1-yr time difference. This limits modeling errors related to differences in the position between the two sidereal days and allows focusing on the local temporal variation of the field instead. The SV is taken into account both during and between sidereal days.

In contrast to the ideal case where measurements are homogeneously distributed, measurements along MESSENGER orbits are available only above the northern hemisphere and along orbit paths. Because of this, σ_M and σ_B have to be carefully computed to minimize edge effects. Considering first which source dipoles should be included in the calculation of σ_M, we note that every dipole is sensitive to a certain angular range of measurements above it and there is a latitude limit below which dipoles become less constrained. We looked at the number and the magnitude of elements in matrix D associated with each dipole and found that only dipoles from the north pole down to 30°N latitude are fully constrained, whereas dipoles south of 30°N are decreasingly constrained. In the following σ_M is therefore computed using only dipoles north of 30°N. We also estimate the latitude range at which the magnetic field at constant altitude can be adequately modeled by the TD-ESD method, given

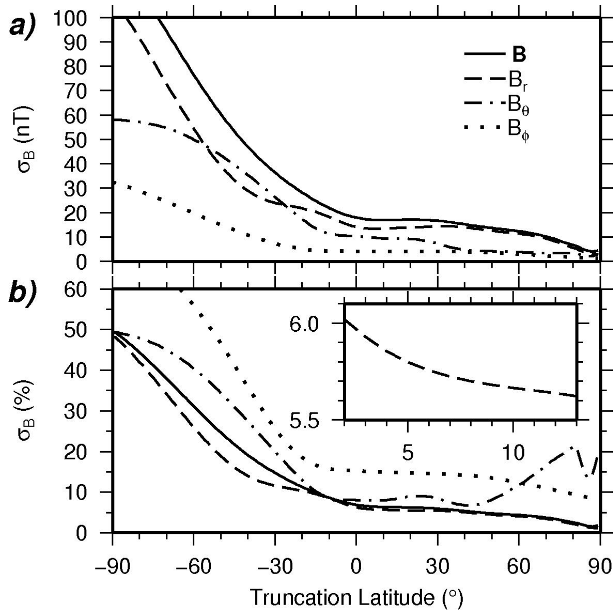

Figure 8: (a) Absolute and (b) relative misfits computed at constant altitude of 200 km, as a function of truncation latitude (see text), for $|\mathbf{B}|$ (solid line), B_r (dashed line), B_θ (dash-dotted line) and B_ϕ (dotted line). Inlet in (b) shows zoom-in for B_r around the transition from slow to rapid relative misfit change.

the limited data coverage over the northern hemisphere. We apply the procedure for $n_d = 19$ and for R_d = 640 km. In Figure 8 we show relative and absolute σ_B values for the vector field and individual components as a function of the truncation latitude, i.e., the southernmost latitude considered for the computation of σ_B. The field is computed and compared to the SH model on a regular grid of 2° resolution at 200-km altitude. We choose the truncation latitude where the relative misfit begins to rapidly increase, i.e. at latitude 7°N as more clearly shown in the inlet of Figure 8b.

We use the scheme described in Section 3.2 to choose the optimal model solution. The trade-off curve between σ_B and σ_M (Fig. 9) shows a similar behavior to that of the ideal case (Fig. 3). First, σ_B decreases to about 10% of its initial value while σ_M increases slowly. Then σ_B and σ_M evolve together, until σ_B reaches a plateau while σ_M continues to increase. The raw, filtered and exponentially fitted $-\Delta\sigma_B/\Delta\sigma_M$ curves are shown in Figure 9b. In this

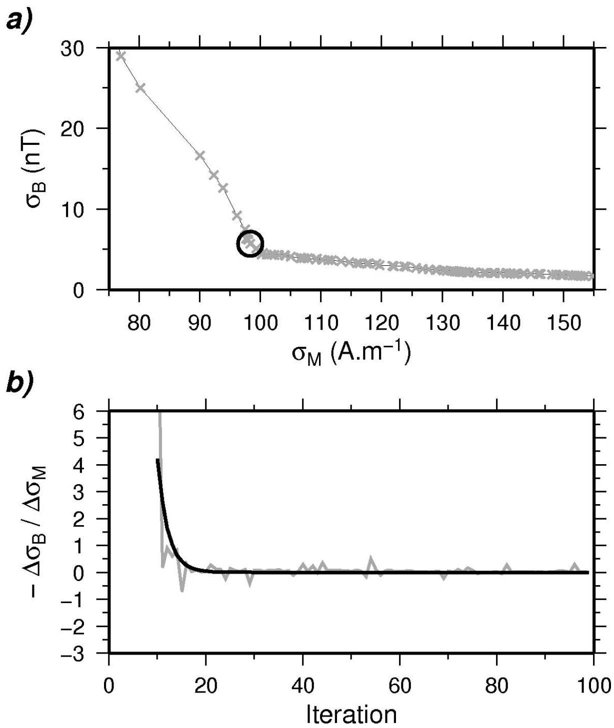

Figure 9: (a) Trade-off curve between σ_B and σ_M for consecutive iterations. (b) $-\Delta\sigma_B/\Delta\sigma_M$ as a function of the iteration number, with its exponential fit of the filtered curve (black line). The black circle in (a) shows σ_{B_j} and σ_{M_j} for the chosen iteration using (b), see Section 3.2 for details. The synthetic data is composed of two similar sidereal days by MESSENGER at two different epochs (an interval of 1 terrestrial year). The dipole mesh is located at 640 km depth with n_d = 19.

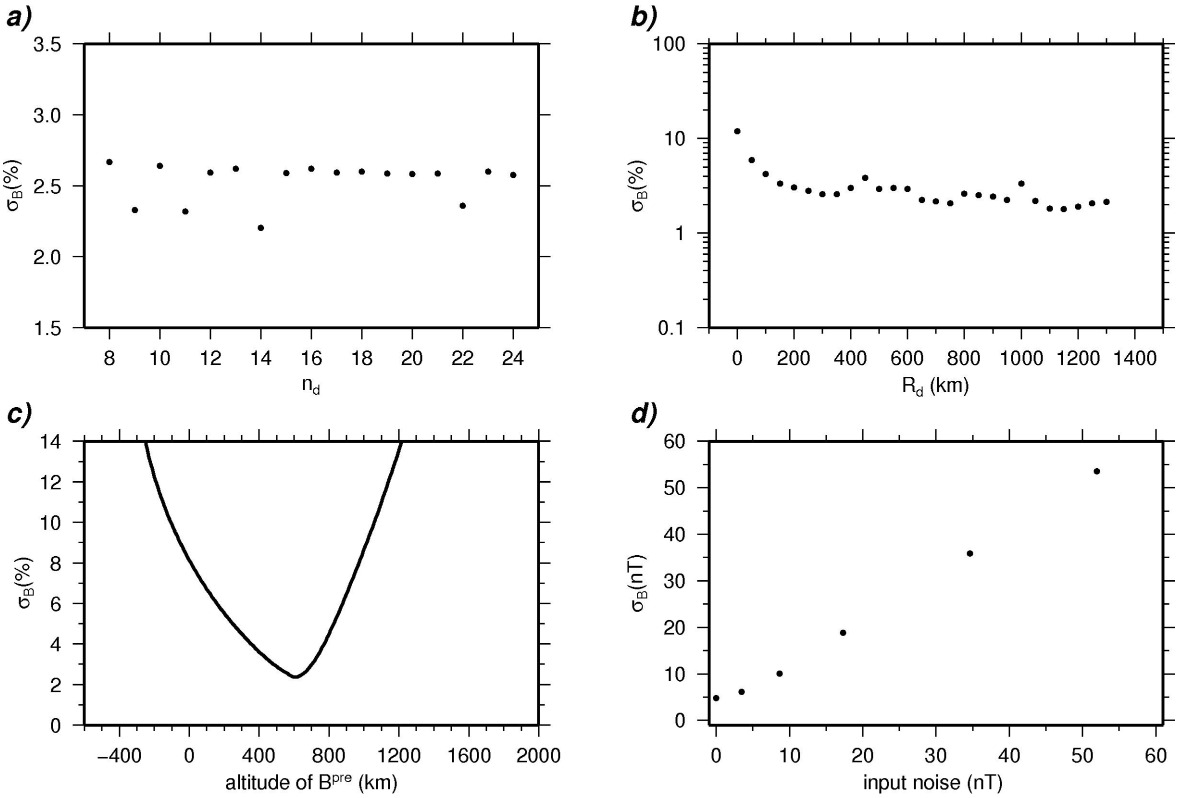

Figure 10: Relative magnetic field misfit as a function of (a) dipole mesh parameter n_d, (b) dipole mesh depth, (c) modeled magnetic field altitude. On (d) the absolute misfit is shown vs. the input white noise amplitude. For (a-d) the dipole mesh is 640-km deep and the dipole mesh parameter is set to $n_d = 19$ unless specified. Input data are predicted along MESSENGER orbits up to 1000 km altitude.

case the optimal solution is found at iteration 15, where the relative misfit is 2.59% and the correlation coefficient larger than 0.99.

The input dipole mesh resolution n_d is tested (Fig. 10a). We find an oscillatory dependence of the relative misfit for $n_d < 15$, which becomes nearly constant for larger n_d values. As for the ideal case, in the following we choose $n_d = 19$. Several dipole mesh depths R_d are also considered. The misfit is larger for shallower dipole meshes (R_d between 0 and 150 km), while for deeper meshes the relative σ_B oscillates between 2 and 4% (Fig. 10b). Contrary to the ideal case, we note that for deeper dipole meshes relative misfit values remain low. The altitude range where the field can be downward and upward continued is evaluated.

Retaining the relative difference between the SH field and that of the TD-ESD model to a maximum of 8% as acceptable, leads to an altitude range between 10 km and 970 km (Fig. 10c), which is narrower than for the ideal case. The minimum relative misfit is reached at an altitude of 600 km, corresponding to the average altitude of the synthetic data. Note that as opposed to the ideal case, in the realistic case σ_B is not symmetric about its minimum, and a better fit is obtained for lower than for higher altitudes. Finally we add to the measurements some noise. As for the ideal case, an almost linear dependency is found between σ_B and the amplitude of the white noise error added to the synthetic data (Fig. 10d). Without any noise, the misfit is around 4.81 nT (equivalent to a relative misfit of 2.59%), which we consider as the lowest error bound of our method in the realistic case.

Figure 11 shows maps of the radial component of the SV for the normal, fast and superfast TD-ESD models, as well as for the SH model from which synthetic data were generated, all at the same altitude for comparison. We obtain some pattern agreement above the northern hemisphere only using the fast and the superfast models. Correlation coefficients are 0.54 and 0.77, respectively. Comparing Figures 11b and 11c with 11d we find some morphological agreement, e.g., positive SV structures at mid-latitudes of longitudes 0-135°W and an intense negative structure at high-latitudes around longitude 180°. Also note that the SV recovered with TD-ESD has an increasing zonal component with decreasing SV magnitude (from superfast to normal models). Overall however, the recovery of the SV pattern by the fast and superfast models is not satisfactory. The situation is even worse for the normal SV model (Fig. 11a) where the correlation value is very low, only 0.07 above the northern hemisphere. Furthermore, the SV misfits of 1490%, 150% and 80% for the normal, fast and superfast models, respectively, are all too large. Above the southern hemisphere (not shown) the correlation coefficients are much lower, as expected. In summary, the TD-ESD is not able to properly recover the imposed SV pattern and magnitude. We note however that both SV pattern and magnitude recovery improve with increasing SV magnitude in the data used. Therefore, since a larger SV magnitude is not expected for Mercury (*Philpott et al.*, 2014), a

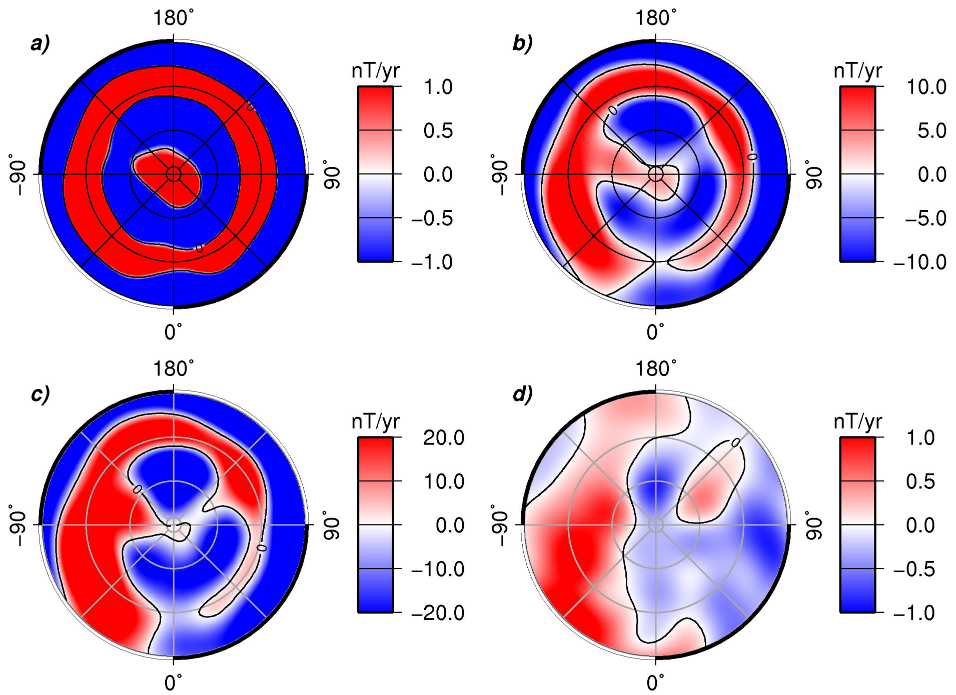

Figure 11: Radial SV recovered by TD-ESD from (a) normal, (b) fast and (c) superfast models. (d) SH synthetic radial SV for the normal model (the fast and superfast models are scaled by 10 and 20, respectively). Figures show maps at 200 km altitude of the northern hemisphere using a stereographic projection. The dipole mesh is located at a depth R_d = 640 km with a dipole parameter n_d = 19.

 DOI: 10.1002/2014JE004734

longer measurement time interval is needed in order to properly recover the Hermean SV.

These tests demonstrate that the TD-ESD can be used in the case of partial data coverage to successfully recover the morphology and intensity of the magnetic field of core origin. It is more difficult to correctly recover the secular variation, especially when it is slow. From these tests, we used in the following $n_d = 19$ and $R_d = 640$ km to produce maps of the Hermean magnetic field based on MESSENGER measurements. We emphasize that the field models were constructed without solving for SV terms.

5 Application to MESSENGER measurements

We now consider the magnetic field of Mercury as measured by MESSENGER during the first four Hermean sideral days. We define an external field proxy which is sensitive to the frequency content of the magnetic field measurements. It is used to select measurements less perturbed by the external component along MESSENGER orbit. First a low-pass cosine filter with 1-second bandwidth is applied to remove the high frequency signal. We then use a 10-seconds moving average in order to smooth the filtered signal. The proxy contains the high-frequency signal that is obtained by subtracting the low-pass smoothed filtered signal from the measurements (Fig. 12). High frequency variations are usually present outside the magnetosphere and when crossing the magnetopause. We assume that proxy intensities lower than 1 nT correspond to MESSENGER being inside the magnetosphere or regions with low external activity. When the proxy values are larger than 1 nT, measurements are rejected. We show in Figure 12 the proxy for the magnetospheric transit on April 17, 2011. Proxy values larger than 1 nT are found on the day side with positive X values in Mercury Solar Orbital (MSO) coordinate system. On the night side the proxy remains lower than 1 nT. In addition, only measurements obtained below 1000-km altitude are kept as illustrated by the vertical dashed lines. The magnetic field measurements acquired during the interval delimited by the vertical dashed lines are those selected for this orbit. As seen in Figure

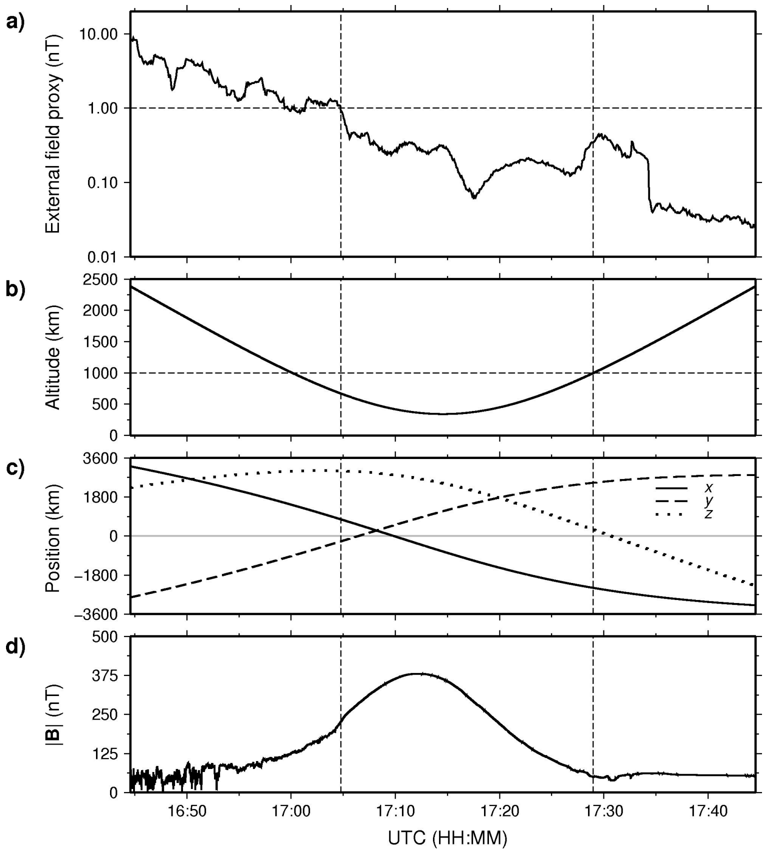

Figure 12: Fly of MESSENGER spacecraft inside the magnetosphere for April 17, 2011. (a) External field Proxy, (b) spacecraft altitude from Mercury's surface in kilometers, (c) x,y,z MESSENGER orbit positions in MSO coordinates, and (d)intensity of the observed magnetic field in nT; all as a function of time. The proxy intensity value of 1 nT is used as the first criterion on data selection for the inversion (see horizontal line in (a)). The altitude of 1000 km is used as a second criterion (see horizontal line in (b)). Vertical dashed lines delimit the interval during which measurements are selected for this orbit.

 DOI: 10.1002/2014JE004734

12d, the field intensity shows a clear internal dipolar signature, with the field becoming more intense at lower altitudes and close to the pole.

Data are selected during 59 consecutive days (corresponding to 1 sidereal day of the planet) to get a complete azimuthal coverage in the Mercury body fixed (MBF) coordinate system. During this period, MESSENGER completed 117 orbits. The angular distance between two consecutive orbits at the equator is about 3°.

The TD-ESD method is applied to the first four individual sidereal days. We do not solve for any temporal evolution, i.e., we assign the same epoch to all measurements of a given sidereal day. Maps of the chosen model of the Hermean magnetic field intensity $|\mathbf{B}|$ and its spherical components, B_r, B_θ, B_ϕ, are plotted for these four sidereal days at 200 km altitude in Figure 13. Only the northern hemisphere is shown because MESSENGER's eccentric orbit precludes reliable modeling of the internal field in the southern hemisphere (see Fig. 8). The maximum absolute radial field B_r is located at the north pole region, and the magnetic equator ($B_r = 0$) is seen at low latitudes of the northern hemisphere. The B_θ component is negative everywhere. The B_ϕ component is much weaker than the other two components.

We observe for all three components small scale features which seem to move around the rotation axis from one sidereal day to another; this is particularly clear for B_θ and B_ϕ. Because of the 3:2 spin-orbit resonance, the planet completes one solar day in 3 sidereal days (176 Earth days). During this time, every MBF longitude experiences all local time conditions. We thus interpret the rotating features as likely of external origin, related to the Sun varying position in the MBF frame. This hypothesis is supported by the comparison between the first and fourth sidereal days (with identical Sun positions) where the small scale features exhibit similar spatial distributions.

The corresponding residuals (unmodeled fields at spacecraft location) are shown in Figure 14 for the descending track. Strong positive B_r residuals are found north of 60°N, in the same region of the cusps identified by *Johnson et al.* (2012). There are also orbit-to-orbit differences in the residuals related to the fact that during the 12-hour interval between two

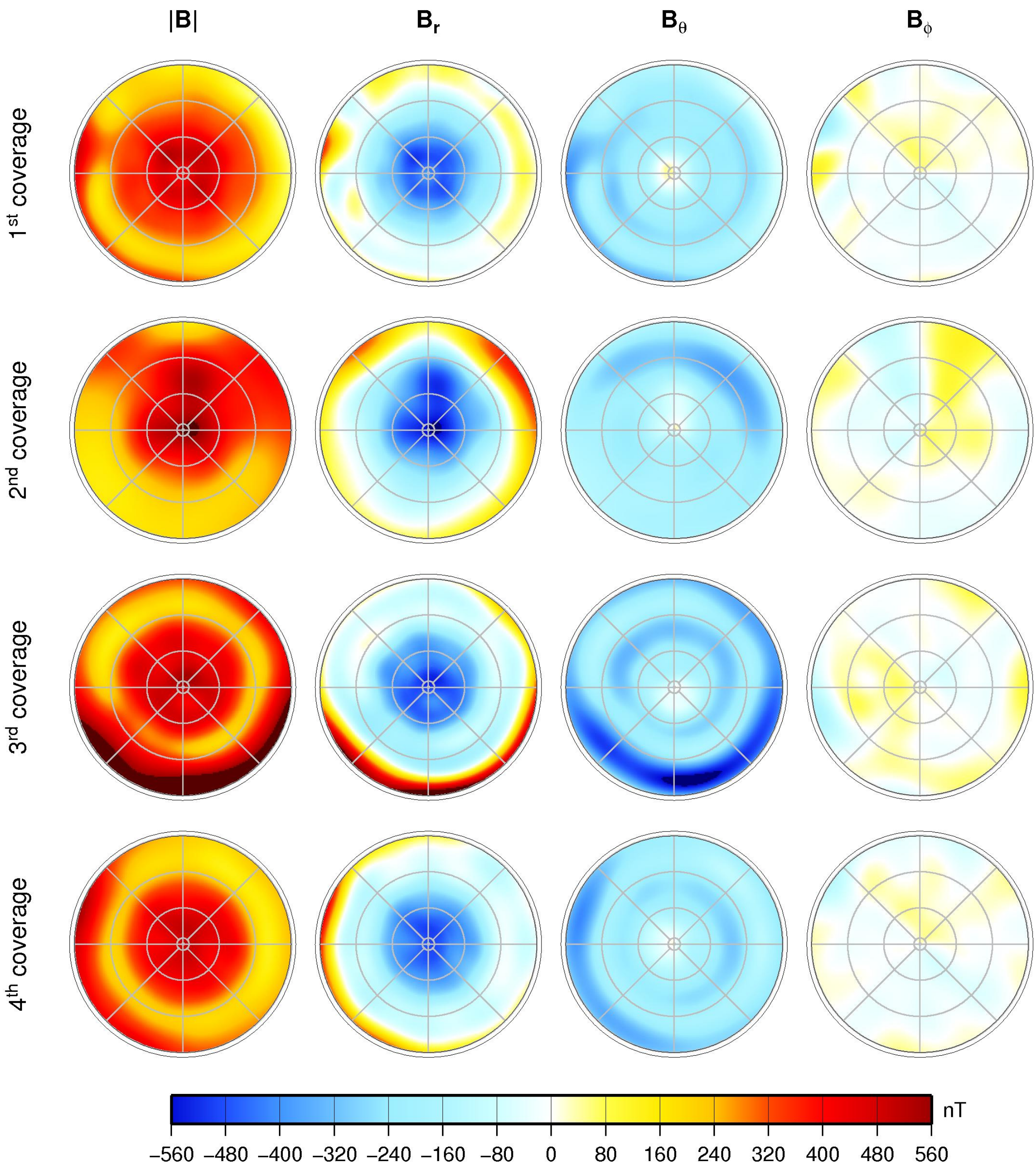

Figure 13: TD-ESD modeled magnetic field maps above the northern hemisphere of Mercury at 200 km altitude in MBF coordinates for the mean epochs of the first four MESSENGER sidereal days. The magnetic field unit is nT. Grid lines (grey) are drawn every 45° for longitude and every 30° for latitude. The maps are shown in stereographic projection. The 0° MBF longitude is toward bottom.

 DOI: 10.1002/2014JE004734

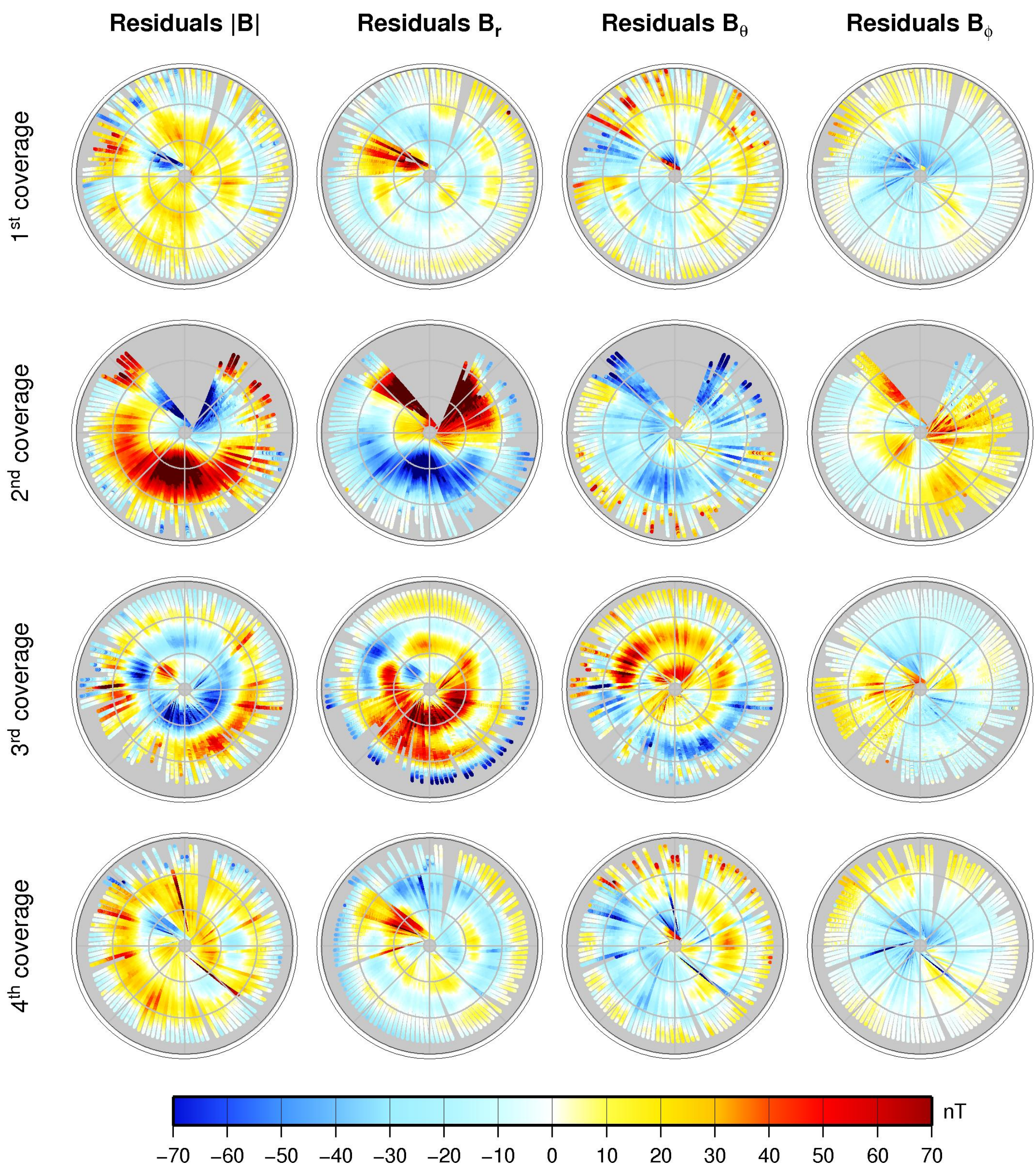

Figure 14: Magnetic field residual maps above the northern hemisphere of Mercury at 200 km altitude in MBF coordinates for the mean epochs of the first four MESSENGER sidereal days. Grid lines (grey) are drawn every 45° for longitude and every 30° for latitude. The maps are shown in stereographic projection. The 0° MBF longitude is toward bottom.

successive tracks the magnetospheric activity related to particles from solar wind and reconnection processes may drastically change (*Johnson et al.*, 2012). During the second sidereal day there is a measurement gap of about 20 orbits, during which the MAG instrument did not acquire data. That may explain the increased deviation of the maximum absolute radial field from the geographical pole (Fig. 13). As with the field components, the residuals also display some repeating features after one complete solar day (or 3 consecutive sidereal days), which can again be associated with periodic external sources. Indeed we observe very similar signatures for the 1st and 4th sidereal days, e.g., in the B_ϕ map the positive residuals at 45°E and at low latitudes between 135°E and 270°E. Similar rotating features can be observed for the other components as well (Figs. 13 and 14). This means that when using only one sidereal day some but not all external field contributions are naturally not modeled by our approach.

Table 1 shows statistics of the field models. The relative B_ϕ misfit is much larger than those of the other components because its magnitude is the lowest. The correlation coefficients are well above the level of statistical significance. The B_ϕ correlation coefficient is lower than those of the other components. Because the model is characterized by a field which is dominantly axisymmetric, the measured B_ϕ component is obviously less modeled using our approach, confirming that this measured component is likely dominated by the external field.

Misfit values also change from one sidereal day to another, but they tend to remain consistent with smallest values for the magnetic field intensity and the radial component, intermediate values for the latitudinal component and highest values for the longitudinal component. We note that when the rms of the observed field increases from one sidereal day to another the corresponding residuals also increase. We also compare values for the first and fourth sidereal days, corresponding to similar Sun-Mercury orientations. The larger relative misfit values observed during the fourth sidereal day may be related to the larger rms measured field, and are probably related to stronger external field during that sidereal day (for instance

Table 1: Number of observations retained for inversion, rms of the observed field, iteration chosen, relative misfit and correlation coefficients between the observed field and the model. The observed field rms, the inversion misfit and the correlation coefficient are given for the magnetic field vector and its spherical components B_r, B_θ and B_ϕ. Values for one-solar-day model are also shown.

Sidereal day	No. of Obs.	Observed field rms (nT)				Iteration	σ_B (nT)				Corr. Coeff.			
		$\mathbf{B}$	B_r	B_θ	B_ϕ		$\mathbf{B}$	B_r	B_θ	B_ϕ	$\mathbf{B}$	B_r	B_θ	B_ϕ
1	86134	275.3	238.9	133.4	28.7	23	31.8	16.4	18.0	20.5	0.98	0.99	0.96	0.71
2	68971	291.2	252.1	141.3	35.7	7	57.6	46.4	27.5	20.2	0.94	0.95	0.94	0.83
3	89947	281.2	242.0	139.6	32.2	14	42.2	27.9	24.2	20.4	0.96	0.98	0.93	0.78
4	88649	292.5	258.7	132.7	31.8	14	41.0	22.4	24.7	23.8	0.97	0.99	0.92	0.65
One-solar-day	245052	282.0	243.8	138.1	32.1	14	50.4	23.5	31.1	32.0	0.94	0.99	0.87	0.05

due to a possible increase of the solar activity).

We also apply the TD-ESD method to the set of all measurements of the first 3 consecutive sidereal days during a total period of one solar day, again using the mean epoch as the common time. There are two main advantages over considering an individual sidereal day. First, there are (roughly) three times the number of observations, which may improve the signal-to-noise ratio provided that the signal we seek to model is coherent. Second, all local times are sampled during a solar day, meaning that the external field is measured three times at a given location under three different Sun-Mercury orientations, while the internal field remains practically constant. For this preliminary computation we do not attempt to recover the SV of the magnetic field, based on results in Section 4. Moreover, external and internal fields vary differently with altitude and very small length scales at spacecraft altitudes are probably of external origin. It is therefore expected that the high frequency external field contributions are significantly reduced in the one-solar-day model.

We use the technique described in section 3.2 to obtain the model. In general the model changes very little with the iteration number (see Supporting Information). Residual statistics of the one-solar-day field model are also given in Table 1. The radial component is modeled with a misfit value of 23.5 nT (relative misfit of 9.6%) and a correlation coefficient exceeding 0.99. The misfit values for the one-solar-day B_θ and B_ϕ are larger than for the individual sidereal days. This is interpreted as the one-solar-day field model being less contaminated by external field contributions than models based on individual sidereal days. The observed B_ϕ component is obviously poorly explained by the dominantly axisymmetric model, since σ_{B_ϕ} is the same order of magnitude as the observed rms B_ϕ (see Table 1), possibly indicating that this component is mainly of external origin.

We show in Figure 15 maps of the modeled magnetic field intensity and vector components for the first solar day of MESSENGER. The modeled field is much more axisymmetric than in the individual sidereal days. This axisymmetry can be quantified by the percentage of non-zonal modeled magnetic field, which is equal to 4.1% and 4.9% for the B_r and B_θ

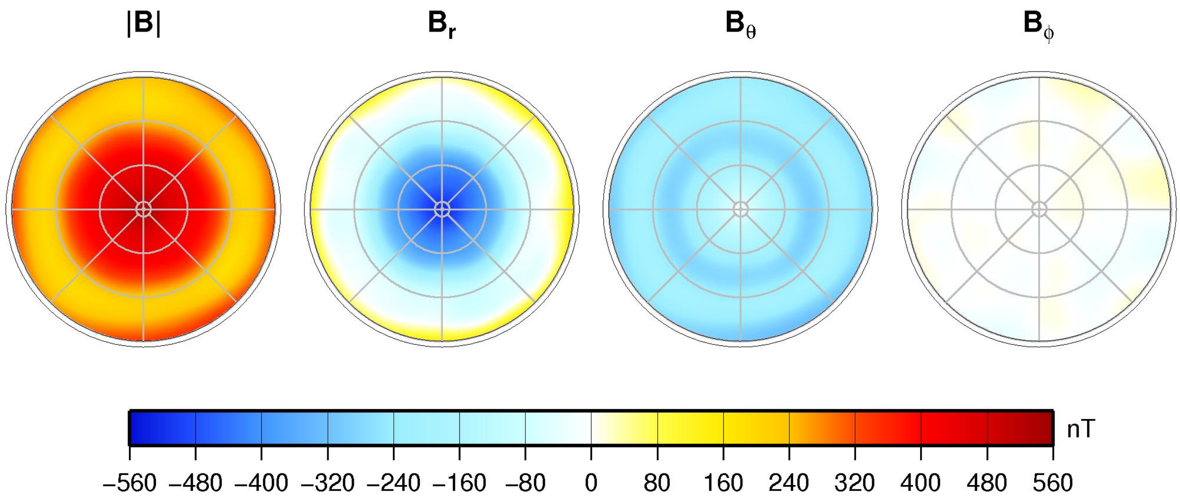

Figure 15: Stereographic projection maps of the magnetic field intensity $|\mathbf{B}|$ and its spherical components B_r, B_θ, B_ϕ, for the first solar day of MESSENGER measurements. Maps represent the northern hemisphere of Mercury at 200 km altitude, in MBF coordinates. Grid lines (grey) are drawn every 45° for longitude and every 30° for latitude. The 0° MBF longitude is toward bottom.

components, respectively. The much smaller values of B_ϕ compared to the other components are also consistent with a dominantly axisymmetric internal field. The maximum value of the radial component is found at a latitude exceeding 89°N. The magnetic equator $B_r = 0$ is found in the northern hemisphere, and its position fluctuates between 6°N and 20°N. These results are qualitatively consistent with an axial and northward offset internal dipole pointing southward (*Anderson et al.*, 2012; *Johnson et al.*, 2012). We discuss this point in the following Section.

The axisymmetric dominance of the one-solar-day field model motivates examining the zonal radial field profile (Fig. 16). The associated standard deviation (i.e., the rms of the non-zonal field at each latitude) is also shown. Based on this profile, the mean magnetic equator $B_r = 0$ position is around 10°N latitude. This estimate has lower and upper bounds at 7.7° and 12.6°N latitude, respectively.

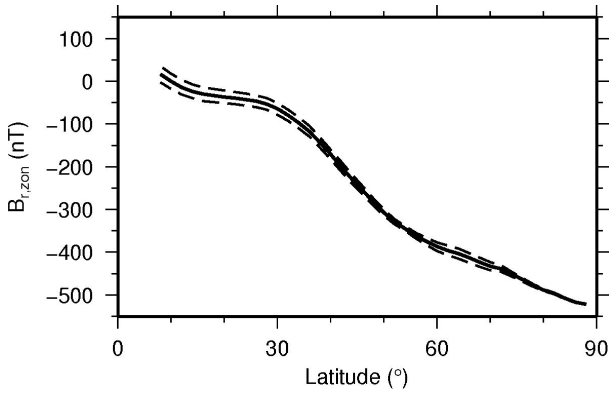

Figure 16: Zonal radial magnetic field (black solid line) with one standard deviation bounds (dashed lines, representing rms non-zonal field), as a function of latitude. Only latitudes higher than 7°N (see Fig. 8b) are shown.

6 Discussion

6.1 MESSENGER one-solar-day model

We now compare the statistics of our field models with previously published models. We obtain misfits to the measurements of the vector **B** of ∼40 nT for the individual sidereal days and 50.4 nT for the one-solar-day. These are larger than 10.7 nT obtained by *Alexeev et al.* (2010) and 20 nT by *Johnson et al.* (2012), but these models explicitly accounted for external field sources, which we do not do in the current approach. In the individual sidereal day inversions some external fields may leak into our models. This effect is greatly reduced in the one-solar-day inversion, as evident from the larger misfit spatially correlated with the Sun position in the MBF frame and the null correlation coefficient between the observed and modeled B_ϕ component.

While the sidereal day models are dominated by zonal fields with some non-zonal contribution, the latter almost vanishes when considering the one-solar-day model. We interpret these non-zonal fields as being the signature of time-variable external fields. However, any non-axisymmetric field of internal origin is expected to remain after the time-averaging of one solar day. We therefore conclude that the internal field of Mercury is strongly axisymmetric.

A purely zonal field in general, and near zero dipole tilt in particular, are in contradiction to Cowling's anti-dynamo theorem (*Cowling*, 1934). For example, the purely axisymmetric field model of Saturn (*Connerney et al.*, 1982; *Cao et al.*, 2011) is enigmatic. Exotic mechanisms were proposed to explain it, most notably a conducting non-convecting envelope surrounding the dynamo region of Saturn (*Stevenson*, 1980, 1982; *Schubert et al.*, 2004). The Hermean internal field axysimmetry is therefore challenging for dynamo modeling.

6.2 Magnetic equator

Anderson et al. (2012) studied the position Z_{ρ_0} of the magnetic equator in cylindrical coordinates ($B_\rho = 0$). They identified the magnetic equator crossings directly from measurements and found an average axial displacement of $\mathrm{Z}_{\rho_0} = 479 \pm 6$ km northward using the low-altitude crossings. The average magnetic equator position value for the high-altitude crossings is also around the same value, in agreement with a northward dipole offset. Figure 17 shows Z_{ρ_0} of our one-solar-day model as a function of the distance to the planet rotation axis ρ (in MSO cylindrical coordinates), for different altitudes and longitudes, in comparison with the values found by *Anderson et al.* (2012). We consider only altitudes up to 1000 km, because relatively low misfit values were obtained for predicted magnetic field maps above that limit (see section 4.3). For each altitude, our magnetic equator position varies with longitude. Our Z_{ρ_0} values partially overlap the crossings positions (grey region in Figure 17) observed by *Anderson et al.* (2012). However, our average Z_{ρ_0} changes with ρ, in contradiction to the dipole offset model, although a constant Z_{ρ_0} could be consistent with the range of variability. Our average Z_{ρ_0} is larger than that of *Anderson et al.* (2012). In the context of a dipole offset model this larger Z_{ρ_0} would correspond to a larger g_2^0/g_1^0 ratio.

Parametric studies of numerical dynamo models found two main types of solutions: when convection is vigorous and rotational effects are moderate, a large g_2^0/g_1^0 ratio may be found but a large non-zonal field is also present; when convection is moderate and rotational effects

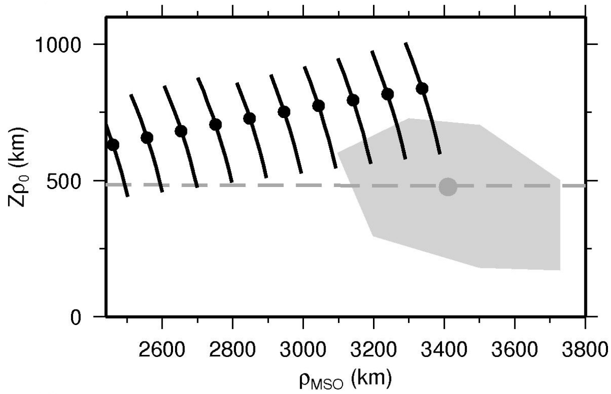

Figure 17: Cylindrical magnetic equator $B_\rho = 0$ axial displacement Z_{ρ_0} as a function of the distance to the planet rotation axis ρ, in MSO frame. Values were obtained from the one-solar-day model for different altitudes and longitudes (black lines). The black dots correspond to the average Z_{ρ_0} value for the corresponding altitude. Average (Z_{ρ_0}, ρ_{MSO}) pair for the low-altitude equator crossings of *Anderson et al.* (2012) is also plotted (grey dot). The grey region indicates where magnetic equator crossings were detected, and the grey dashed line is based on the estimate from the SH model of *Anderson et al.* (2012).

 DOI: 10.1002/2014JE004734

are vigorous, a small non-zonal field is found but the g_2^0/g_1^0 ratio is also small (*Kutzner and Christensen*, 2002; *Christensen and Aubert*, 2006). Heterogeneous CMB heat flux can help to obtain a large g_2^0/g_1^0 ratio together with small non zonal terms, as was applied to the paleo-dynamo of Mars (*Stanley et al.*, 2008; *Amit et al.*, 2011; *Dietrich and Wicht*, 2013), but there is no solid evidence for hemispheric mantle heterogeneity in Mercury. The large g_2^0/g_1^0 ratio found by *Anderson et al.* (2012) together with the very axisymmetric field confirmed by our study are therefore challenging constraints for Mercury dynamo models (*Cao et al.*, 2014; *Wicht and Heyner*, 2014).

6.3 Can temporal variations be modeled?

Using the TD-ESD method we demonstrate that a purely internal magnetic field can be correctly described in a limited region of the planet's neighborhood, with low misfits (below 5 nT) and close to unity correlation coefficients, even when only a partial dataset is available (i.e., corresponding to the case of MESSENGER). This low misfit may be seen as the modeling limit of our method.

The case is different for the SV field. Using a global and regular data distribution and assuming SV characteristic timescales (*Hulot and Le Mouël*, 1994) identical to the Earth's (normal SV), we were unable to correctly model the SV when using synthetic measurements separated by one year. With this ideal data coverage, the fast and superfast SV models can nonetheless be correctly reproduced, with a correlation coefficient exceeding 0.99 and relative misfits below 8.1%. For a partial data coverage, even the superfast SV model cannot be adequately recovered: although the correlation coefficients are statistically significant, the patterns are not sufficiently similar and the misfit values are too large.

The characteristic SV timescale is inversely proportional to the magnetic Reynolds number R_m (*Christensen and Tilgner*, 2004; *Lhuillier et al.*, 2011; *Christensen et al.*, 2012), so assuming Earth-like characteristic timescales on Mercury is equivalent to assuming an Earth-like magnetic Reynolds number for Mercury. Our normal SV model corresponds to the same characteristic timescales for the Earth and Mercury, i.e., the same R_m. Even if the SV was 20 times higher (superfast SV model), i.e., a characteristic timescale 20 times lower and an R_m 20 times higher, we would have not resolved the SV magnitude correctly. We therefore conclude that the time required for our TD-ESD method to detect Mercury's SV is larger than $20R_m^{\oplus}/R_m^M$ years, where $R_m^{\oplus}$ and R_m^M are the magnetic Reynolds numbers of the Earth and Mercury, respectively. This seemingly negative result was obtained by modeling the SV with two similar sidereal days separated by one Earth year. In the future, we hope that modeling the SV with shorter sampling times and covering longer time periods may yield a more encouraging lower bound on the required time to detect the Hermean SV with a MESSENGER-like orbit.

7 Conclusion

In this study we introduce the Time-Dependent Equivalent Source Dipole method to model the magnetic field of Mercury as measured by the MESSENGER spacecraft. This method was validated using synthetic internal magnetic field measurements, both located on regular grids at different altitudes and only along MESSENGER orbits above the northern hemisphere. We designed and validated a scheme to select a unique and optimal iteration as a solution. We evaluated the performance of the method in recovering an internal field as a function of several input parameters, including the dipole mesh horizontal resolution and depth. We found that an horizontal resolution of 9.6° (n_d = 19) offers a satisfying compromise between the fit to the measurements and the computational cost. We chose a dipole mesh depth of 640 km, within the range proposed by *Verhoeven et al.* (2009). We demonstrated that our results are weakly sensitive to the choice of dipole mesh depth (Fig. 10b), and shallower depths (*Hauck et al.*, 2013; *Rivoldini and Van Hoolst*, 2013) may also be considered.

Next we determined the altitude range where the modeled magnetic field can be reliably upward- or downward continued. This altitude range is -300 to 1460 km when using measurements ideally located on regular grids, and it is restricted to 10 to 970 km when using MESSENGER-like measurements. More importantly, this partial data coverage does not degrade the quality of the model above the northern hemisphere. The minimum latitude at which the field can be reliably modeled by our TD-ESD method is 7°N. Our tests also showed that it is impossible to adequately recover the SV within two individual sidereal days separated by one year.

We then applied our new modeling scheme to the MESSENGER measurements during the first 4 consecutive sidereal days after MAG instrument turned on (from March 23, 2011 to November 13, 2011). In order to reduce external magnetic field contributions, only measurements inside the magnetosphere were selected, using a proxy we defined. During these relatively short time intervals we did not attempt to model the SV. Five models were computed and compared, one for each sidereal day plus one additional model for the first solar day of Mercury. For each of the first four sidereal day models, a dominantly axisymetric field is observed. Small-scale features move around the rotation axis of the planet from one sidereal day to another, which we interpret as features of external origin related to the position of the Sun with respect to the planet. In the one-solar-day model (Fig. 15) most of the non-axisymmetric and small scale features vanish, supporting their external origin. This latter field model has a more axisymmetric signature than in individual sidereal days, with a very small non-zonal to total magnetic field ratio. This is in agreement with previous studies (*Anderson et al.*, 2012; *Johnson et al.*, 2012). We emphasize that using an inversion scheme which allows for non-axisymmetric and small-scale features to be modeled, we recover a large-scale and dominantly zonal one-solar-day magnetic field model. This feature continues to provide a challenge for dynamo modeling (*Wicht and Heyner*, 2014).

The TD-ESD method gives encouraging results for planetary magnetic field modeling. One advantage is the possibility to model the magnetic field of Mercury locally using a partial data set such as the one provided by MESSENGER and without any a priori regularization as previously used in SH models of Mercury (*Uno et al.*, 2009). In the future, TD-ESD will be applied to a larger set of MESSENGER measurements. This will lead to more accurate estimates for the field. Lower altitude measurements from the final phase of MESSENGER mission may give new information about smaller length scales of the magnetic field that are not detectable at higher altitudes. Selecting orbits during quiet Sun activity conditions may reduce the external effects (*Anderson et al.*, 2013), but it would reduce significantly the number of observations and might also decrease the spatial and temporal coverage of the modeled magnetic field. Another possibility to overcome the external field contamination is to use an alternative parameterization or to extend the TD-ESD method by jointly modeling the internal and external sources.

Our study helps to bring out all the difficulties met in using planetary-scale modeling methods when the data set is not globally distributed. It may guide in finding new approaches to constrain smaller scales of Mercury's magnetic field. In addition, our approach may be applied to model magnetic fields of other planets.

We argue that a strongly axisymmetric core field should be used as a constraint for modeling the Hermean dynamo. Our current view on the magnetic field of Mercury, based on limited spatial coverage, could change when more global measurements are available. The future BepiColombo mission of ESA/JAXA to Mercury (*Benkhoff et al.*, 2010) will map its magnetic field globally. For this future mission, global modeling methods will likely be more suitable than limited coverage methods . However, the TD-ESD method will still be appropriate to combine MESSENGER and BepiColombo measurements, in particular in order to detect and estimate the time changes of the Hermean magnetic field between these missions.

Acknowledgments

We thank Erwan Thébault, Michael Purucker, Melanie Drilleau and Johannes Wicht for insightful discussions. We are grateful to Catherine Johnson and Richard Holme, for comments and suggestions which helped to improve the manuscript. This work is partly funded through the ANR project MARMITE (ANR-13-BS05-0012) and PNP/ INSU/ CNRS program. M. A. Pais is supported by Fundação para a Ciência e Tecnologia (FCT: PTDC/CTE-GIX/119967/2010) and FEDER through the project COMPETE (FCOMP-01-0124-FEDER-019978). The data used in this study are available from the NASA Planetary Data System at http://ppi.pds.nasa.gov.

Supporting Information

Figure 18 shows the trade-off curve and three B_r maps of the one-solar-day model. The maps correspond to three different iterations with 20%, 10% and 5% threshold values (iteration 11, chosen iteration 14 and iteration 17, respectively). The corresponding misfit values for the magnetic field vector are 52.8 nT, 50.4 nT and 50.1 nT, respectively. Increasing number of iteration yields more intense small-scale radial field at low-latitudes. However, overall all three maps exhibit very similar patterns characterized by strongly axisymmetric large-scale field and $B_r = 0$ contour in the Northern hemisphere. We therefore conclude that our field model is weakly sensitive to our choice of iteration.

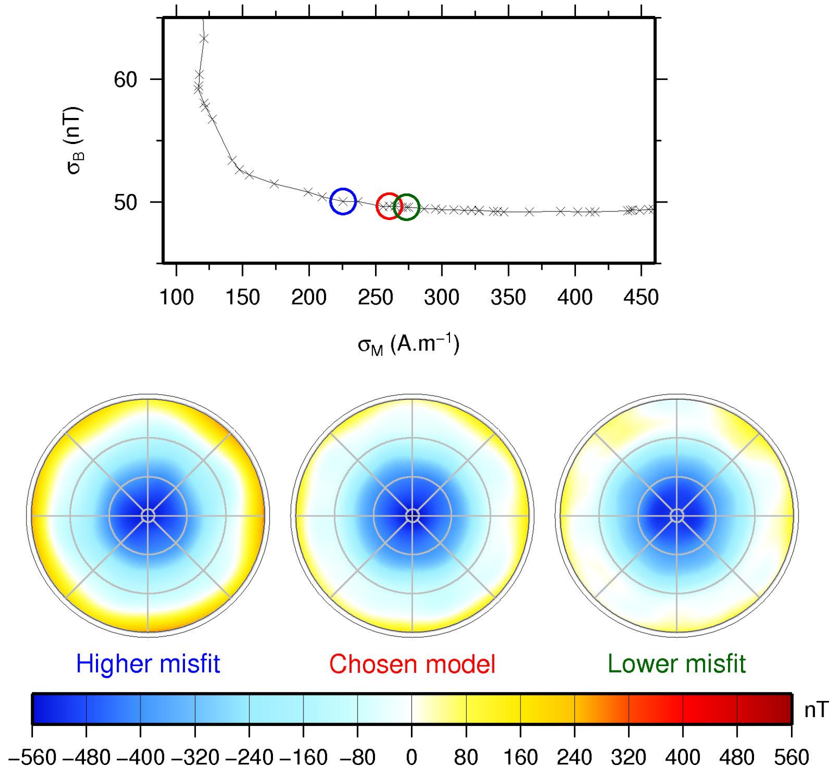

Figure 18: Top: Trade-off curve between σ_B and σ_M for the one solar day measured by MESSENGER spacecraft. Bottom: TD-ESD modeled radial magnetic field maps above the northern hemisphere at 200 km for three different iterations, the one giving Figure 16 and two others with higher and lower misfits (see circles in the trade-off curve).

 DOI: 10.1002/2014JE004734

References

Alexeev, I. I., E. S. Belenkaya, J. A. Slavin, H. Korth, B. J. Anderson, D. N. Baker, S. A. Boardsen, C. L. Johnson, M. E. Purucker, M. Sarantos, and S. C. Solomon (2010), Mercury's magnetospheric magnetic field after the first two MESSENGER flybys, *Icarus*, *209*, 23–39, doi:10.1016/j.icarus.2010.01.024.

Amit, H., U. R. Christensen, and B. Langlais (2011), The influence of degree-1 mantle heterogeneity on the past dynamo of Mars, *Phys. Earth Planet. Inter.*, *189*, 63–79, doi: 10.1016/j.pepi.2011.07.008.

Anderson, B. J., M. H. Acuña, D. A. Lohr, J. Scheifele, A. Raval, H. Korth, and J. A. Slavin (2007), The Magnetometer Instrument on MESSENGER, *Space Sci. Rev.*, *131*, 417–450, doi:10.1007/s11214-007-9246-7.

Anderson, B. J., M. H. Acuña, H. Korth, M. E. Purucker, C. L. Johnson, J. A. Slavin, S. C. Solomon, and R. L. McNutt (2008), The Structure of Mercury's Magnetic Field from MESSENGER's First Flyby, *Science*, *321*, 82–, doi:10.1126/science.1159081.

Anderson, B. J., M. H. Acuña, H. Korth, J. A. Slavin, H. Uno, C. L. Johnson, M. E. Purucker, S. C. Solomon, J. M. Raines, T. H. Zurbuchen, G. Gloeckler, and R. L. McNutt (2010), The Magnetic Field of Mercury, *Space Sci. Rev.*, *152*, 307–339, doi:10.1007/s11214-009-9544-3.

Anderson, B. J., C. L. Johnson, H. Korth, M. E. Purucker, R. M. Winslow, J. A. Slavin, S. C. Solomon, R. L. McNutt, J. M. Raines, and T. H. Zurbuchen (2011), The Global Magnetic Field of Mercury from MESSENGER Orbital Observations, *Science*, *333*, 1859–1862, doi:10.1126/science.1211001.

Anderson, B. J., C. L. Johnson, H. Korth, R. M. Winslow, J. E. Borovsky, M. E. Purucker, J. A. Slavin, S. C. Solomon, M. T. Zuber, and R. L. McNutt, Jr. (2012), Low-degree structure in Mercury's planetary magnetic field, *J. Geophys. Res.*, *117*, E00L12, doi: 10.1029/2012JE004159.

Anderson, B. J., C. L. Johnson, and H. Korth (2013), A magnetic disturbance index for Mercury's magnetic field derived from MESSENGER Magnetometer data, *Geochem. Geophys. Geosyst.*, *14*, 3875–3886, doi:doi:10.1002/ggge.20242.

Benkhoff, J., J. van Casteren, H. Hayakawa, M. Fujimoto, H. Laakso, M. Novara, P. Ferri, H. R. Middleton, and R. Ziethe (2010), BepiColombo - Comprehensive exploration of Mercury: Mission overview and science goals, *Planet. Space Sci.*, *58*, 2–20, doi: 10.1016/j.pss.2009.09.020.

Cain, J. C., Z. Wang, C. Kluth, and D. R. Schmitz (1989), Derivation of a geomagnetic model to n = 63, *Geophys. J.*, *97*, 431–441.

Cao, H., C. T. Russell, U. R. Christensen, M. K. Dougherty, and M. E. Burton (2011), Saturn's very axisymmetric magnetic field: No detectable secular variation or tilt, *Earth Planet. Sci. Lett.*, *304*, 22–28, doi:10.1016/j.epsl.2011.02.035.

Cao, H., J. M. Aurnou, J. Wicht, W. Dietrich, K. M. Soderlund, and C. T. Russell (2014), A dynamo explanation for mercurys anomalous magnetic field, *Geophys. Res. Lett.*, *41*, doi:10.1002/2014GL060196.

Christensen, U. R., and J. Aubert (2006), Scaling properties of convection driven dynamos in rotating spherical shells and application to planetary magnetic fields, *Geophys. J. Int.*, *166*, 97–114, doi:10.1111/j.1365-246X.2006.03009.x.

Christensen, U. R., and A. Tilgner (2004), Power requirement of the geodynamo from ohmic losses in numerical and laboratory dynamos, *Nature*, *429*, 169–171, doi: 10.1038/nature02508.

Christensen, U. R., J. Aubert, and G. Hulot (2010), Conditions for Earth-like geodynamo models, *Earth and Planetary Science Letters*, *296*, 487–496, doi:10.1016/j.epsl.2010.06.009.

Christensen, U. R., I. Wardinski, and V. Lesur (2012), Timescales of geomagnetic secular acceleration in satellite field models and geodynamo models, *Geophys. J. Int.*, *190*, 243–254, doi:10.1111/j.1365-246X.2012.05508.x.

Connerney, J. E. P., N. F. Ness, and M. H. Acuna (1982), Zonal harmonic model of Saturn's magnetic field from Voyager 1 and 2 observations, *Nature*, *298*, 44–46, doi:10.1038/298044a0.

Connerney, J. E. P., M. H. Acuna, and N. F. Ness (1987), The magnetic field of Uranus, *J. Geophys. Res.*, *92*, 15,329–15,336, doi:10.1029/JA092iA13p15329.

Connerney, J. E. P., M. H. Acuna, and N. F. Ness (1991), The magnetic field of Neptune, *J. Geophys. Res.*, *96*, 19,023.

Cowling, T. G. (1934), The stability of gaseous stars, *Monthly Notices of the Royal Astronomical Society*, *94*, 768–782.

Dietrich, W., and J. Wicht (2013), A hemispherical dynamo model: Implications for the Martian crustal magnetization, *Phys. Earth Planet. Inter.*, *217*, 10–21, doi:10.1016/j.pepi.2013.01.001.

Dyment, J., and J. Arkani-Hamed (1998), Equivalent source magnetic dipoles revisited, *Geophys. Res. Lett.*, *25*(11), 2003–2006, doi:10.1029/98GL51331.

Emilia, D. A. (1973), Equivalent sources used as an analytic base for processing total magnetic field profiles, *Geophysics*, *38*, 339, doi:10.1190/1.1440344.

Gubbins, D. (2004), *Time Series Analysis and Inverse Theory for Geophysicists*, pp. 272. ISBN 0521819652. Cambridge, UK: Cambridge University Press, April 2004.

Hauck, S. A., J.-L. Margot, S. C. Solomon, R. J. Phillips, C. L. Johnson, F. G. Lemoine, E. Mazarico, T. J. McCoy, S. Padovan, S. J. Peale, M. E. Perry, D. E. Smith, and M. T. Zuber (2013), The curious case of Mercury's internal structure, *J. Geophys. Res.*, *118*, 1204–1220, doi:10.1002/jgre.20091.

Holme, R., and J. Bloxham (1996), The magnetic fields of Uranus and Neptune: Methods and models, *J. Geophys. Res.*, *101*, 2177–2200, doi:10.1029/95JE03437.

Hulot, G., and J. L. Le Mouël (1994), A statistical approach to the Earth's main magnetic field, *Phys. Earth Planet. Inter.*, *82*, 167–183, doi:10.1016/0031-9201(94)90070-1.

Johnson, C. L., M. E. Purucker, H. Korth, B. J. Anderson, R. M. Winslow, M. M. H. Al Asad, J. A. Slavin, I. I. Alexeev, R. J. Phillips, M. T. Zuber, and S. C. Solomon (2012), MESSENGER observations of Mercury's magnetic field structure, *J. Geophys. Res.*, *117*, E00L14, doi:10.1029/2012JE004217.

Katanforoush, A., and M. Shahshahani (2003), Distributing Points on the Sphere, *Experimental Mathematics*, *12*, 199–209.

Kutzner, C., and U. R. Christensen (2002), From stable dipolar towards reversing numerical dynamos, *Phys. Earth Planet. Inter.*, *131*, 29–45, doi:10.1016/S0031-9201(02)00016-X.

Langlais, B., and M. Purucker (2007), A polar magnetic paleopole associated with Apollinaris Patera, Mars, *Planet. Space Sci.*, *55*, 270–279, doi:10.1016/j.pss.2006.03.008.

Langlais, B., M. E. Purucker, and M. Mandea (2004), Crustal magnetic field of Mars, *J. Geophys. Res.*, *109*, E02,008, doi:10.1029/2003JE002048.

Lhuillier, F., J. Aubert, and G. Hulot (2011), Earth's dynamo limit of predictability controlled by magnetic dissipation, *Geophys. J. Int.*, *186*, 492508, doi:10.1111/j.1365-246X.2011.05081.x.

Margot, J. L., S. J. Peale, R. F. Jurgens, M. A. Slade, and I. V. Holin (2007), Large Longitude Libration of Mercury Reveals a Molten Core, *Science*, *316*, 710–714, doi: 10.1126/science.1140514.

Maus, S., M. Rother, C. Stolle, W. Mai, S. Choi, H. Lühr, D. Cooke, and C. Roth (2006), Third generation of the Potsdam Magnetic Model of the Earth (POMME), *J. Geophys. Res.*, *7*, Q07008, doi:10.1029/2006GC001269.

Mayhew, M. A. (1979), Inversion of satellite magnetic anomaly data, *J. Geophys.*, *45*, 119–128.

Ness, N. F., K. W. Behannon, R. P. Lepping, Y. C. Whang, and K. H. Schatten (1974), Magnetic Field Observations near Mercury: Preliminary Results from Mariner 10, *Science*, *185*, 151–160, doi:10.1126/science.185.4146.151.

Ness, N. F., K. W. Behannon, R. P. Lepping, and Y. C. Whang (1975), The magnetic field of Mercury. I, *J. Geophys. Res.*, *80*, 2708–2716, doi:10.1029/JA080i019p02708.

Philpott, L. C., C. L. Johnson, R. M. Winslow, B. J. Anderson, H. Korth, M. E. Purucker, and S. C. Solomon (2014), Constraints on the secular variation of Mercury's magnetic field from the combined analysis of MESSENGER and Mariner 10 data, *Geophys. Res. Lett.*, *41*, 6627–6634, doi:10.1002/2014GL061401.

Plagemann, S. (1965), Model of the Internal Constitution and Temperature of the Planet Mercury, *J. Geophys. Res.*, *70*, 985–993, doi:10.1029/JZ070i004p00985.

Press, W. H., B. P. Flannery, S. A. Teukolsky, and W. T. Vetterling (1989), *Numerical recipes in Pascal. The art of scientific computing*.

Purucker, M., D. Ravat, H. Frey, C. Voorhies, T. Sabaka, and M. Acuña (2000), An altitude-normalized magnetic map of Mars and its interpretation, *Geophys. Res. Lett.*, *27*, 2449–2452, doi:10.1029/2000GL000072.

Purucker, M., B. Langlais, N. Olsen, G. Hulot, and M. Mandea (2002), The southern edge of cratonic North America: Evidence from new satellite magnetometer observations, *Geophys. Res. Lett.*, *29*, 56–156–4, doi:10.1029/2001GL013645.

Purucker, M. E., T. J. Sabaka, and R. A. Langel (1996), Conjugate gradient analysis: A new tool for studying satellite magnetic data sets, *Geophys. Res. Lett.*, *23*, 507–510, doi:10.1029/96GL00388.

Purucker, M. E., R. A. Langel, M. Rajaram, and C. Raymond (1998), Global magnetization models with a priori information, *J. Geophys. Res.*, *103*, 2563–2584, doi:10.1029/97JB02935.

Purucker, M. E., J. W. Head, III, and L. Wilson (2012), Magnetic signature of the lunar South Pole-Aitken basin: Character, origin, and age, *J. Geophys. Res.*, *117*, E05001, doi:10.1029/2011JE003922.

Rivoldini, A., and T. Van Hoolst (2013), The interior structure of Mercury constrained by the low-degree gravity field and the rotation of Mercury, *Earth Planet. Sci. Lett.*, *377*, 62–72, doi:10.1016/j.epsl.2013.07.021.

Schubert, G., K. H. Chan, X. Liao, and K. Zhang (2004), Planetary dynamos: effects of electrically conducting flows overlying turbulent regions of magnetic field generation, *Icarus*, *172*, 305–315, doi:10.1016/j.icarus.2004.06.007.

Smith, D. E., M. T. Zuber, R. J. Phillips, S. C. Solomon, S. A. Hauck, F. G. Lemoine, E. Mazarico, G. A. Neumann, S. J. Peale, J.-L. Margot, C. L. Johnson, M. H. Torrence, M. E. Perry, D. D. Rowlands, S. Goossens, J. W. Head, and A. H. Taylor (2012), Gravity Field and Internal Structure of Mercury from MESSENGER, *Science*, *336*, 214–217, doi:10.1126/science.1218809.

Solomon, S. C., R. L. McNutt, R. E. Gold, M. H. Acuña, D. N. Baker, W. V. Boynton, C. R. Chapman, A. F. Cheng, G. Gloeckler, J. W. Head, III, S. M. Krimigis, W. E. Mc-

Clintock, S. L. Murchie, S. J. Peale, R. J. Phillips, M. S. Robinson, J. A. Slavin, D. E. Smith, R. G. Strom, J. I. Trombka, and M. T. Zuber (2001), The MESSENGER mission to Mercury: scientific objectives and implementation, *Planet. Space Sci.*, *49*, 1445–1465, doi:10.1016/S0032-0633(01)00085-X.

Stanley, S., L. Elkins-Tanton, M. T. Zuber, and E. M. Parmentier (2008), Mars' Paleomagnetic Field as the Result of a Single-Hemisphere Dynamo, *Science*, *321*, 1822–, doi: 10.1126/science.1161119.

Stevenson, D. J. (1980), Saturn's luminosity and magnetism, *Science*, *208*, 746–748, doi: 10.1126/science.208.4445.746.

Stevenson, D. J. (1982), Reducing the non-axisymmetry of a planetary dynamo and an application to Saturn, *Geophys. Astrophys. Fluid Dyn.*, *21*, 113–127, doi: 10.1080/03091928208209008.

Thébault, E., J. J. Schott, and M. Mandea (2006), Revised spherical cap harmonic analysis (R-SCHA): Validation and properties, *J. Geophys. Res.*, *111*, B01102, doi: 10.1029/2005JB003836.

Uno, H., B. J. Anderson, H. Korth, C. L. Johnson, and S. C. Solomon (2009), Modeling Mercury's internal magnetic field with smooth inversions, *Earth Planet. Sci. Lett.*, pp. 328–339, doi:10.1016/j.epsl.2009.02.032.

Verhoeven, O., P. Tarits, P. Vacher, A. Rivoldini, and T. van Hoolst (2009), Composition and formation of Mercury: Constraints from future electrical conductivity measurements, *Planet. Space Sci.*, *57*, 296–305, doi:10.1016/j.pss.2008.11.015.

von Frese, R. R. B., W. J. Hinze, and L. W. Braile (1981), Spherical earth gravity and magnetic anomaly analysis by equivalent point source inversion, *Earth Planet. Sci. Lett.*, *53*, 69–83, doi:10.1016/0012-821X(81)90027-3.

Whaler, K. A., and M. E. Purucker (2005), A spatially continuous magnetization model for Mars, *J. Geophys. Res.*, *110*, E09001, doi:10.1029/2004JE002393.

Wicht, J., and D. Heyner (2014), Mercury's magentic field in the messenger era, in *Planetary Geodesy and Remote Sensing*, edited by J. Shuanggen, pp. 223 – 262, CRC Press, doi: 10.1201/b17624-11.

Chapter 4

Hermean magnetic field models based on MESSENGER extended mission data

In this Chapter, the TD-ESD method is applied to data for nominal and extended MESSENGER mission. Different sidereal and solar day models are obtained, interpreted, and discussed.

4.1 Data availability and selection

MESSENGER data is available at the Planetary Plasma Interaction NASA site[1]. In this work, calibrated data are preferred over reduced magnetic data in order to avoid averages in the position and magnetic field. Mercury body fixed (MBF) and Mercury solar orbital (MSO) frames are used. The first frame is centered at the planet's center, where the x-axis points to the Hermean reference longitude, the z-axis is parallel to the rotation axis, and the y-axis completes the right-hand rule. The second frame is different from the first because the x-axis points toward Sun. Due to the 3:2 spin-orbit resonance of

[1] http://ppi.pds.nasa.gov/

Mercury, the planet completes three sidereal days in two Hermean years. In addition, one solar day is completed in three sidereal days (or in two Hermean years), contrary to the Earth where there is roughly no difference between the solar and sidereal days duration. During a complete sidereal day ($\sim$59 terrestrial days) MESSENGER covers all MBF longitudes. However, one Hermean year ($\sim$88 terrestrial days) is necessary to cover all MSO longitudes. In this Chapter, all maps are shown in the MBF frame unless specified.

Only measurements close to the planet, and inside the magnetosphere are selected. As in Chapter 3.2, we use the external field proxy which is sensitive to the frequency content of the magnetic field to select the field measurements. During the nominal MESSENGER mission, the spacecraft completed each orbit in 12 hours, passing two times inside the magnetosphere during one terrestrial day (orbit to orbit position spaced of 3° at equator). Later, after the orbit period reduction to 8 hours (at 20 April 2012 or doy=111), the spacecraft passed inside the magnetosphere three times in 24 hours (where orbit to orbit position is spaced of 2° at equator). Table 4.1 lists the eighteen Hermean sidereal days (or complete azimuthal coverages at MBF frame) MESSENGER measurements information.

The spacecraft altitude in MBF frame is shown in Figure 4.1 for all eighteen MESSENGER sidereal days. Each sidereal day is represented in two parts corresponding to the ascending and descending tracks. The ascending part contains all measurements for increasing latitudes, and the descending part the measurements for decreasing latitudes. Thus, certain latitudes are sampled twice in one sidereal day, usually with different altitudes and spaced in local time by about 12h. The spacecraft altitude of the selected measurements vary between 200 to 1000 km (note that one criterion of the proxy is to select measurements below 1000 km altitude). Drastic changes in altitude correspond to the beginning of the sidereal day (135°W) or to spacecraft maneuver altitude corrections (for other longitudes). Gaps on sidereal day measurements, such as for the second sidereal day (between longitudes 140°W and 200°W) or the sidereal day number 8 (between longitudes 1°E and 22°E), correspond to periods where data are not available. Other irregularities in the data coverage result from the external field proxy selection. Along all

Table 4.1: List of MESSENGER sidereal days characteristics: starting and end date (year and day-of-the-year, doy), number of orbits, latitudinal range, and spacecraft minimum altitude.

Sidereal day No.	Starting date year	doy	End date year	doy	No. orbits	MBF Lat. range (°) Min.	Max.	Min. altitude (km)
1	2011	83	2011	142	115	-1.0	83.1	216.6
2	2011	142	2011	200	100	0.7	83.4	200.4
3	2011	200	2011	258	118	3.6	83.6	200.1
4	2011	259	2011	317	119	4.5	83.6	211.3
5	2011	317	2012	10	118	7.1	83.8	200.1
6	2012	11	2012	69	120	10.7	83.9	200.0
7	2012	70	2012	128	137	11.4	84.0	210.3
8	2012	128	2012	186	165	14.6	84.0	291.5
9	2012	187	2012	245	175	20.4	84.0	355.2
10	2012	245	2012	304	176	24.9	84.1	397.0
11	2012	304	2012	362	176	28.2	84.1	421.0
12	2012	363	2013	55	173	32.2	84.1	440.6
13	2013	55	2013	113	174	35.4	84.1	446.9
14	2013	114	2013	173	177	32.4	84.1	429.0
15	2013	173	2013	231	176	29.3	84.1	414.0
16	2013	232	2013	290	176	25.6	84.1	383.7
17	2013	290	2013	348	176	19.7	84.0	317.8
18	2013	349	2014	42	176	15.5	84.0	277.0

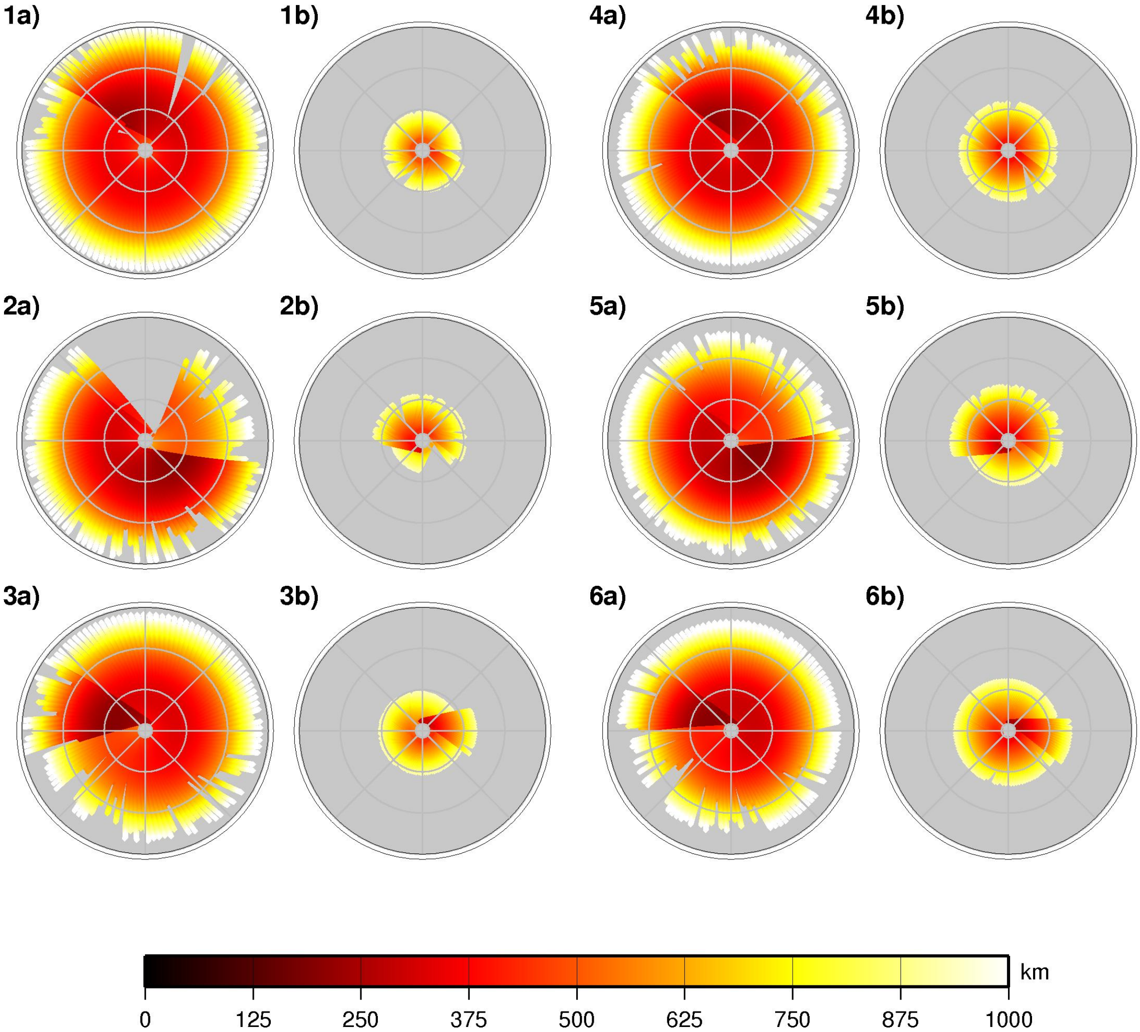

Figure 4.1: Spacecraft altitude for the first eighteen MESSENGER Hermean sidereal days in MBF frame. The numbers denote the sidereal day, and a) and b) denote the descending and ascending nodes, respectively. The 0° MBF longitude is toward bottom. The plots show only the northern hemisphere of the planet. The grid lines are at 30°N, 60°N, and at 45° longitude intervals.

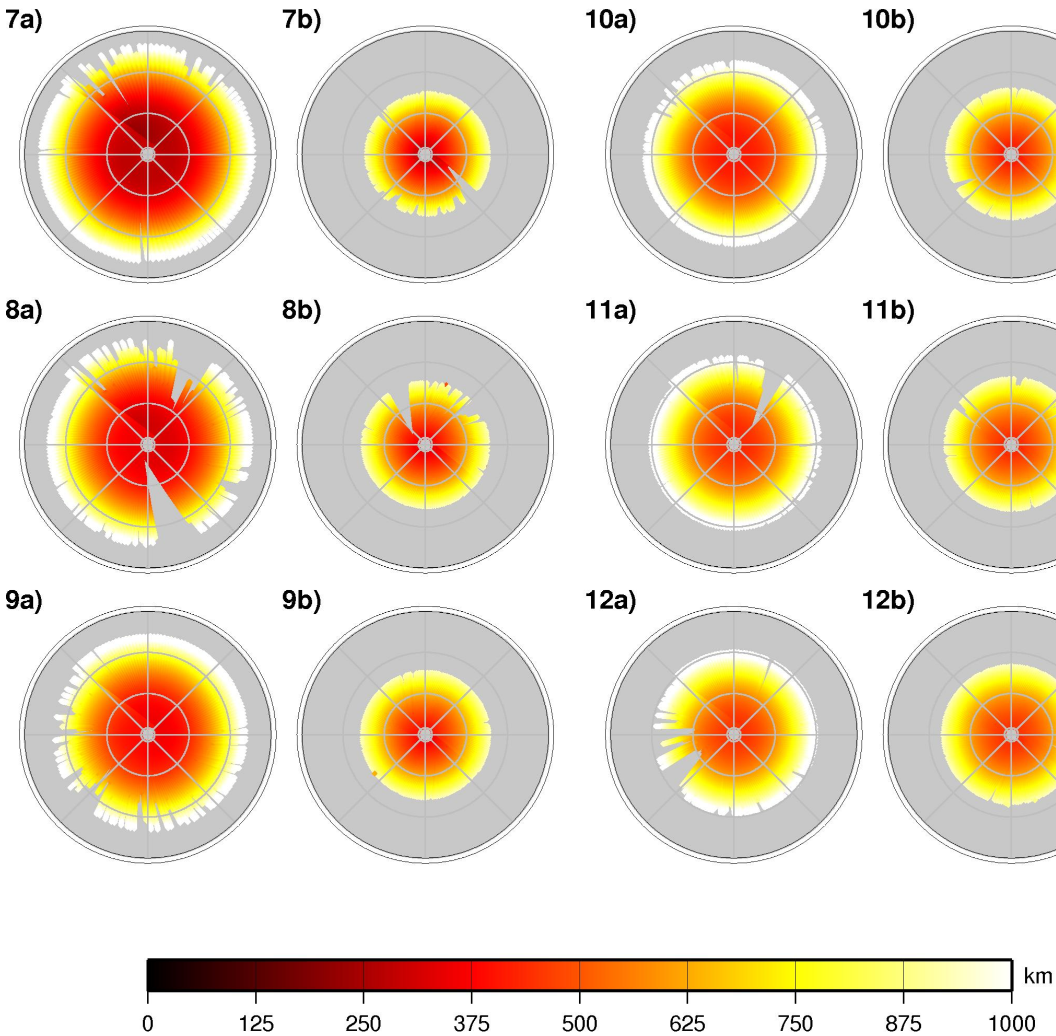

Figure 4.1: (cont.)

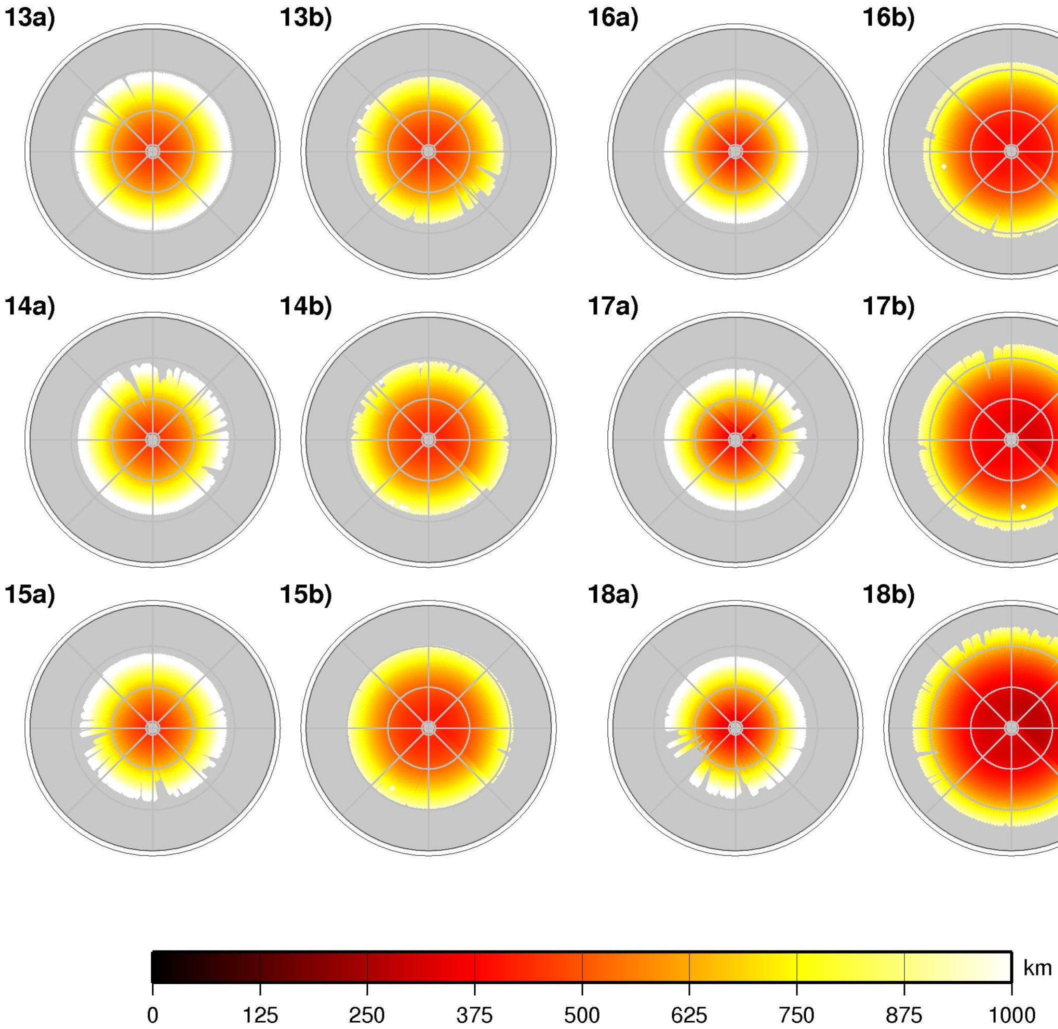

Figure 4.1: (cont.)

sidereal days, the distribution of descending/ascending tracks varies. For sidereal days numbers 1 to 11 the descending node contains a better latitudinal coverage, contrary to sidereal days numbers 16 to 18. Sidereal days numbers 12 to 15 have similar latitudinal coverages for both descending and ascending parts. For sidereal days 7 to 12, the spacecraft periapsis altitude increases (compare to Figure 1.11 for the period between MOI+1 and MOI+2). For the last sidereal days 13 to 18, the periapsis altitude decreases.

The magnetic field spherical components measured by MESSENGER are shown in Figure 4.2, for all data set listed in Table 4.1. In general, all sidereal days show: a very negative region around the North Pole for the B_r component (even stronger for lower altitudes); a positive small region near the pole and negative elsewhere for the B_θ component; and a weak B_ϕ component. Abrupt spatial changes in field intensity usually correspond to changes in spacecraft altitude. When measurements for latitudes south of 30°N are available, the B_r component is very weak. The weak B_ϕ component shows a positive/negative structure that move around the planetary rotation axis and repeats its location every three sidereal days. It is interesting to note that for a very active external magnetic field environment as in the case of Mercury, orbit to orbit measured field does not change drastically.

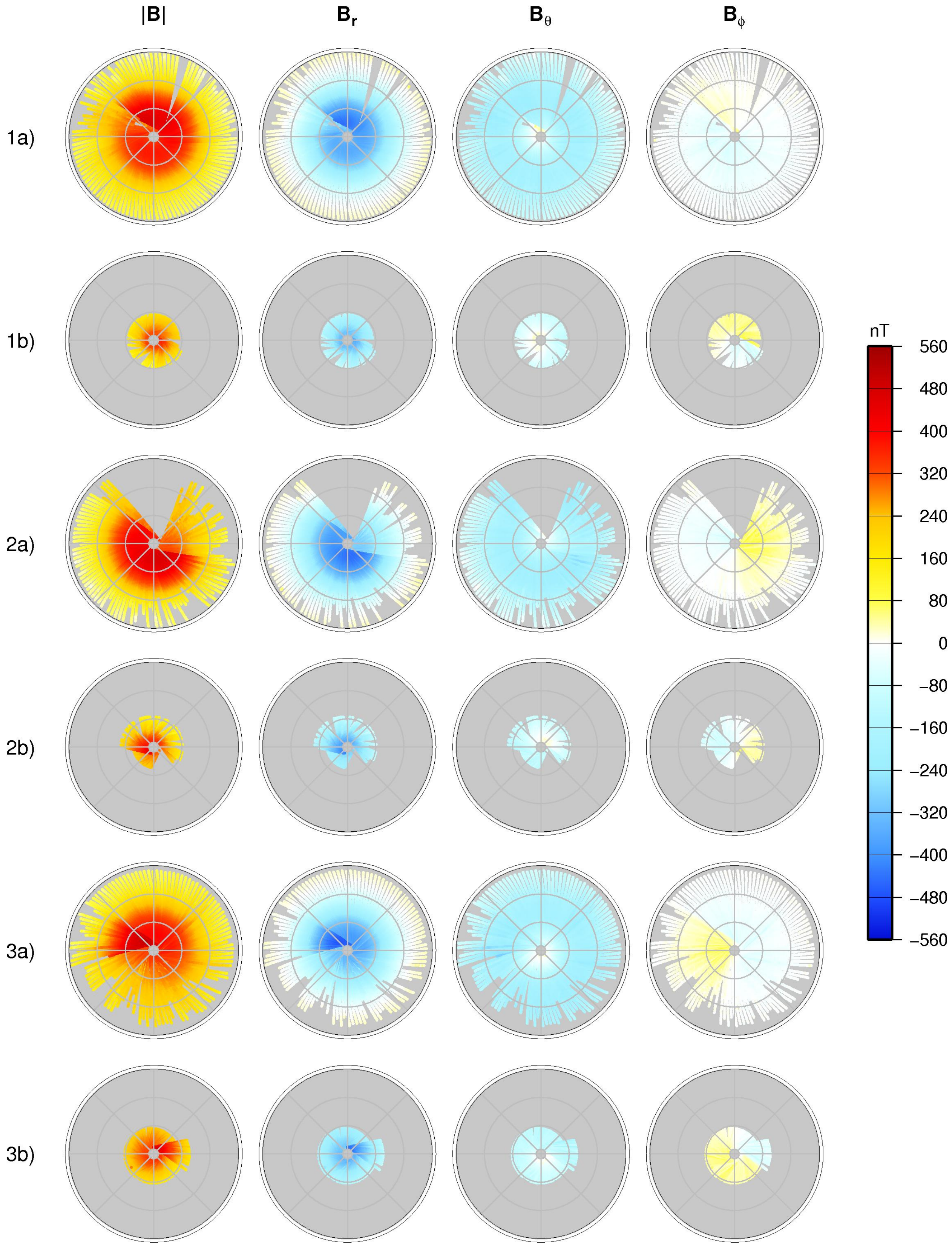

Figure 4.2: Magnetic field measurements in MBF coordinates above the northern hemisphere of Mercury at spacecraft altitude for the eighteen sidereal days. Numbers denote the sidereal day, and a) and b) denote the descending and ascending nodes, respectively. The 0° MBF longitude is toward bottom.

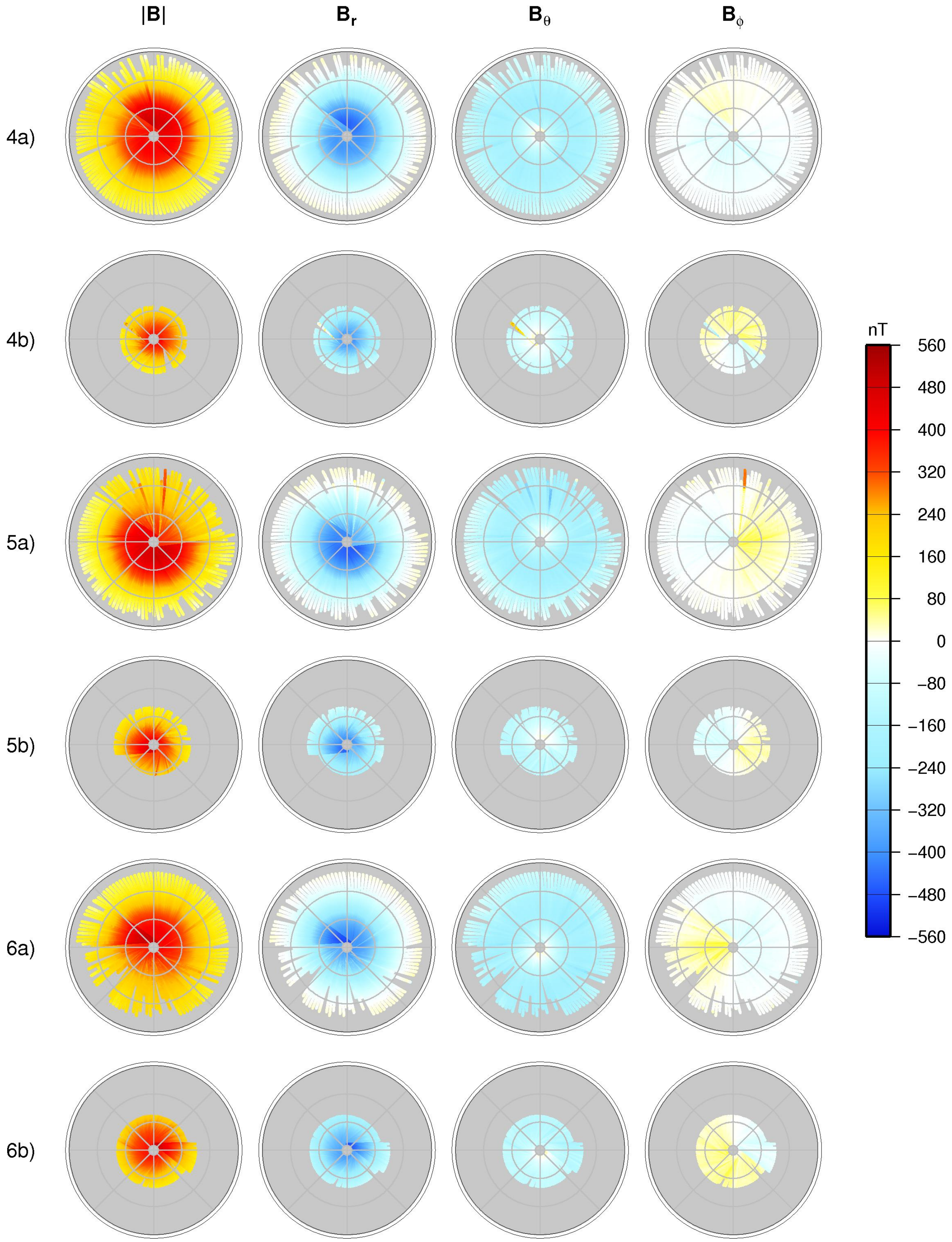

Figure 4.2: (cont.)

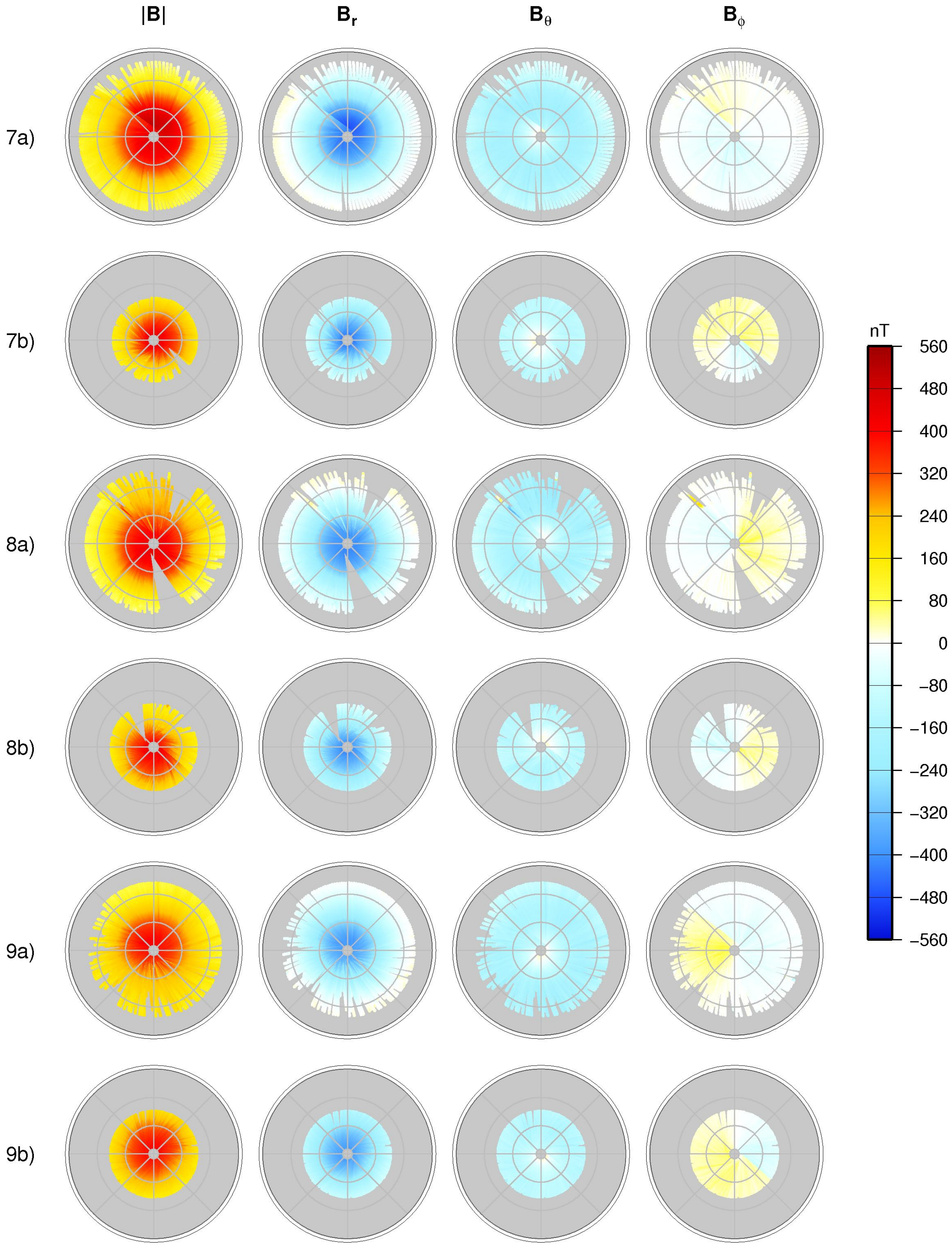

Figure 4.2: (cont.)

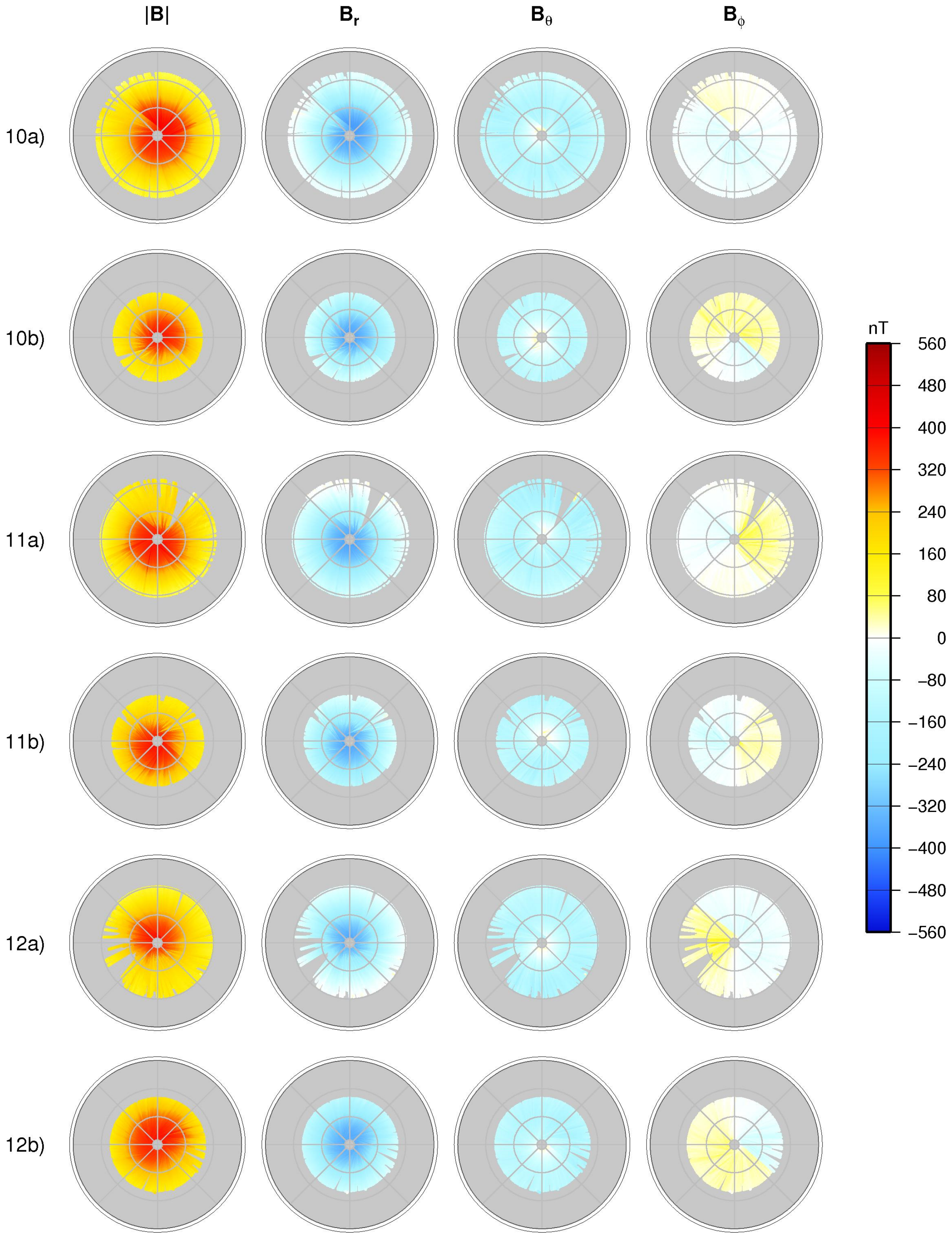

Figure 4.2: (cont.)

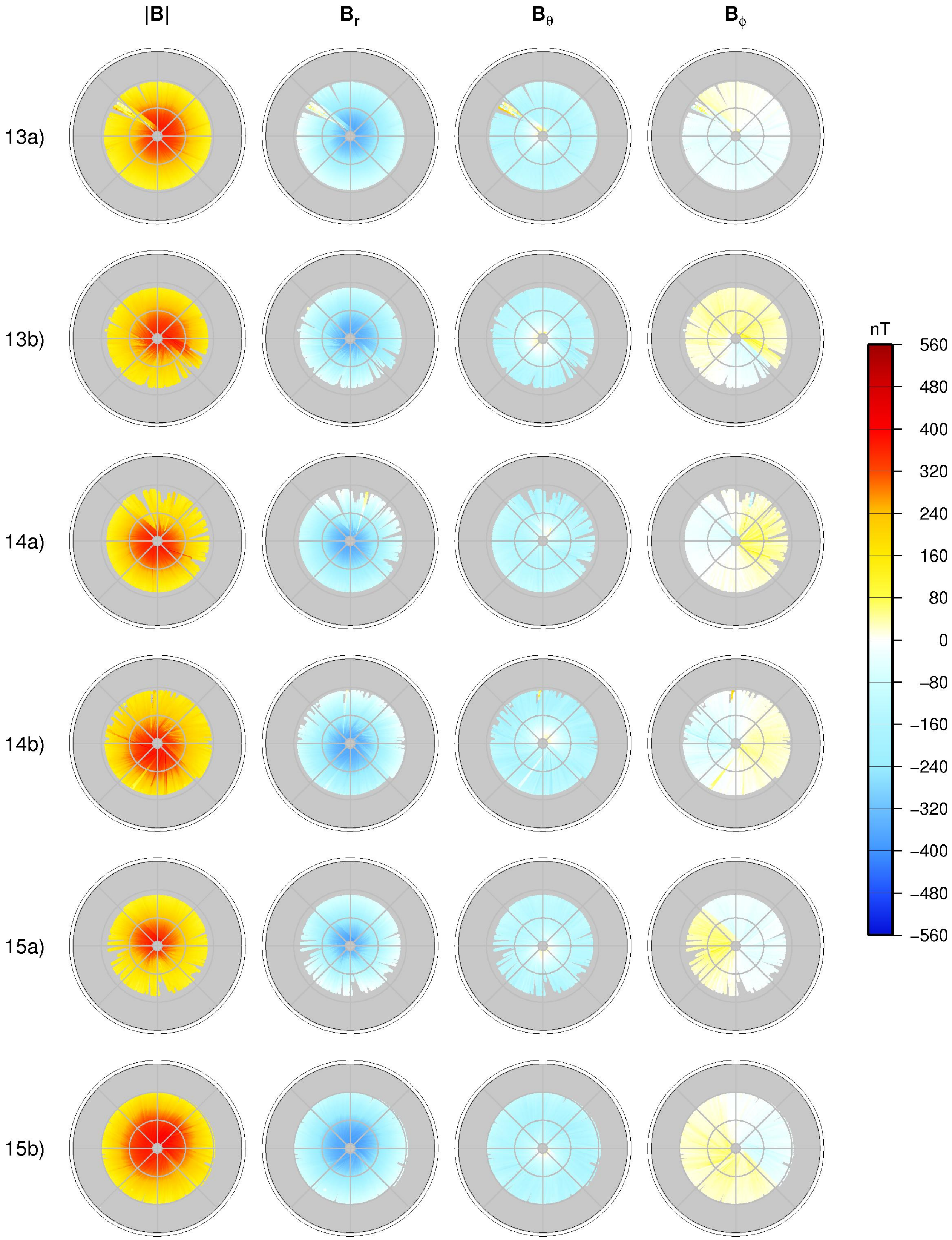

Figure 4.2: (cont.)

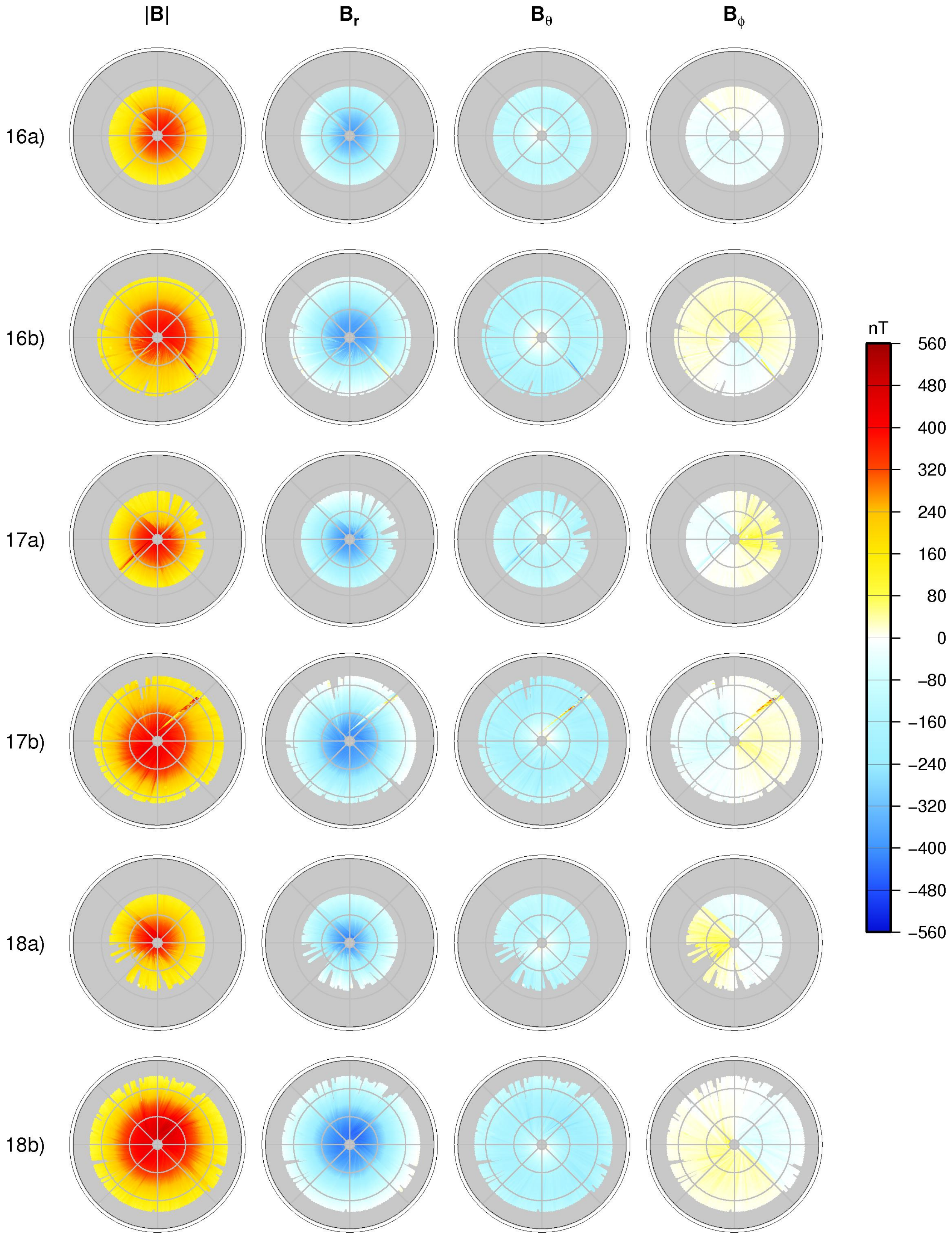

Figure 4.2: (cont.)

4.2 Sidereal-day models from TD-ESD

The TD-ESD method is applied to each eighteen MESSENGER sidereal day. The scheme described in Section 3.2 of the Draft Manuscript is used to choose the optimal solution. The field is considered reliable from the North Pole to a latitude threshold, depending on the measurements position. This latitude threshold is estimated based on the truncation tests with a synthetic field distributed over the first sidereal day spacecraft position (Fig. A8). From the σ_{B_r} derivative a variation of more than 5% is arbitrarily chosen to define the limit where our model predicts correctly the magnetic field. Thus this corresponds to a latitude threshold of 5°N. A difference between the minimum latitude and the threshold latitude of 6° is applied to all TD-ESD models, in order to compute the corresponding threshold latitudes (shown in Table 4.2), as a first approach. A more accurate method to compute the threshold latitude, such as modeling a synthetic field distributed over each sidereal day, probably would not differ much from this approximation. As highlighted in Chapter 3.2, small-scales that vary in time are interpreted to be of external origin. The Hermean secular variation is thought to be much slower than the temporal variation of those small-scales, thus the time-dependence is not solved here. Maps of the Hermean magnetic field intensity and its spherical components are plotted to all MESSENGER sidereal days, at 200 km altitude (Figures 4.3, 4.5, 4.7, 4.9, 4.11 and 4.13).

For all sidereal day models, the maximum absolute radial field $|B_r|$ is located at the north pole region, and the average position of the magnetic equator ($B_r = 0$) if visible is in the northern hemisphere. The B_θ component is essentially negative over the northern hemisphere. The B_ϕ component is significantly weaker than the other components. The magnetic equator $B_r = 0$ position varies from one sidereal day to another.

Small-scale features move around the planetary rotation axis, for all components. For example the very intense and positive radial field structure near the equator is located between 90°W - 135°W at sidereal day 1 model, moves to longitudes 135°W - 270°W for the sidereal day 2, and finally it is seen at longitudes 90°E - 90°W for sidereal day 3. This is also observed for the B_θ component with the very negative small-scale feature. The B_ϕ component also shows small-scale rotating features, but less clearly. The position of these small-scale structures repeats every 3 sidereal days, for which the solar conditions are similar due to the 3:2 spin-orbit resonance. These small-scale structures are thought to be signatures of the external field in the sidereal day models. Although these small-scale structures are non-zonal, the field is nevertheless dominantly axisymmetric.

The corresponding residuals at spacecraft altitude for the descending and ascending tracks are shown in Figures 4.4, 4.6, 4.8, 4.10, 4.12 and 4.14. Orbit to orbit intensity changes are observed over all sidereal days, for all components. This is expected, because of the temporal variability of the magnetospheric field. As for the sidereal day models, small-scales are seen rotating around the planetary rotation axis, repeating each three sidereal days, and similar features are observed for identical solar conditions, for all three components. The residuals of the B_ϕ component (component least modeled in our resulting dominantly axisymmetric field) is comparable in strength to the other residual components, indicating that B_ϕ is probably dominated by an external field.

Statistics for the sidereal day models are shown in Table 4.2. The most evident characteristic that should be highlighted here is the larger relative misfit and the poor correlation coefficient of the B_ϕ component in agreement with an axisymmetric field.

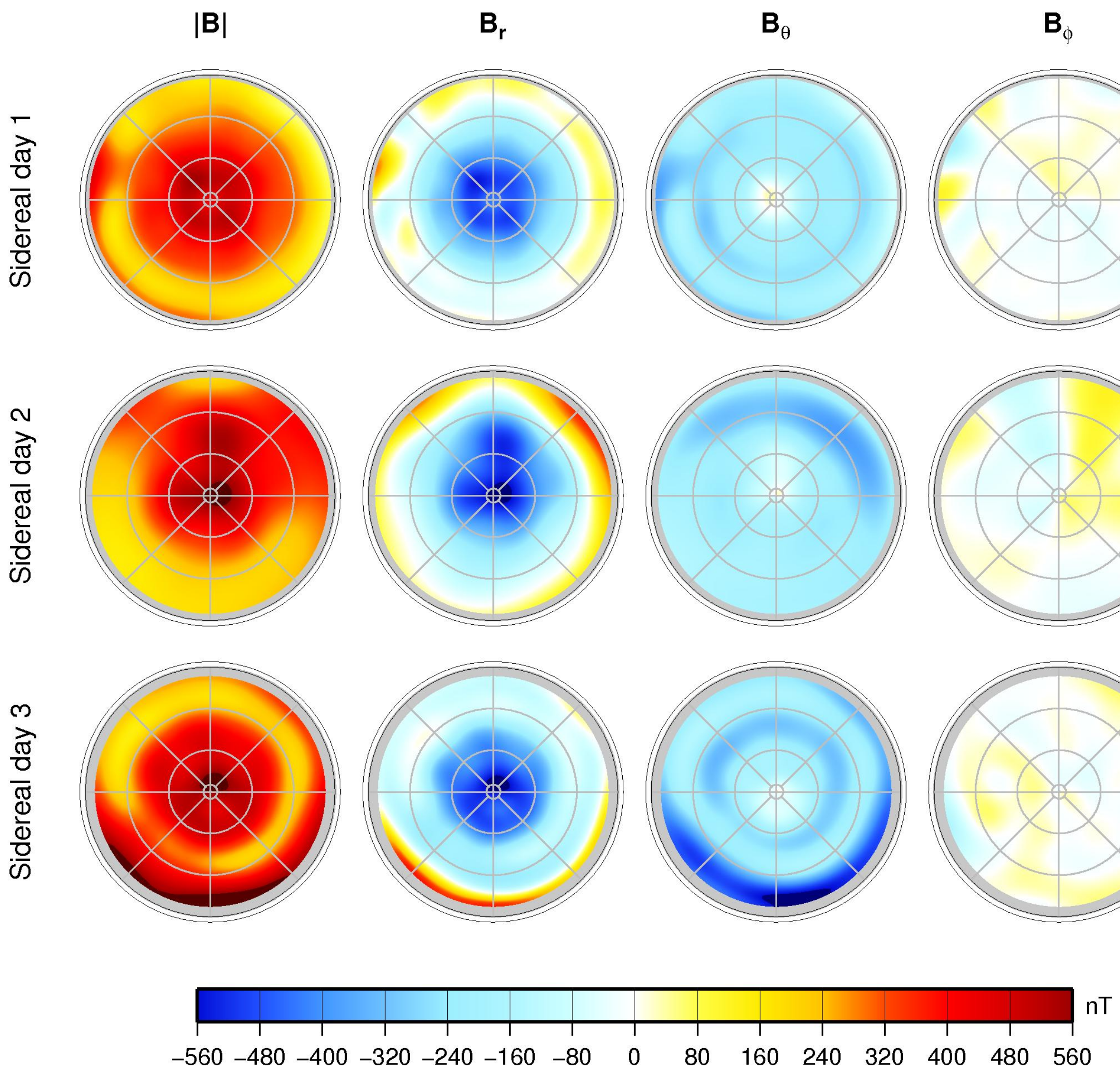

Figure 4.3: TD-ESD modeled magnetic field maps above the northern hemisphere of Mercury at 200 km altitude in MBF coordinates for the mean epochs of each MESSENGER sidereal day. The magnetic field unit is nT. Grid lines (grey) are drawn every $45°$ for longitude and every $30°$ for latitude. The maps are shown in stereographic projection. The $0°$ MBF longitude is toward bottom.

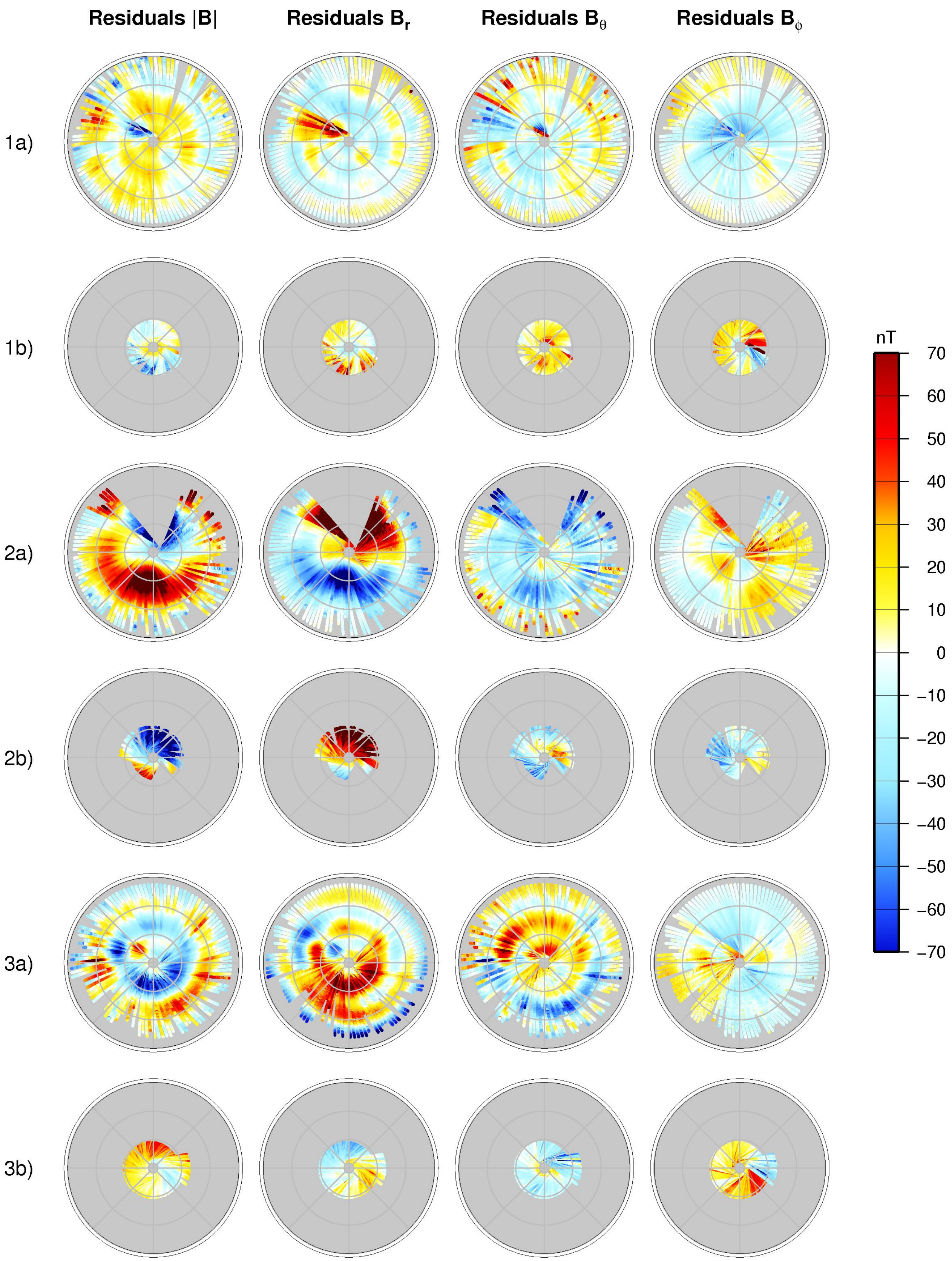

Figure 4.4: Magnetic field residual maps above the northern hemisphere of Mercury at 200 km altitude in MBF coordinates for the mean epochs of each MESSENGER sidereal day. a) and b) denote the descending and ascending nodes, respectively. The 0° MBF longitude is toward bottom.

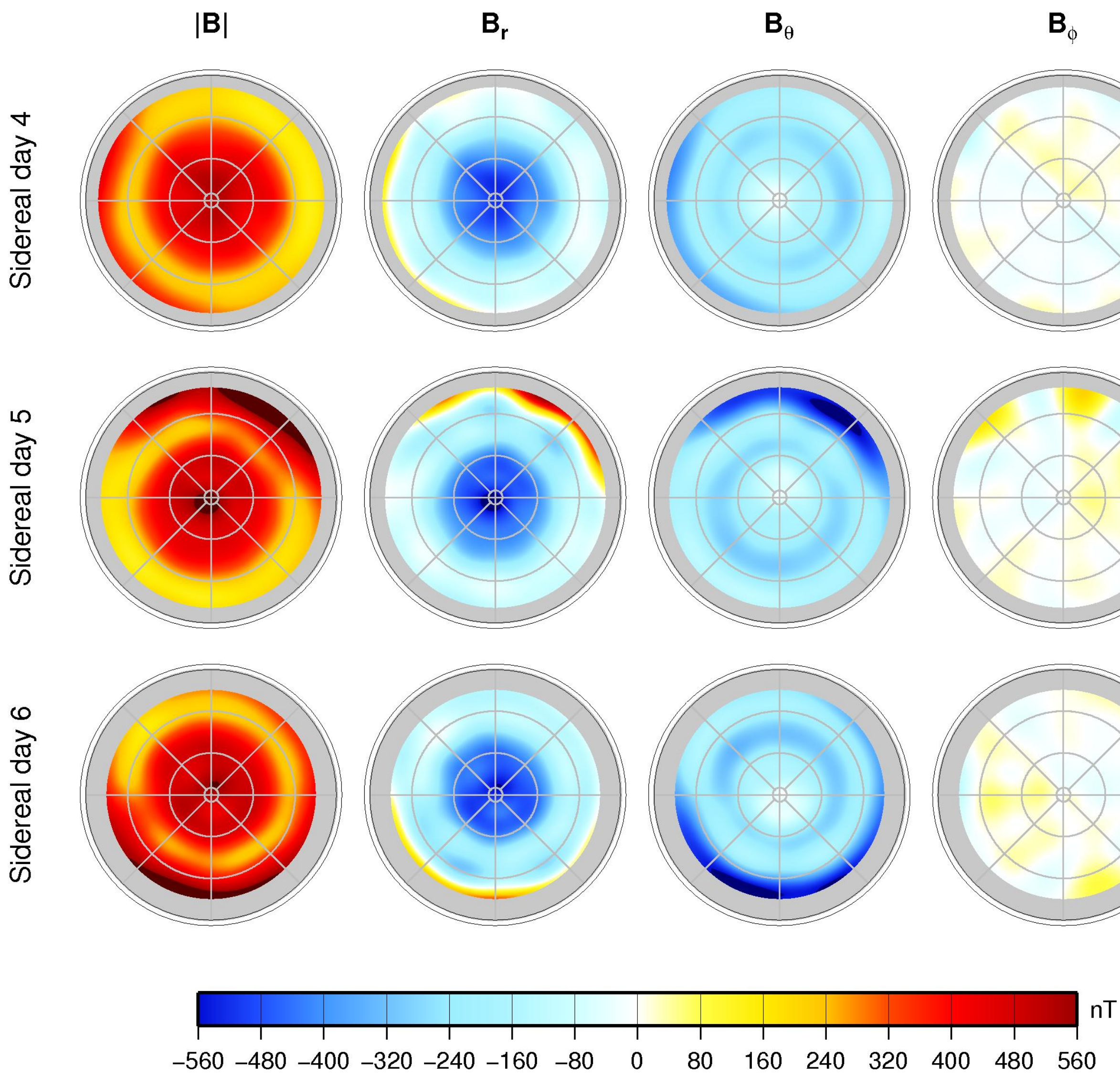

Figure 4.5: As in Figure 4.3.

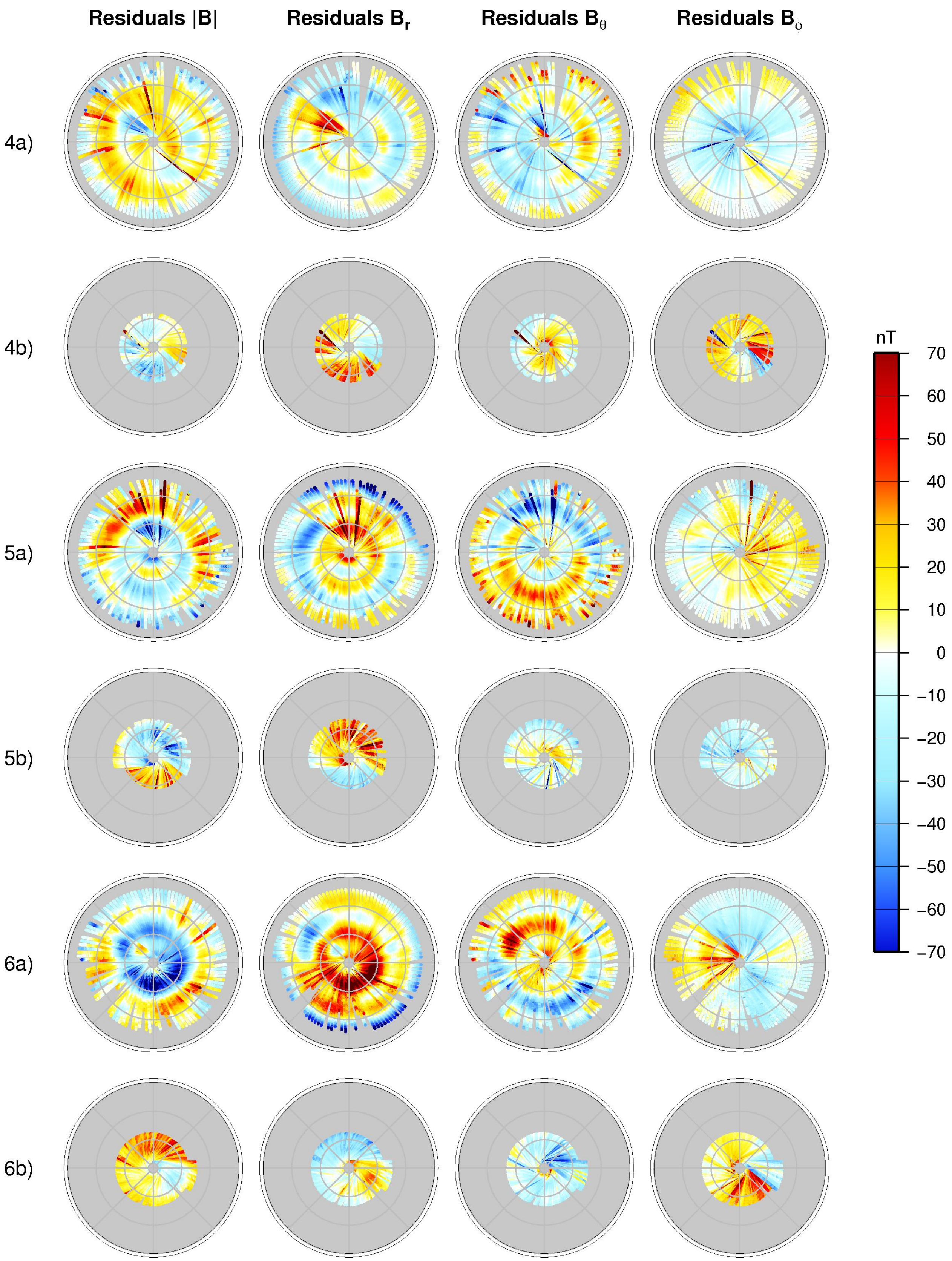

Figure 4.6: As in Figure 4.4.

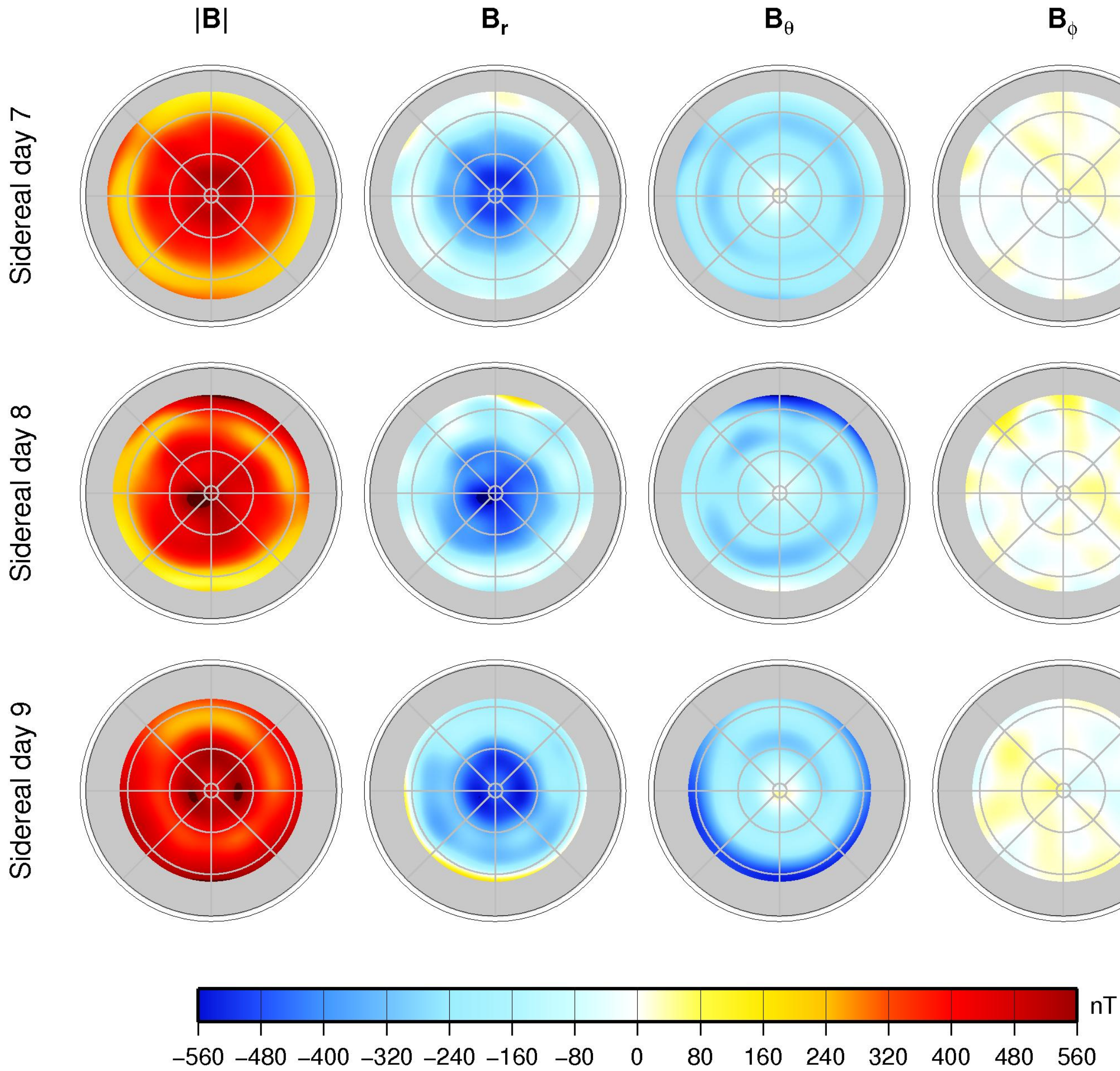

Figure 4.7: As in Figure 4.3.

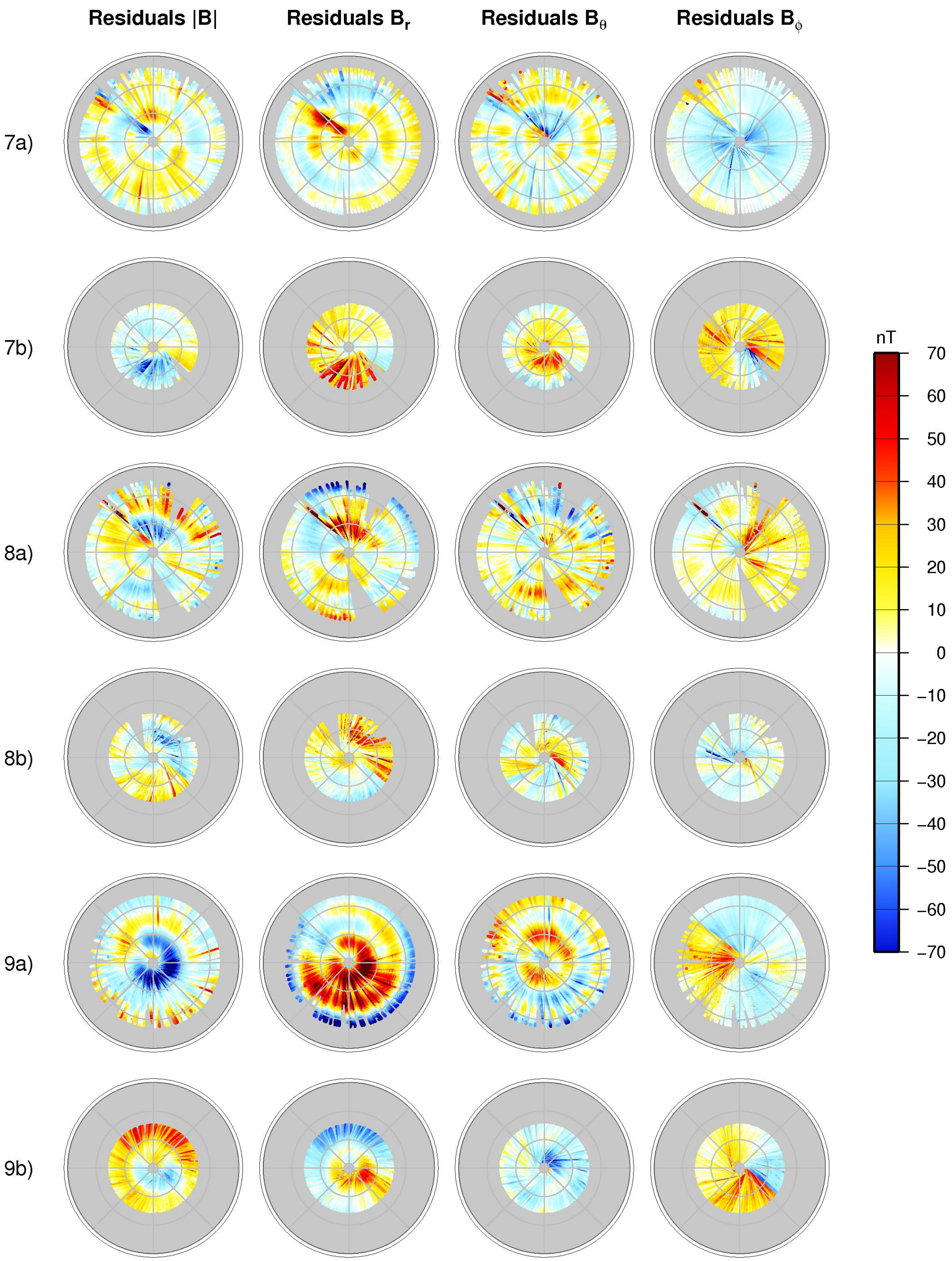

Figure 4.8: As in Figure 4.4.

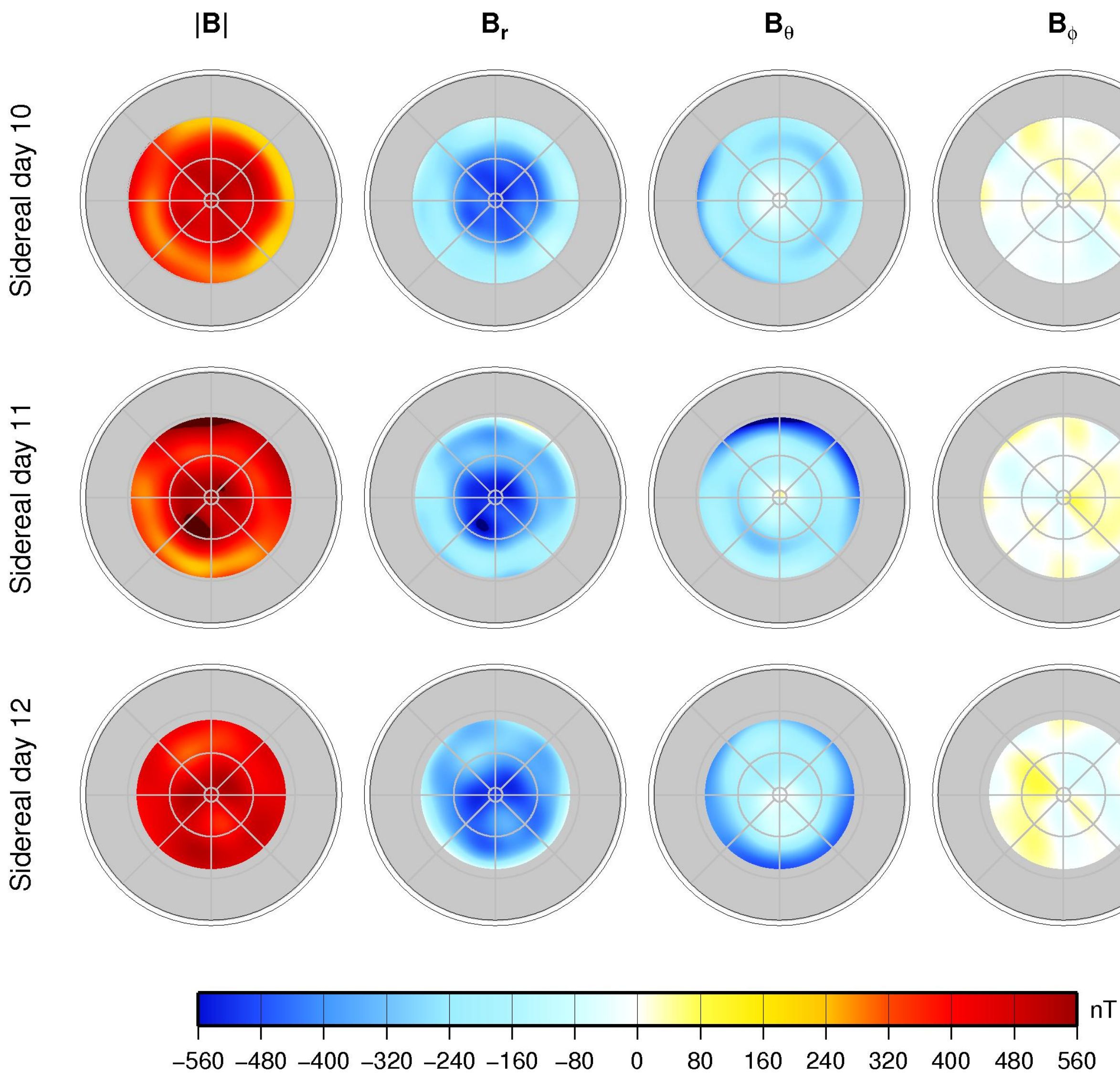

Figure 4.9: As in Figure 4.3.

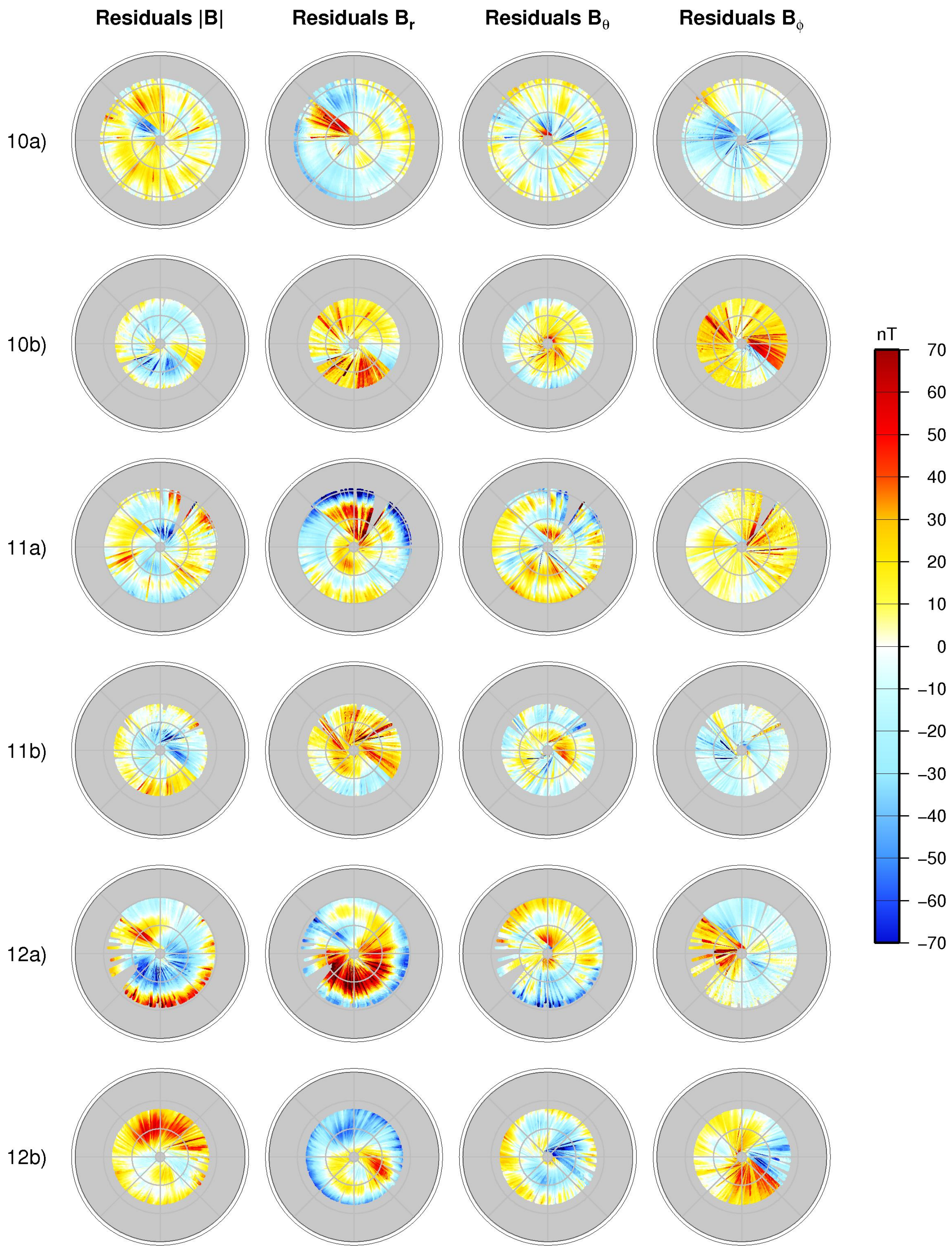

Figure 4.10: As in Figure 4.4.

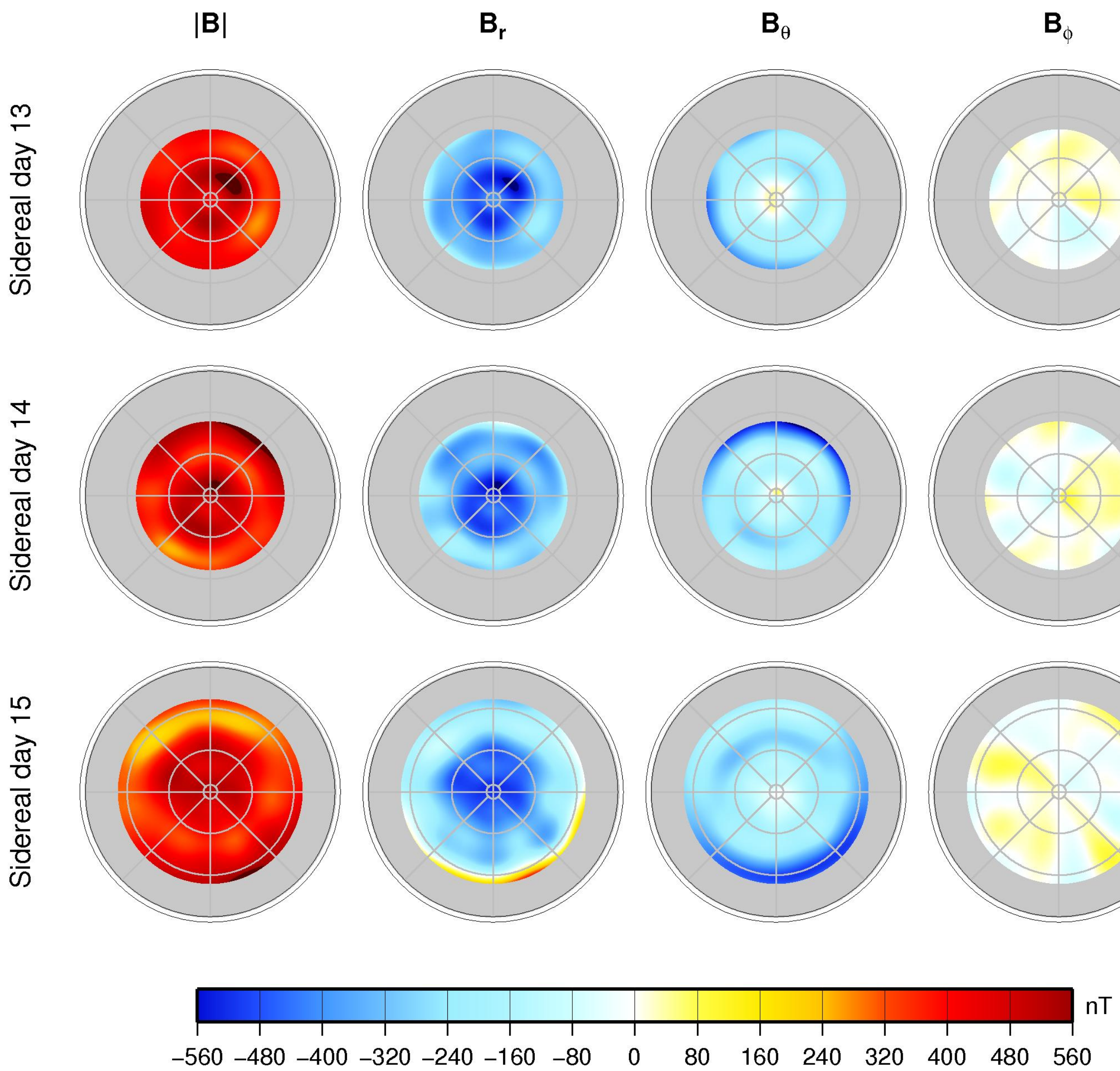

Figure 4.11: As in Figure 4.3.

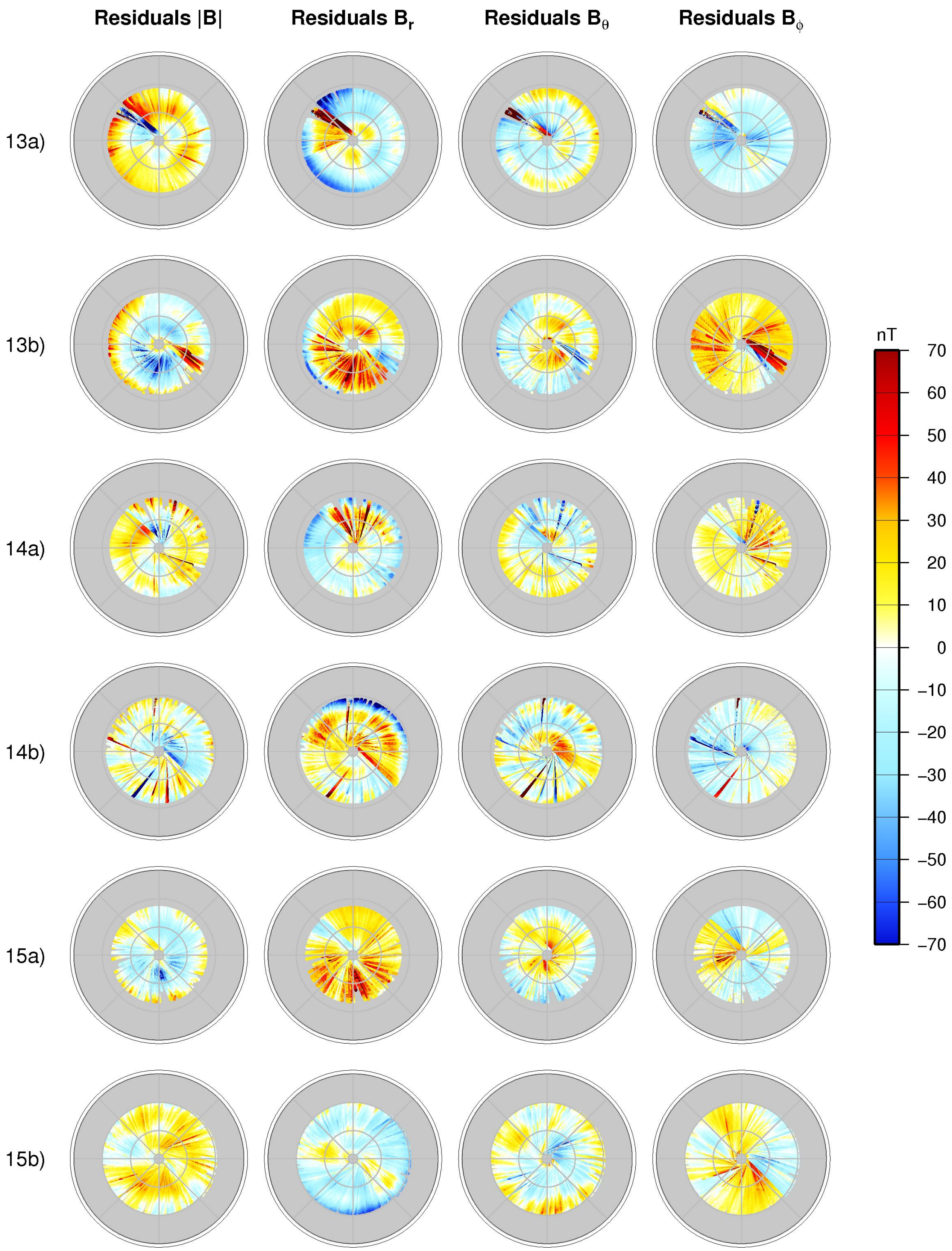

Figure 4.12: As in Figure 4.4.

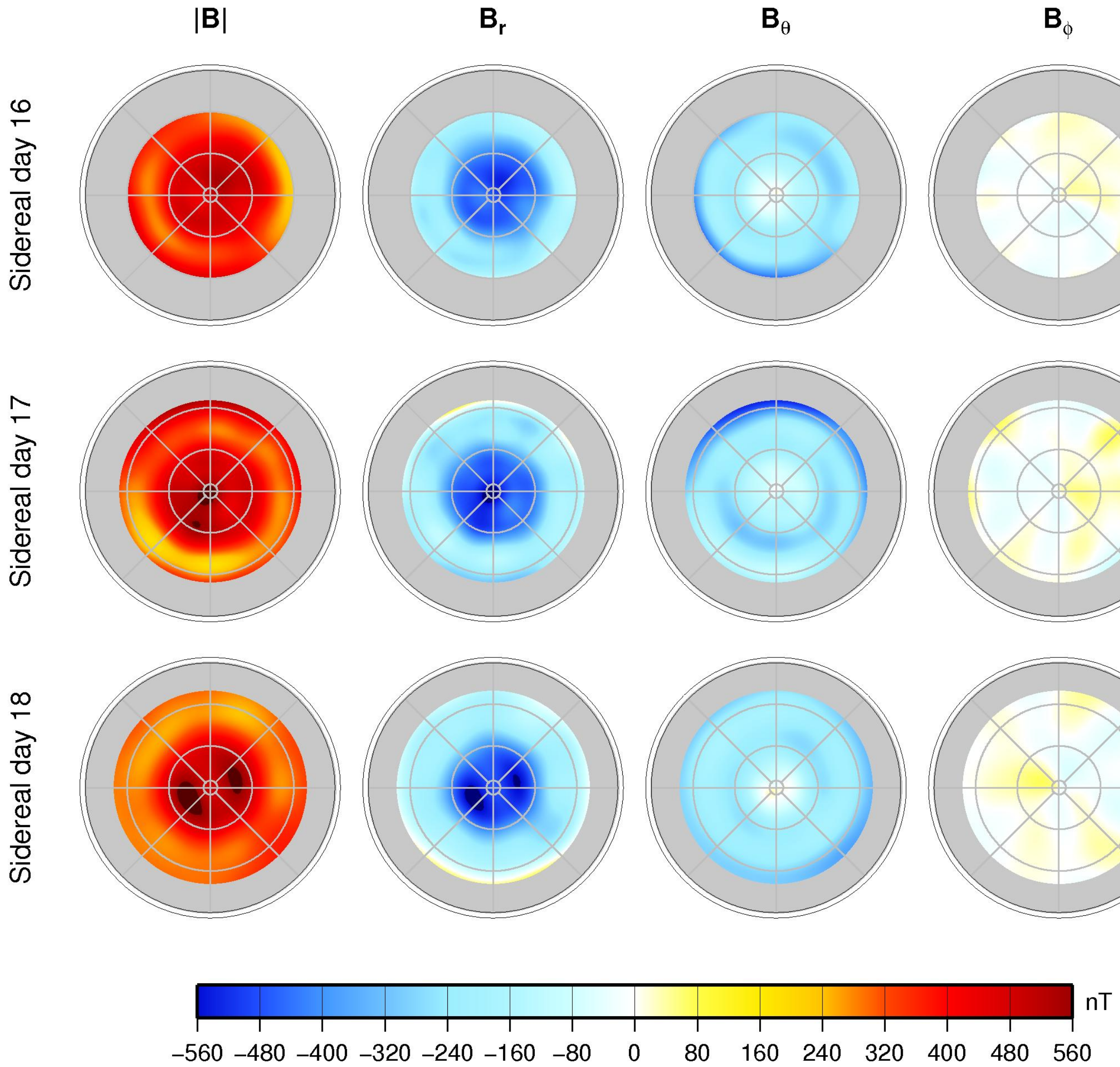

Figure 4.13: As in Figure 4.3.

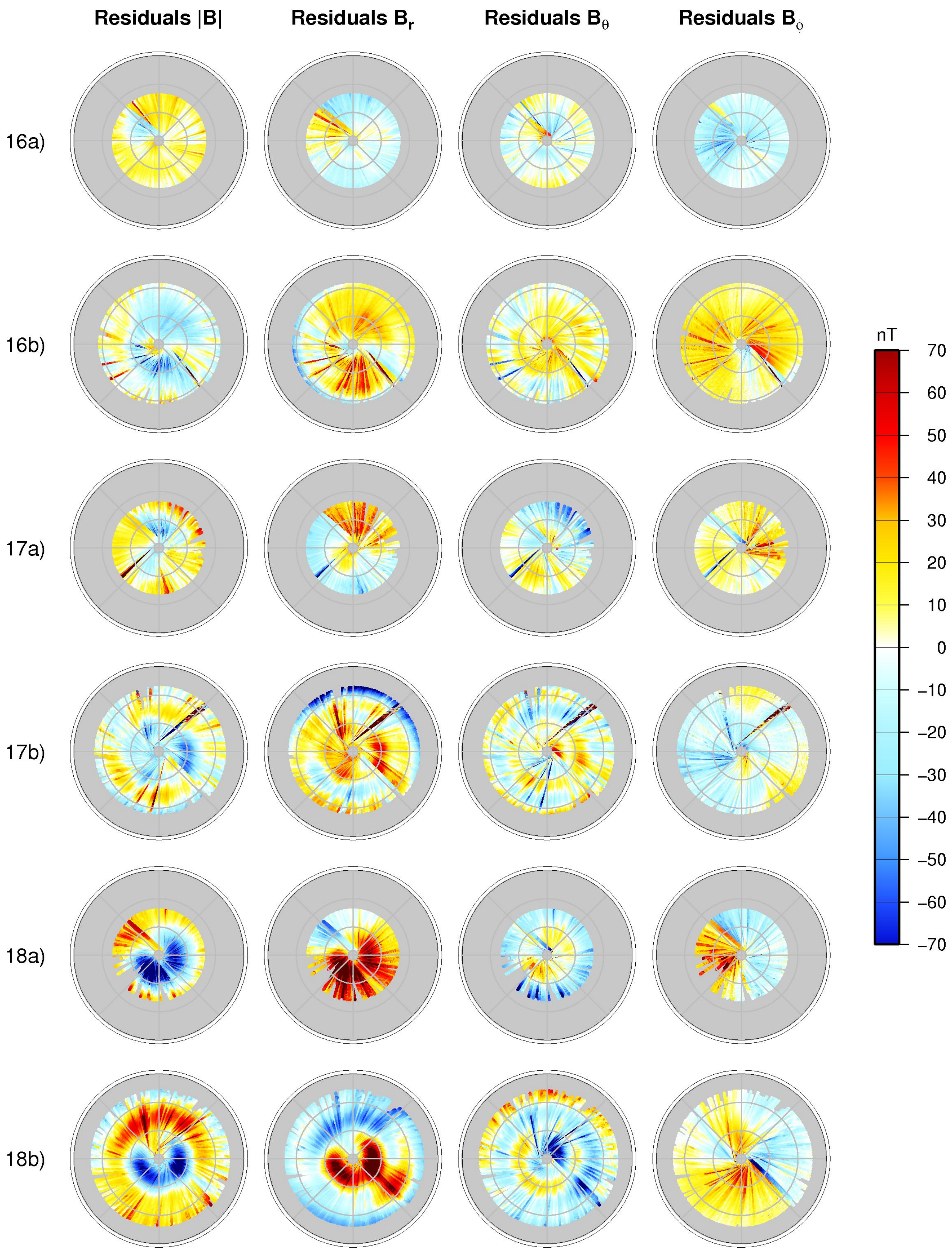

Figure 4.14: As in Figure 4.4.

4.3 Solar day TD-ESD models

During one solar day, all local times are sampled. In order to compare models with the same external field conditions (in which the Sun plays an important role), the TD-ESD method is applied to periods of a solar day (3 consecutive sidereal days). The measurements used here are sampled each 5 seconds (or 0.2 Hz) and not each 2 seconds (0.5 Hz) as before, because the number of measurements increased. As for the sidereal days case, the scheme described in Section 3.2 of the Draft Manuscript is used to choose the optimal solution. Figure 4.15 shows the trade-off curves for each solar day. The threshold latitude of the solar day models is computed as for the sidereal days (shown in Table 4.3). Again, no SV is modeled here because the temporal variations of the field are too fast to be of core dynamo origin.

The solar day model maps are shown in Figure 4.16, and the corresponding statistics are shown in Table 4.3. For the solar day models, the field is even more axisymmetric than the sidereal day models. The B_ϕ component is very small and it is not correlated with the measured field. The relative misfit for the radial component is smaller than 15%, and there is little evidence of small-scales in the radial and latitudinal components. Two main features vary between one solar day model to another, in terms of their latitudinal localization: the magnetic equator (B_r = 0) and the negative low-latitudes ring in the B_θ component.

The axisymmetric field found in the solar day models motivates examination of zonal field profiles (Fig. 4.17). As expected from the maps in Figure 4.16, the time varying solar day models result in different zonal profiles for B_r and B_θ. The magnetic equator (B_r =0) position varies between 9°N and 12°N of latitude. These values are from the solar day models 1 and 2, corresponding to the models with better latitudinal coverage. The intense negative ring in B_θ also changes its position. These position variation could be due to a strong external field component that vary with time.

For the zonal radial profile, the solar day 4 and 5 models are similar for latitudes north

Table 4.2: Number of observations retained for inversion, rms of the observed field, iteration chosen, relative misfit and correlation coefficients between the observed field and the model. The observed field rms, the inversion misfit and the correlation coefficient are given for the magnetic field vector and its spherical components B_r, B_θ and B_ϕ.

Sidereal	No.	Lat.	Observed field rms (nT)				Iteration	σ_B (nT)				Corr. Coeff.			
day	of Obs.	Threshold	**B**	B_r	B_θ	B_ϕ		**B**	B_r	B_θ	B_ϕ	**B**	B_r	B_θ	B_ϕ
1	86134	5	275.3	238.9	133.4	28.7	23	31.8	16.4	18.0	20.5	0.98	0.99	0.96	0.71
2	68971	6	291.2	252.1	141.3	35.7	7	57.6	46.4	27.5	20.2	0.94	0.95	0.94	0.83
3	89947	9	281.2	242.0	139.6	32.2	14	42.2	27.9	24.2	20.4	0.96	0.98	0.93	0.78
4	88649	10	292.5	258.7	132.7	31.8	14	41.0	22.4	24.7	23.8	0.97	0.99	0.92	0.65
5	90700	12	299.8	263.2	138.9	35.9	14	42.5	29.4	22.8	20.6	0.97	0.98	0.92	0.84
6	94598	16	294.9	258.7	137.2	34.8	16	44.7	30.2	23.9	22.7	0.96	0.98	0.91	0.78
7	114369	16	304.1	272.2	132.0	31.5	27	35.3	18.1	19.5	23.2	0.98	0.99	0.94	0.71
8	130703	20	298.6	265.5	132.3	34.2	22	36.7	23.0	20.8	19.6	0.97	0.99	0.92	0.84
9	141620	25	285.7	253.4	126.9	36.1	11	46.2	33.9	22.2	22.2	0.95	0.97	0.90	0.82
10	141494	30	273.8	246.9	113.3	33.8	19	37.2	20.0	19.1	24.9	0.95	0.98	0.92	0.68
11	137118	33	275.0	245.3	118.9	36.1	15	36.6	24.8	19.7	18.3	0.96	0.98	0.89	0.87
12	136307	37	271.3	242.8	115.1	37.7	10	44.8	30.2	23.0	23.8	0.93	0.96	0.87	0.80
13	137413	40	265.8	239.6	109.5	35.6	12	47.3	29.7	24.4	27.4	0.91	0.96	0.87	0.64
14	136470	37	276.2	245.2	120.5	40.1	17	38.1	22.2	22.8	20.9	0.95	0.98	0.87	0.86
15	139192	24	275.5	247.7	115.4	35.3	19	33.5	19.6	18.5	20.0	0.96	0.98	0.92	0.84
16	149363	31	276.3	248.8	116.4	29.6	21	35.9	20.8	18.6	22.7	0.96	0.98	0.92	0.64
17	146637	25	293.6	259.7	131.7	38.0	14	47.9	30.9	26.7	24.9	0.94	0.98	0.85	0.78
18	139883	21	276.3	248.8	116.4	29.6	9	53.2	39.6	26.5	23.6	0.95	0.97	0.89	0.75

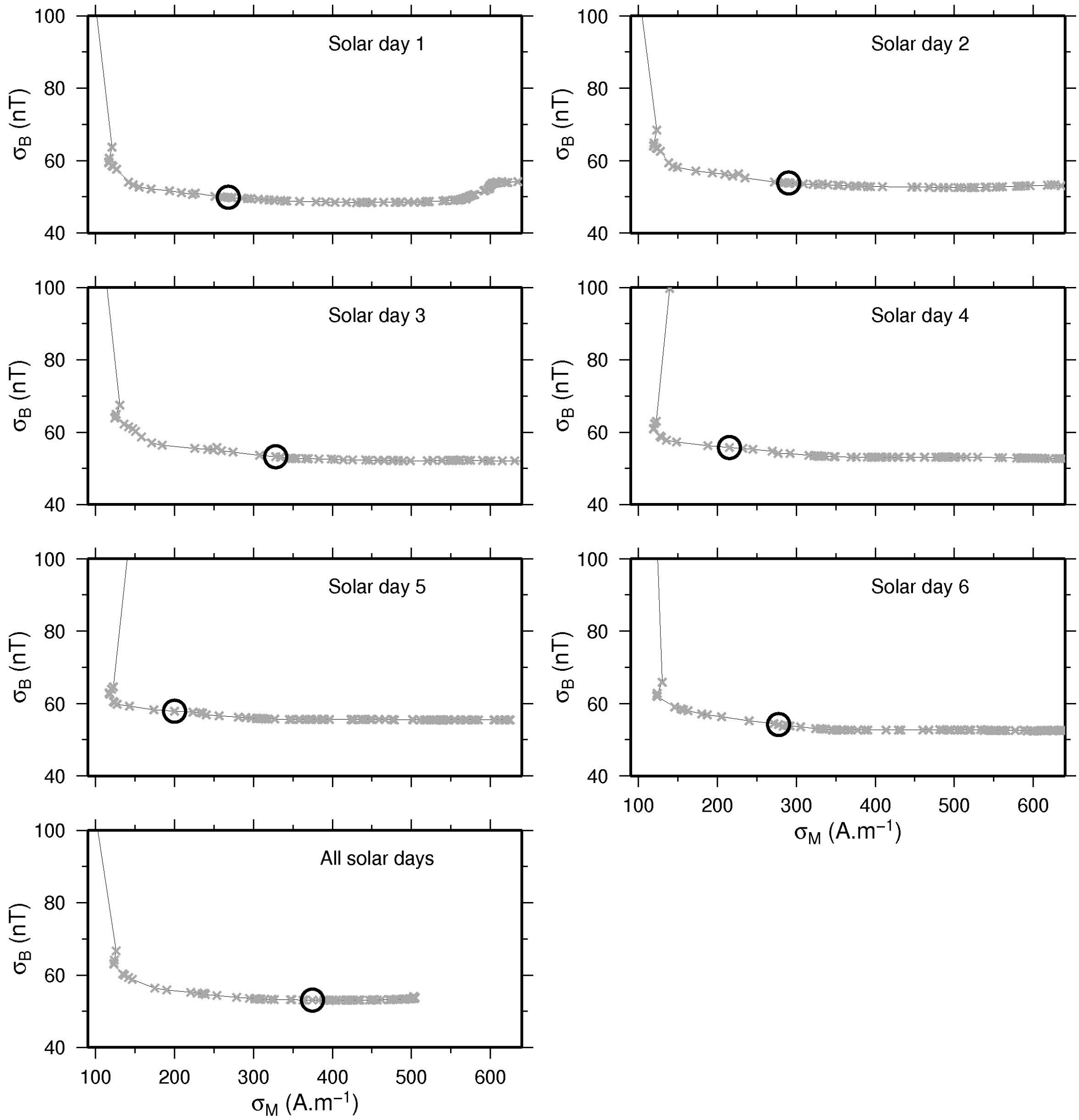

Figure 4.15: Trade-off curves for all solar days (grey) with the chosen model highlighted by the black circles. The trade-off curve for all solar days together, is also shown.

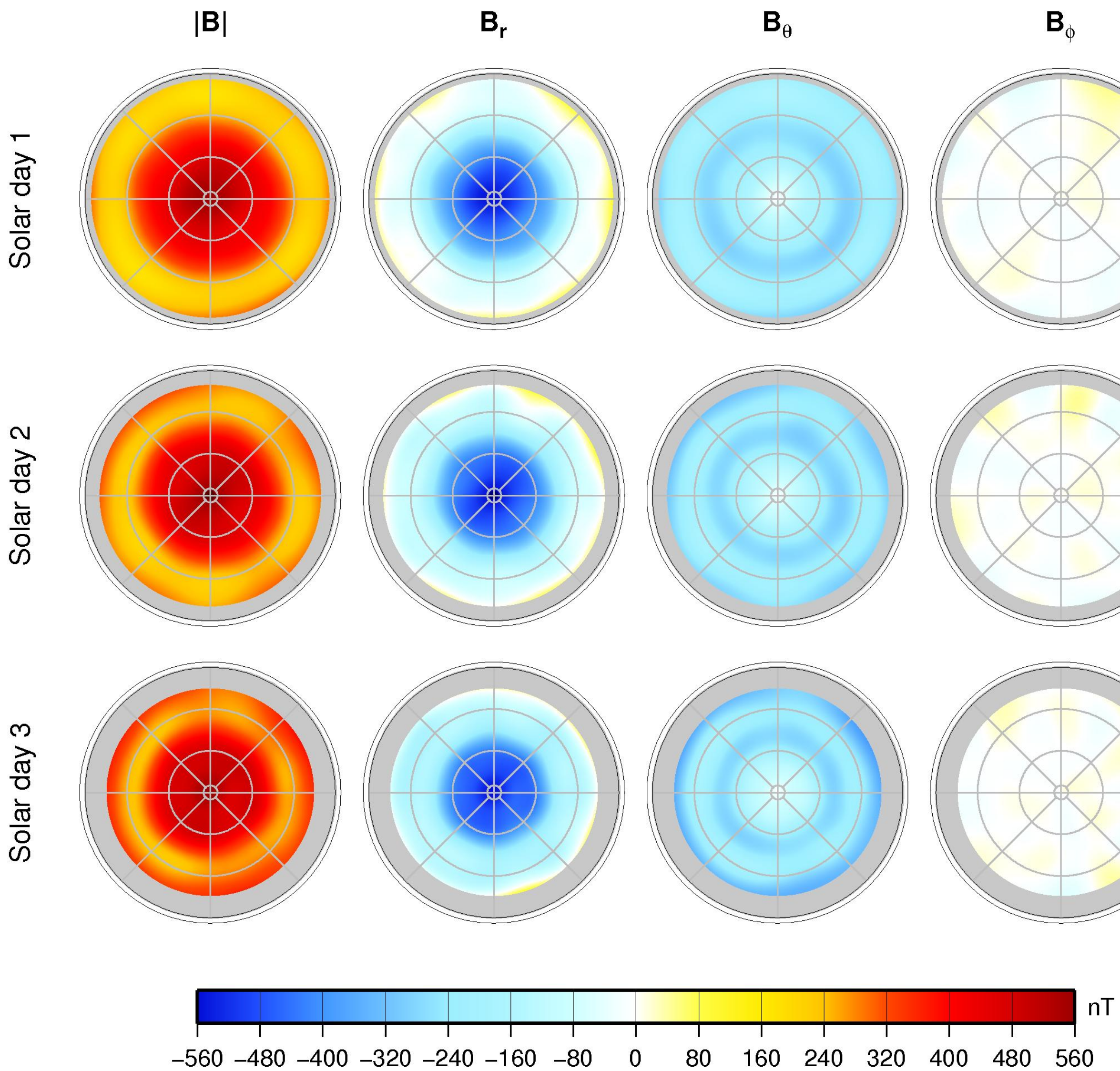

Figure 4.16: Stereographic projection maps of the magnetic field intensity $|\mathbf{B}|$ and its spherical components B_r, B_θ, B_ϕ, for the six solar day models. Maps represent the northern hemisphere of Mercury at 200 km altitude, in MBF coordinates. Grid lines (grey) are drawn every $45°$ for longitude and every $30°$ for latitude. The 0° MBF longitude is toward bottom.

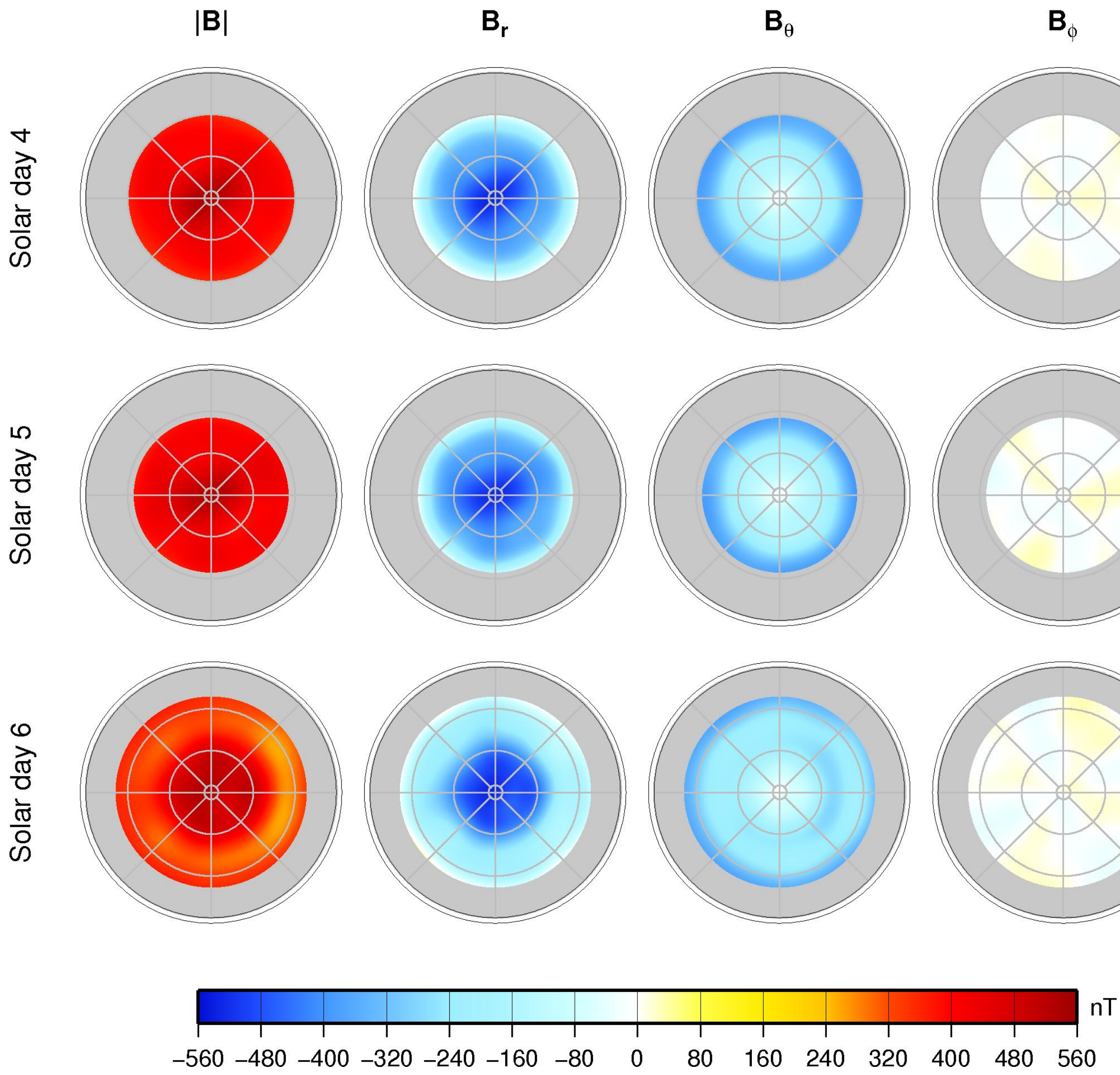

Figure 4.16: (cont.)

Table 4.3: Number of observations retained for inversion, latitudinal threshold, rms of the observed field, iteration chosen, relative misfit and correlation coefficients between the observed field and the model. The observed field rms, the inversion misfit and the correlation coefficient are given for the magnetic field vector and its spherical components B_r, B_θ and B_ϕ.

Solar day	No. of Obs.	Lat. threshold (°)	Observed field rms (nT)				Iteration	σ_B (nT)				Corr. Coeff.			
			B	B_r	B_θ	B_ϕ		**B**	B_r	B_θ	B_ϕ	**B**	B_r	B_θ	B_ϕ
1	100675	5	282.0	243.9	138.0	32.0	16	51.0	25.1	30.8	32.0	0.95	0.99	0.88	0.05
2	112411	11	295.8	260.3	136.2	34.2	16	56.4	30.9	32.5	34.2	0.94	0.98	0.84	0.06
3	157167	16	295.5	263.0	130.2	34.1	17	54.9	30.8	30.3	33.9	0.93	0.98	0.82	0.11
4	167821	31	273.3	245.0	115.8	35.9	9	57.2	33.3	29.9	35.8	0.88	0.96	0.77	0.09
5	168084	35	272.5	244.1	115.2	37.1	9	59.3	34.5	30.8	37.0	0.87	0.95	0.77	0.09
6	178680	22	291.0	259.4	127.5	34.0	13	55.3	31.4	30.2	34.0	0.92	0.97	0.81	0.08
All	884838	5	284.7	252.9	126.0	34.8	20	53.5	27.7	29.8	34.7	0.92	0.97	0.83	0.08

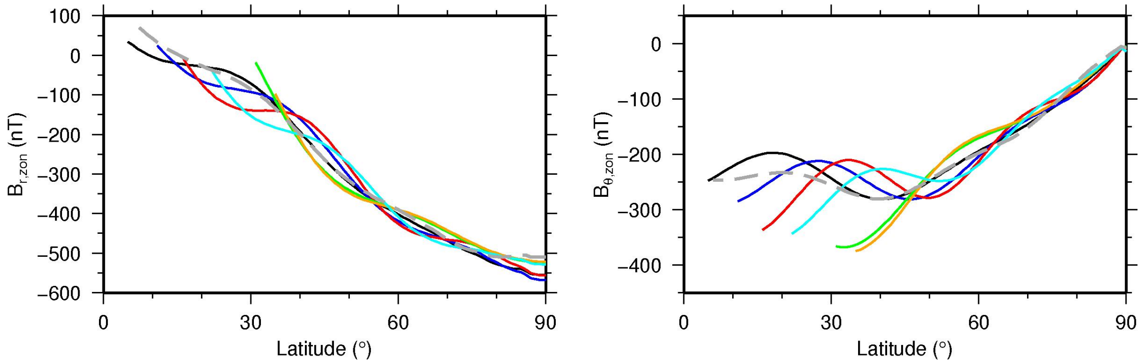

Figure 4.17: Zonal radial (left) and colatitudinal (right) magnetic field as a function of latitude, for the solar day models 1 (black), 2 (blue), 3 (red), 4 (green), 5 (orange) and 6 (cyan). The 6-solar-days model is also shown (dashed gray line). Only latitudes higher than the latitudinal threshold (see Table 4.3) are shown.

of 40°N. The solar day 2 and 3 models are also similar for the same latitude extent. For the zonal latitudinal profile we find the same type of relation: solar days 2 and 3 have latitudinal profiles similar for latitudes north of 30°N, and solar days 4 and 5 are similar from latitudes north of 50°N. This shows that at some times (but not always) and at some latitudes (but not everywhere) the temporal variation is weak.

4.4 6-solar-day model

Finally, the TD-ESD method is applied to all sidereal days (or to all solar days) together. As above, the scheme described in Section 3.2 of the Draft Manuscript is used to choose the optimal solution. Figure 4.15 shows the trade-off curve for the 6-solar-day case. The threshold latitude of the 6-solar-day model is computed as for the sidereal days (also shown in Table 4.3), corresponding to the threshold latitude of solar day 1. Again, the SV is not modeled. Maps of the 6-solar-day model are shown in Figure 4.18, and the corresponding statistics in Table 4.3. The residuals are roughly weaker than those of the solar day models. This is probably due to the higher chosen iteration. A dominantly axisymmetric field is also found when modeling all days together. This axisymmetry is quantified by the ratio of non-zonal to total modeled magnetic field, which is 8%, for the radial component. The zonal profile is shown in Figure 4.17. Note that the 6-solar-day

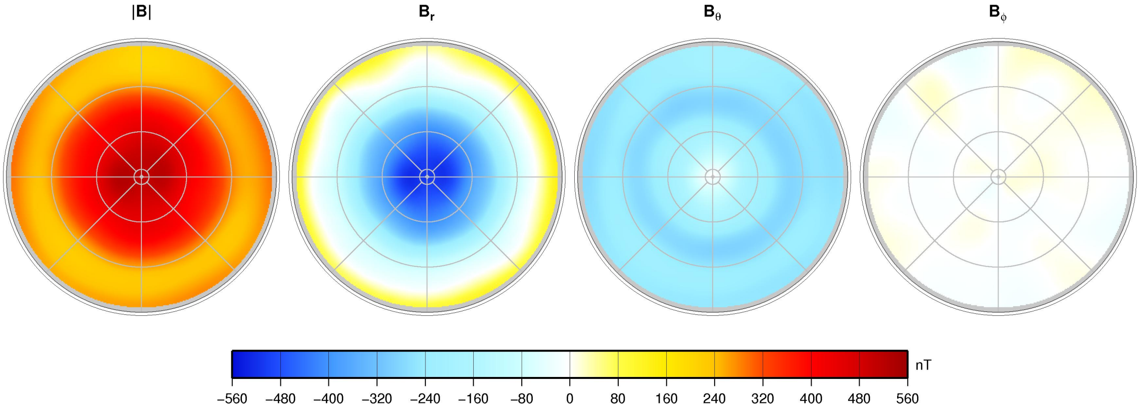

Figure 4.18: Stereographic projection maps of the magnetic field intensity and its spherical components B_r, B_θ, B_ϕ, for the 6-solar-day model. Maps represent the northern hemisphere of Mercury at 200 km altitude, in MBF coordinates. Grid lines (grey) are drawn every $45°$ for longitude and every $30°$ for latitude. The 0° MBF longitude is toward bottom.

model profile is very similar to that the solar day 1 model for latitudes 40°N - 70°N. However, the magnetic equator position is at higher latitudes on average for the 6-solar-day. Note that both solar day 1 and 6-solar-day models have the same latitudinal coverage range.

4.5 Discussion

4.5.1 Magnetic field residuals and the external field

The magnetic field residuals maps of the sidereal day models, as seen in section 4.2, show features co-rotating in MBF system and repeating under similar local time. This is suggestive of external origin. In Figure 4.19 the magnetic field residuals of the second and third MESSENGER Hermean year are shown in MSO coordinates. The first Hermean year is not shown because of the measurements gap. The magnetic field residuals seem to be larger scale in the MSO frame, and are rather similar for both Hermean years. The radial residual presents a very intense positive region in the Sun's direction (day side), while the night side presents a roughly negative residual. The B_θ residual presents in the day side a negative region near the equator, and a positive region near the pole. In the night side, the

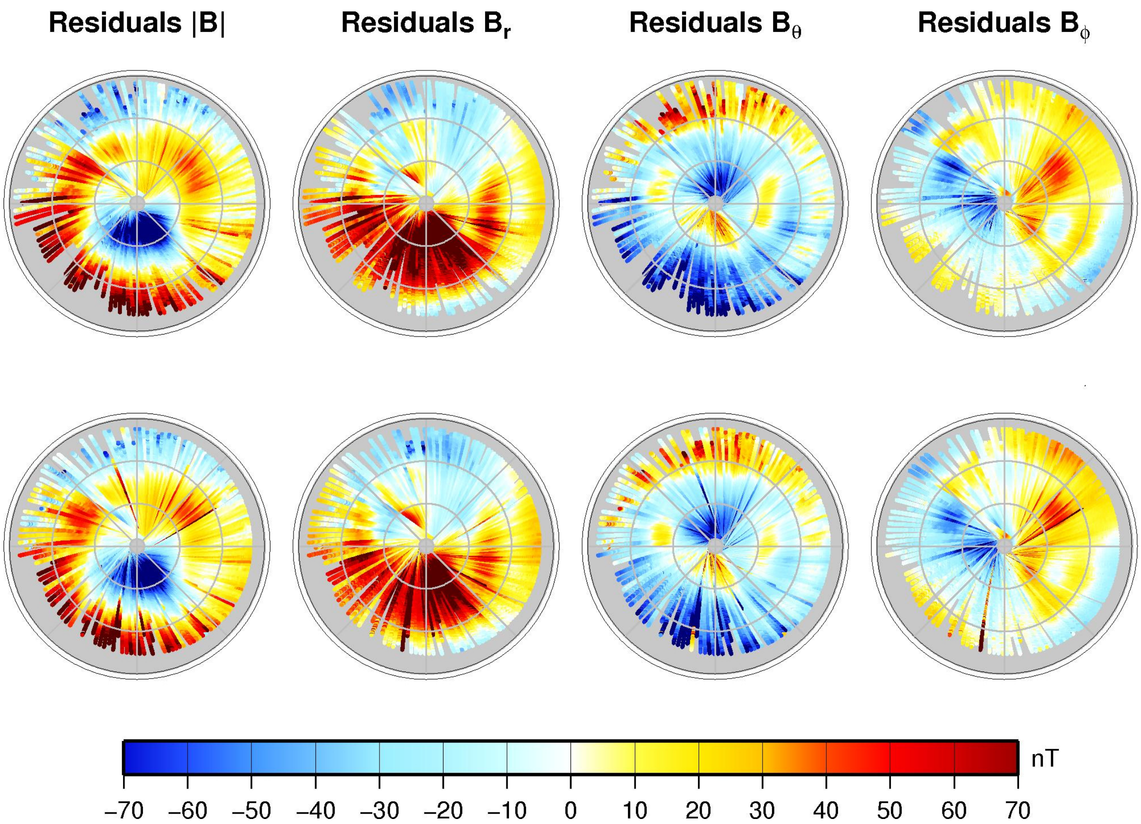

Figure 4.19: Magnetic field residual maps (descending node) above the northern hemisphere of Mercury at spacecraft altitude in MSO coordinates, for the second (top) and third (bottom) MESSENGER Hermean year. The 0° MSO longitude is toward bottom (pointing to the Sun).

inverse situation is observed. The B_ϕ component shows roughly one positive hemisphere (noon to midnight), while the other is negative.

Positive residuals means that the measured magnetic field is stronger than the modeled one, while negative residuals correspond to a weaker measured field. The radial residual maps are consistent with the Chapman-Ferraro field illustrated in Figure 2.7, in which the current sources are located in the magnetopause region toward the Sun. This external field pushes the internal Hermean field, provoking a stronger and positive measured field in the day side. The negative/positive equatorial night side field of the radial/latitudinal components are probably a result of the magnetotail currents located in that midnight direction.

4.5.2 Assessing the SH of the internal field model

As highlighted in Chapter 3.2, models are probably contaminated by magnetic field of an external origin. However, accounting for data over longer periods is likely to reduce the external field contamination. Doing this, we may compare the TD-ESD models converted into an SH internal solution to previously published internal field models.

The solar-day and all-days models are the ones suitable for SH conversion. The B_r field at 200 km altitude above the northern hemisphere down to the respective threshold latitude (Fig. 4.16 and 4.18) is fitted with low-degree SH terms, for each model. These fitted models have to be taken with caution as it is based on a partial spatial data coverage.

The dominant zonal field morphology motivates searching for an expansion with zonal Gauss coefficients. Only using a g_1^0 and a g_2^0 does not adequately explain our models and adding a g_3^0 term significantly decreases the misfit. Additional SH zonal terms do not contribute to a significant decrease of the misfit and are therefore disregarded. Therefore, only zonal coefficients up to degree 3 are considered here. The equatorial dipole coefficients g_1^1 and h_1^1 are included in order to assess the dipole tilt (or at least its upper bound). With just these 5 Gauss coefficients, the misfit between the TD-ESD and the SH-derived B_r maps varies between 20 and 31 nT.

It is difficult to assess the associated error of the resulting Gauss coefficients. The modeling variances are very small (less than 1 nT), but non-diagonal terms in the covariance matrix of the SH inversion are significant, highlighting the existing covariance between different Gauss coefficients. Because the azimuthal coverage is complete, zonal and non-zonal terms are decoupled nonetheless. Using directly the diagonal elements of the covariance matrix to estimate the errors would give unrealistically small values. Instead an estimation of the SH error is based on the error of the TD-ESD method. The iteration that corresponds to the double of the arbitrary value of 10% is used to chose the TD-ESD model that is retained in order to compute the associated Gauss coefficients error.

In Table 4.4 the obtained Gauss coefficients are presented together with those of a previous Hermean internal field model (Anderson et al., 2012) as well as a geomagnetic field model POMME-4.1 (Maus et al., 2006) scaled to Hermean geometry. All TD-ESD models show a dominantly axial dipole within a range [-244.3 , -187.9] nT, except solar day 4 and 5 models where an axial quadrupole overwhelmingly dominates. These two models have a poor latitudinal coverage. Therefore, results of solar day 4 and 5 models are not interpreted. Solar day 1 and 6-solar-day models are the only ones with an axial quadrupole stronger than the axial octupole. This is an evidence for a very correlated g_2^0 and g_3^0 coefficients for a partial coverage set, as highlighted in Figure 3.2. The tilt angles obtained for all models interpreted here are lower than 1.8°. These tilt values for Mercury are much smaller than the geomagnetic dipole tilt at present (Maus et al., 2006) and in the past centuries (Amit and Olson, 2008).

As the 6-solar-day model is the model best constrained because it contains more measurements, it is considered the preferred one for comparison with previous studies. Our g_2^0/g_1^0 ratio is significantly higher and our g_3^0/g_1^0 ratio is lower than the respective values obtained by Anderson et al. (2012). The g_2^0/g_1^0 ratio at Mercury's surface is much stronger than at Earth's mid-mantle. However, the g_3^0/g_1^0 ratio is of the same order (but with an opposite sign). The very small non-zonal terms of our model give a tilt value of 0.92°, somewhat similar to the upper bound value of 0.8° obtained by Anderson et al. (2012).

The zonal Gauss coefficients from Table 4.4 are used to plot the fitted zonal profile of B_r (red curve in Fig. 4.20), for all solar day models. The misfit of 31.8 nT of the solar day 3 is higher than those of the other models. In general, the fitted curves explains well the main trend of the models, which however clearly shows higher complexity.

Extrapolating the SH curve of the 6-solar-day model to the southern hemisphere would give a north-to-south-pole magnetic field magnitude ratio of 4, i.e. the asymmetry with respect to the geographic equator is strong. For comparison, the extrapolated north-to-south-pole ratio based on the Gauss coefficients of Anderson et al. (2012) is 2.7 corresponding also to a significantly larger asymmetry. Our larger g_2^0/g_1^0 ratio is therefore even more challenging for Mercury dynamo models (Cao et al., 2014).

4.5.3 Are solar day models compatible with a secular variation?

Differences between the solar day models are computed, in order to seek for any possible temporal variation signature. These maps are shown in Figure 4.21. The corresponding statistics are computed only for latitudes that are well described by both solar day models, and are shown in Table 4.5.

The resulting differences between consecutive solar days are dominantly axisymmetric. This characteristic is not a surprise because the solar day models themselves are axisymmetric. Note that in all differences maps the region from the pole south to 60°N is weaker than for lower latitudes for all components. The intensity of the difference between consecutive solar day models vary substantially with time, but remains lower than 85 nT. This value is comparable with the magnetopause external field value of 80 nT near the geographical equator shown by Johnson et al. (2012). The solar day difference 4-5 maps are very weak in agreement with the lower misfit values in Table 4.5 for these days.

The secular variation is not expected to be so fast in 170 days. A recent study found that no variation of the field between Mariner 10 and MESSENGER is consistent with the measurements, although some variability is possible (Philpott et al., 2014). We should conclude that the field differences computed between the different solar day models are strong and probably arise from external field sources that contaminate our models.

4.6 Conclusion

In this Chapter I applied the TD-ESD method developed to model the magnetic field of Mercury as measured by the MESSENGER spacecraft. Almost three terrestrial years of MESSENGER measurements were modeled. I used the proxy defined in Chapter 3 to select measurements less perturbed by external sources. Because of this, some coverages are limited to a smaller region at the northern hemisphere from 30°N to the North Pole.

Table 4.4: Gauss coefficients fitted to the B_r model obtained from the TD-ESD method for the MESSENGER's solar days at 200 km altitude over the northern hemisphere. Also shown for comparison are the corresponding values from a previous Mercury field model (Anderson et al., 2012) and from the POMME-4.1 model (Maus et al., 2006) downward continued to the $R_{\oplus}^{h}$ depth inside the Earth's mantle (see section 4.1 of the Draft Manuscript).

	Model								
	1	2	3	4	5	6	All	Anderson et al. (2012)	POMME-4.1
g_1^0	-212.8 ± 8.9 nT	-223 ± -1.4 nT	-244.3 ± 16.6 nT	3.5 ± 33.0 nT	-53.5 ± 79.7 nT	-234.3 ± 74.8 nT	-187.9 ± 5.2 nT	-190 ± 10 nT	-71792.2 nT
g_2^0	-45.2 ± 13.6 nT	-27.4 ± 0.9 nT	4.4 ± 27.1 nT	-384.9 ± 49.2 nT	-304.3 ± 115.9 nT	-21.6 ± 120.3 nT	-90.6 ± 4.6 nT	-74.6 ± 4.0 nT	-7586.4 nT
g_3^0	-44.3 ± 7.5 nT	-54.1 ± -2.1 nT	-62.8 ± 12.8 nT	124.8 ± 20 nT	93 ± 45.9 nT	-43.3 ± 59.3 nT	-12.5 ± 2.4 nT	-22.0 ± 1.3 nT	5862.6 nT
g_1^1	-2.8 ± 6.5 nT	3.5 ± 1.0 nT	2.5 ± 1.2 nT	8.3 ± 2.4 nT	5.2 ± 0.7 nT	3.6 ± 0.7 nT	1.1 ± 0.3 nT	-	-4085.22 nT
h_1^1	-1.5 ± 5.4 nT	6.1 ± 3.4 nT	7.1 ± 4.3 nT	0 ± 5.3 nT	-5.8 ± 2.6 nT	4.8 ± 6.8 nT	2.8 ± 1.3 nT	-	12385.31 nT
θ_0	0.86 °	1.81 °	1.76 °	67.14 °	8.28 °	1.47 °	0.92 °	< 0.8 °	10.3 °
g_2^0/g_1^0	0.212 ± 0.065	0.123 ± 0.004	-0.018 ± 0.111	-109.971 ± 1036.969	5.688 ± 8.746	0.092 ± 0.514	0.482 ± 0.028	0.392 ± 0.010	0.106
g_3^0/g_1^0	0.208 ± 0.036	0.243 ± 0.010	0.257 ± 0.063	35.657 ± 336.196	-1.738 ± 2.599	0.185 ± 0.285	0.067 ± 0.011	0.116 ± 0.009	- 0.082

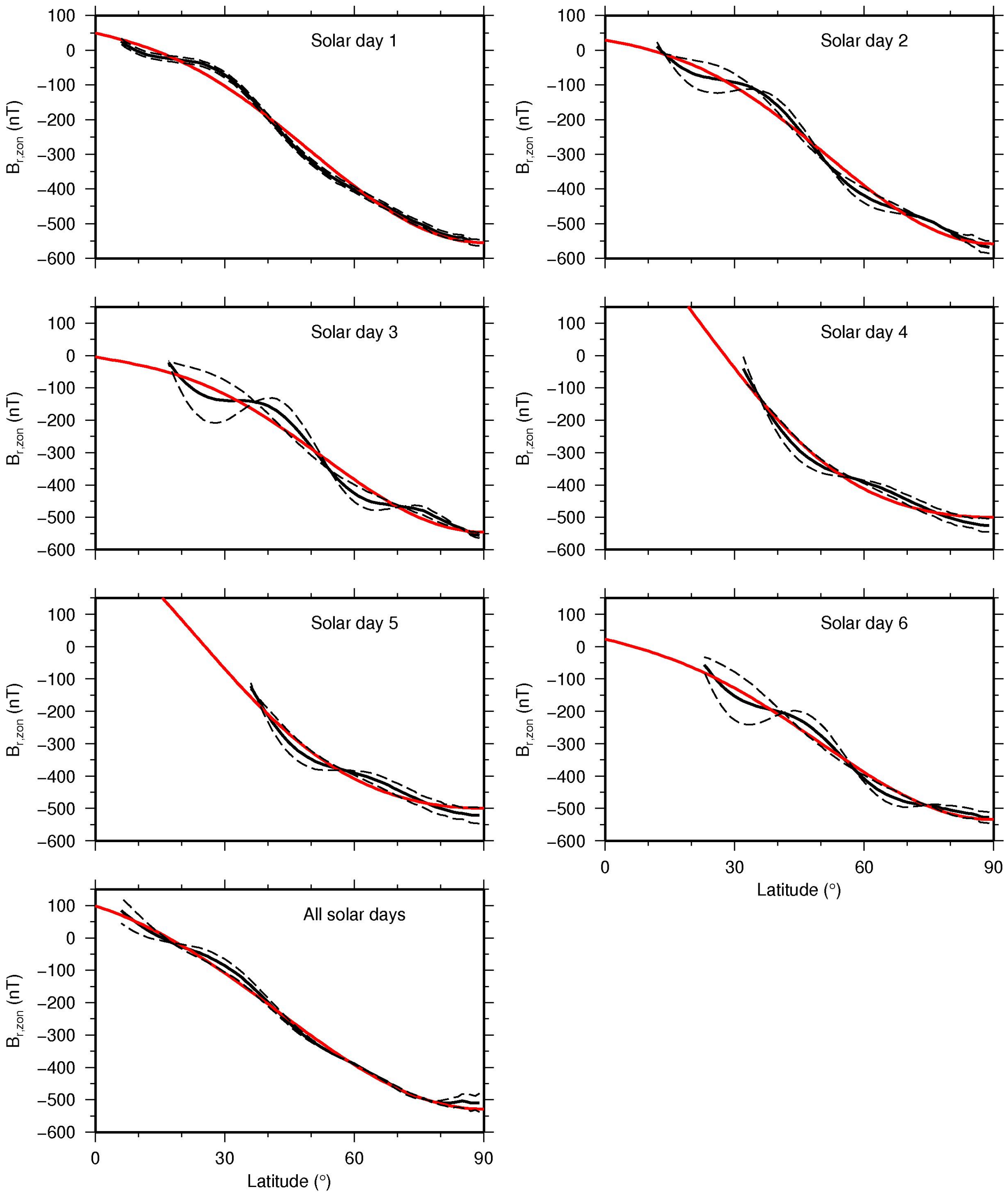

Figure 4.20: Zonal radial magnetic field (black solid lines) and the corresponding mean with one standard deviation bounds (dashed lines, representing rms non-zonal field), as a function of latitude. Only latitudes higher than the latitudinal threshold are shown. The corresponding profile from fitted Gauss coefficients to the TD-ESD models are also shown (red solid lines).

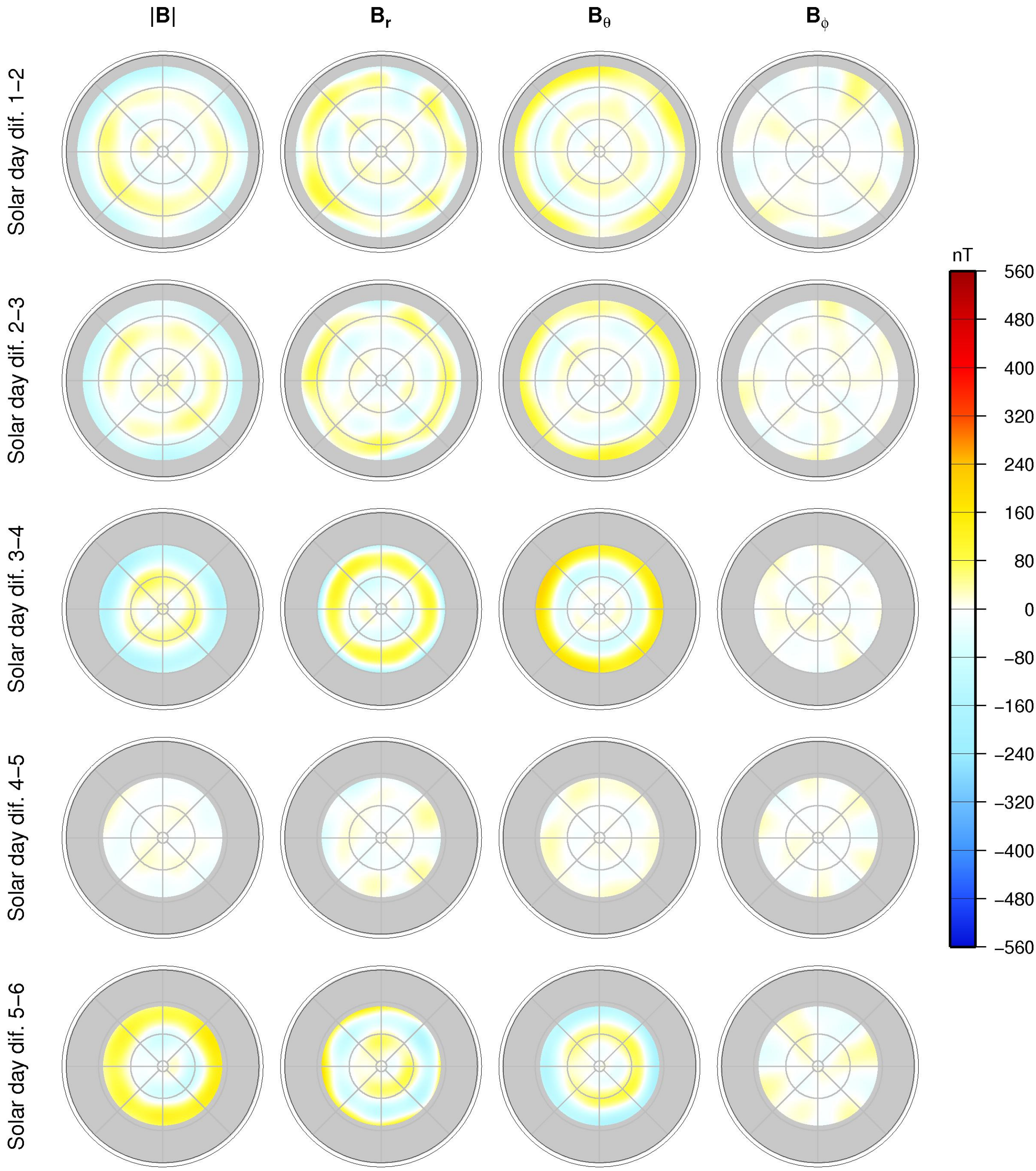

Figure 4.21: Stereographic projection maps of the magnetic field differences between two consecutive solar day models. Maps represent the northern hemisphere of Mercury at 200 km altitude, in MBF coordinates. The 0° MBF longitude is toward bottom.

Table 4.5: Misfit and correlation coefficients between two consecutive solar day models. Values are given for the magnetic field vector and its spherical components B_r, B_θ and B_ϕ.

Solar day dif.	σ_B (nT)				Corr. Coeff.			
	B	B_r	B_θ	B_ϕ	**B**	B_r	B_θ	B_ϕ
1-2	42.8	28.3	29.3	13.1	0.98	0.99	0.93	0.14
2-3	42.1	27.0	30.5	10.6	0.98	0.99	0.94	0.45
3-4	83.3	48.9	66.6	10.5	0.88	0.94	0.80	0.47
4-5	19.4	13.8	10.1	9.2	0.99	0.99	0.99	0.74
5-6	79.3	49.7	59.6	16.6	0.87	0.92	0.83	0.29

Eighteen sidereal day models were computed and interpreted. All sidereal day models exhibit a dominantly axisymmetric field. However, some small-scale features still move around the planetary rotation axis in the models and in the corresponding residuals. These features are interpreted as being from external origin, because of its periodicity of three sidereal days.

The solar day models are also computed because it allows each Hermean longitude to experience all local hours. The resulting field is much more axisymmetric, without small-scales moving around the planetary rotation axis. It should be again emphasized that using an inversion method which allows for non-axisymmetric field and small-scale features to be modeled, those structures are in general absent and a large-scale and dominantly zonal solar day magnetic field models are obtained. Latitudinal thresholds are then computed for each solar day coverage, in order to obtain the region where the field is reliable.

I studied the variability from one solar day model to another, through differences between consecutive solar days. Zonal axisymmetric differences are obtained, corresponding to a fast temporal variation. The rms of the difference between two consecutive solar days are of the order of the magnetopause external field of Johnson et al. (2012), suggesting that a strong large-scale external field is being modeled together with the internal field.

The solar day TD-ESD models are converted into spherical harmonic models, in order to compare with previous works. As mentioned in Chapter 3, converting a partial coverage into a global SH model inherently introduces errors. When comparing our 6-solar-day model (using all 6 solar days together) converted to SH Gauss coefficients with the model of Anderson et al. (2012), we observe a strong resemblance. Note that no external field treatment were performed with our TD-ESD models, contrary to Anderson et al. (2012) that modeled the internal part of the field based on magnetic equator average crossings in their dipole offset model.

This study provides important information about the external field contamination. The external field has a large-scale component that varies relatively fast (an order of a solar day). Such details are needed to jointly model the external and internal sources, in order to achieve an internal magnetic field model that may constrain the internal physical processes in Mercury's core.

Summary

Mercury, the smallest and closest to the Sun of the telluric planets of our Solar System, has been studied since 1974 from space, after the first flyby performed by the Mariner 10 spacecraft. Measurements obtained during this and the subsequent flybys allowed to measure a present-day magnetic field, whose origin has been attributed to the existence of a possible core dynamo inside the planet, the same physical process that generates Earth's magnetic field. Because of Mercury's particular small size that might mean a completely or almost completely frozen core, subsequent space missions such as the NASA MESSENGER and the ESA/JAXA BEPI COLOMBO missions have been and are still being elaborated with as one of the main scientific goals to constrain the origin and dynamics of Mercury's magnetic field. The MESSENGER mission, orbiting Mercury since 2011, has already provided unprecedented information about the planet's surface, interior, exosphere and magnetosphere.

In this study, I focused on the magnetic field of Mercury as measured by the MESSENGER magnetometer (MAG) instrument. Due to its eccentric orbit around Mercury, the magnetic field coverage as measured from the spacecraft is not global and only covers the northern hemisphere. New methods overcoming this strong limitation have to be developed in order to produce a model for the magnetic field of Mercury and its temporal variation in agreement with such observations. My main concern was to develop a method to deal with this present limitation in the magnetic field coverage around Mercury and still improve our knowledge of the Hermean field.

Here I proposed a new method called Time Dependent Equivalent Source Dipoles

(TD-ESD) in order to model a magnetic field over a limited spatial region. This method is based on the Equivalent Source Dipoles method primarily used successfully to reduce the geomagnetic field to a constant altitude, and later to model the static lithospheric magnetic field. My main contribution was to place the dipoles grid at deeper depths and introduce a linear variation in time for the dipoles magnetization. This allows to model a magnetic field produced by a deep and dynamic dynamo source.

I performed and implemented a series of tests to investigate the different factors that affect the inverted solution. Tests have been performed with a synthetic field both distributed over a regular grid, as well as distributed over MESSENGER selected orbits. The performance of the method was tested for different input parameters. It was found that a number of model dipoles leading to an horizontal resolution of 9.6° is a good compromise between the fit to the measurements and the computational cost. I chose a dipole mesh depth of 640 km, but other depths (in particular shallower) could also be used since the results are weakly sensitive to the depth at which the dipoles are located. The magnetic field is successfully and reliably downward and upward continued. For data ideally distributed on the regular grid, the altitude range is -300 to 1460 km, while for data distributed over the spacecraft orbits this range is restricted to 10 to 970 km. These tests also showed that it is not possible to adequately assess the secular variation within two sidereal days separated by one year.

The method was applied to eighteen sidereal days as measured by MESSENGER, equivalent to almost three terrestrial years. A proxy was defined to select the measurements less perturbed by the external sources. The TD-ESD method scheme was then applied to obtain the various sidereal day models. It was found that a dominantly axisymmetric magnetic field, with small-scale features rotating around the planetary spin axis with four sidereal days periodicity, are consistent with the observations of Mercury's magnetic field by MESSENGER. These small-scale features were interpreted as of external origin. These results are consistent with other studies, in the sense that they support a strong external field environment present on Mercury (Johnson et al., 2012).

This solar day periodicity in the small-scale features motivated to apply the TD-ESD method to a complete solar day, equivalent to 170 terrestrial days. Six such solar day models were obtained. These models show a magnetic field much more axisymmetric than obtained with the sidereal days models, with little small-scale features. However, a strong temporal variability of this zonal field over the different solar days is found. This field variability is interpreted as originating from a large-scale external field, as expected from a magnetopause contribution, that strongly contaminates the TD-ESD models.

I also converted the TD-ESD solar-day models into a spherical harmonic solution. The most robust model, corresponding to all 18 sidereal days modeled together with the TD-ESD method, shows a dominantly axial dipolar field. It also shows a stronger quadrupole-to-dipole ratio of 0.48 ± 0.03 and a weaker octupole-to-dipole ratio of 0.07 ± 0.01 compared to those obtained by Anderson et al. (2012). A very small tilt of $0.92°$ is also obtained from the converted 6-solar-day model, slightly larger than the upper bound found by Anderson et al. (2012).

I emphasize that using an inversion scheme which allows for non-axisymmetric and small-scale features to be modeled, those structures were in general not found. A large-scale and dominantly zonal magnetic field for the solar day models is obtained. Even if there is an external source contamination, the results from this work provide a strong evidence for the large-scale and close-to-axisymmetry structure of the internal field. A large-scale and axisymmetric internal magnetic field for Mercury strongly supports the dynamo model with a stable stratified layer at the top of the core proposed by Christensen (2006). No signature of a tangent cylinder was found, not even near the equator (the case for a thin shell), meaning that a thin shell dynamo (Stanley et al., 2005; Takahashi and Matsushima, 2006) is not expected to be the source of the Hermean internal magnetic field. From the observed variability when comparing the different solar day models, an induced field from a feedback dynamo process could be present on Mercury.

This study demonstrates that regional methods can be used to model the planetary magnetic field when the data set is not globally distributed. In order to detect a possible (and probably weak) secular variation, measurements provided by the future Bepi-Colombo mission would be compared to the actual MESSENGER data. The TD-ESD method will be appropriate to combine measurements from both MESSENGER and Bepi-Colombo missions.

Future work

The tests performed in this work regarding the secular variation were probably too simplistic. In order to better understand the true limit of the TD-ESD method, a new test should be performed. For example, instead of a data set composed of two coverages separated by one year, a continued data coverage during more than one year could be a better way to proceed. Also, the periodic time variations that were found from one sidereal day to the other, suggest that the linear time variation implemented in the TD-ESD method is probably oversimplified. A cubic spline basis could be a better solution.

Other regional methods such as the Spherical Harmonic Caps Analysis (Thébault et al., 2006) could also obtain interesting results to be compared with those that I obtained using the TD-ESD method. However, an external field contribution should still probably be jointly required, as explained above.

The unexpected revolution on spatial engineering has made possible the extension of the MESSENGER mission up to 2 years, and even better with a periapsis at very low altitudes (lower than 15 km). Studying the magnetic field at such low altitudes will probably give information about the very small-scale field that is not measurable at nominal mission altitudes. The ESD method could probably give good resolution maps of the crustal magnetic field. Later, a correction of this crustal field could be applied to the core field.

The evidence of external field sources present in our solar day models calls for a future development of a method that jointly models the internal and external fields. This could be performed by implementing an external dipole co-rotating with the Sun in MSO frame, while the internal field continues to be modeled through the dipoles in the MBF frame as in this thesis. This external dipole would allow to model a large-scale external field that is presently contaminating the TD-ESD models. After a successful internal/external field separation the corresponding internal SH model would provide a new constraint on dynamo models (Wicht and Heyner, 2014).

The future BepiColombo mission will provide global magnetic field measurements. However, as the secular variation of Mercury is expected to be slow, it is necessary to model jointly the new data with the actual partial MESSENGER data. The TD-ESD, could be used to this task.

Appendices

Appendix A

Spherical harmonic (SH) model

The magnetic field **B** verifies the Maxwell equations below,

$$\nabla \times \mathbf{B} = \mu_0 \mathbf{J} \tag{A.1}$$

$$\nabla \cdot \mathbf{B} = 0 \tag{A.2}$$

Where **J** is the current density and μ_0 is the permeability for free space. From equation A.1 we can say that **B** is a scalar potential gradient, when we are in a region without sources, i. e. $\mathbf{J} = 0$. Then,

$$\mathbf{B} = -\nabla V \tag{A.3}$$

and from equation A.2 we obtain the Laplace equation, for the scalar potential V:

$$\nabla^2 V = 0 \tag{A.4}$$

In spherical coordinates (r, θ, ϕ), this equation takes the form,

$$\frac{1}{r}\frac{\partial^2 (rV)}{\partial r^2} + \frac{1}{r^2 \sin\theta}\frac{\partial}{\partial \theta}\left(\sin\theta \frac{\partial V}{\partial \theta}\right) + \frac{1}{r^2 \sin^2\theta}\frac{\partial^2 V}{\partial \phi^2} = 0 \tag{A.5}$$

Gauss showed that the solution of this equation can be written in the form of spherical harmonics of the potential. That is,

$$V_{n,m}(r,\theta,\phi) = \left[A_n r^n + B_n r^{-(n+1)}\right]\left[a_m \cos m\phi + b_m \sin m\phi\right] P_{n,m}(\cos\theta) \tag{A.6}$$

where $P_{n,m}$ are the associate Legendre functions and n, m are integers.

$$P_{n,m}(\mu) = \left(1-\mu^2\right)^{\frac{m}{2}} \frac{d^m P_n(\mu)}{d\mu^m} \tag{A.7}$$

whith $\mu = \cos\theta$, where $P_n(\mu)$ are the Legendre polynomials.

The general solution for Laplace's equation, A.6, can then be written,

$$\begin{aligned} V(r,\theta,\phi) = a\sum_{n=1}^{\infty}\sum_{m=0}^{n}\{(g_n^m \cos m\phi + h_n^m \sin m\phi)\left(\frac{a}{r}\right)^{n+1} + \\ + (q_n^m \cos m\phi + s_n^m \sin m\phi)\left(\frac{r}{a}\right)^{n}\}P_n^m(\theta) \end{aligned} \tag{A.8}$$

The equation A.8 is the potential expansion in spherical harmonics, with a the surface of reference, and r the surface where we want to obtain the potential.

The functions $P_n^m(\theta)\cos m\phi$ and $P_n^m(\theta)\sin m\phi$ are the spherical harmonics, and g_n^m, h_n^m, q_n^m e s_n^m are the spherical harmonic coefficients.

Studying equation A.8, the term $\left(\frac{a}{r}\right)^{n+1}$ is zero when r is going to infinity, meaning that this parcel describes the potential of internal sources at the surface reference ($r = a$), usually the Earth's surface. On the other hand the term $\left(\frac{r}{a}\right)^{n}$ is zero when r is going to zero, and that means that this parcel describes the external sources.

Finaly, using the equation A.3, we obtain the three magnetic field components below,

$$B_r = \sum_{n=1}^{\infty}\sum_{m=0}^{n}\{(n+1)\left[g_n^m \cos m\phi + h_n^m \sin m\phi\right]\left(\frac{a}{r}\right)^{n+2} -$$
$$- n\left[q_n^m \cos m\phi + s_n^m \sin m\phi\right]\left(\frac{r}{a}\right)^{n-1}\}P_n^m(\theta) \tag{A.9}$$

$$B_\theta = -\sum_{n=1}^{\infty}\sum_{m=0}^{n}\{\left[g_n^m \cos m\phi + h_n^m \sin m\phi\right]\left(\frac{a}{r}\right)^{n+2} +$$
$$+ \left[q_n^m \cos m\phi + s_n^m \sin m\phi\right]\left(\frac{r}{a}\right)^{n-1}\}\frac{dP_n^m(\theta)}{d\theta} \tag{A.10}$$

$$B_\phi = \frac{1}{\sin\theta}\sum_{n=1}^{\infty}\sum_{m=0}^{n} m\{\left[g_n^m \sin m\phi - h_n^m \cos m\phi\right]\left(\frac{a}{r}\right)^{n+2} +$$
$$+ \left[q_n^m \sin m\phi - s_n^m \cos m\phi\right]\left(\frac{r}{a}\right)^{n-1}\}P_n^m(\theta) \tag{A.11}$$

Appendix B

Equivalent source dipole (ESD) model

The ESD method consists in treating a material as a dipole distribution with a given thickness, and finding the resulting magnetic field outside the region magnetized. With this, we obtain the magnetic field at a constant altitude above the region where we have the dipole sources Langlais et al. (2004).

The magnetic potential, observed at (r, θ, ϕ), is defined as

$$V = -\mathbf{M} \cdot \nabla \frac{1}{l} \tag{B.1}$$

Where **M** is the magnetic moment of a point dipole located at (r_d, θ_d, ϕ_d). This relation is valid when there are no sources between the observation point and the dipole. The distance l is defined as

$$l = \left(r_d^2 + r^2 - 2r_d r \cos(\zeta)\right)^{\frac{1}{2}} \tag{B.2}$$

Where ζ is the angle between the two position vectors, and $cos(\zeta)$ can be written

$$\cos(\zeta) = \cos(\theta)\cos(\theta_d) + \sin(\theta)\sin(\theta_d)\cos(\phi - \phi_d) \tag{B.3}$$

Re-writing the equation B.1, we have

$$V(r,\theta,\phi) = \frac{M_r(rA_1 - r_d) - M_\theta r B_1 + M_\phi r C_1}{l^3} \tag{B.4}$$

Where the coefficients are:

$$\begin{aligned}
A_1 &= \cos(\theta)\cos(\theta_d) + \sin(\theta)\sin(\theta_d)\cos(\phi - \phi_d) = \cos(\zeta) && \text{(B.5)}\\
B_1 &= \cos(\theta)\sin(\theta_d) - \sin(\theta)\cos(\theta_d)\cos(\phi - \phi_d) && \text{(B.6)}\\
C_1 &= \sin(\theta) sin(\phi - \phi_d) && \text{(B.7)}
\end{aligned}$$

The total magnetic field **B** comes from the equation A.3 in spherical coordinates,

$$\mathbf{B} = -\left(\frac{\partial}{\partial r}, \frac{\partial}{r\partial\theta}, \frac{\partial}{r\sin(\theta)\partial\phi}\right) V \tag{B.8}$$

Deriving A_1, B_1 and C_1 in relation to θ and ϕ we define,

$$\begin{aligned}
A_2 &= \frac{\partial A_1}{\partial\theta} = -\sin(\theta)\cos(\theta_d) + \cos(\theta)\sin(\theta_d)\cos(\phi - \phi_d) && \text{(B.9)}\\
B_2 &= \frac{\partial B_1}{\partial\theta} = -\sin(\theta)\sin(\theta_d) - \cos(\theta)\cos(\theta_d)\cos(\phi - \phi_d) && \text{(B.10)}\\
C_2 &= \frac{\partial C_1}{\partial\theta} = \cos(\theta)\sin(\phi - \phi_d) && \text{(B.11)}\\
A_3 &= \frac{\partial A_1}{\sin(\theta)\partial\phi} = -\sin(\theta_d)\sin(\phi - \phi_d) && \text{(B.12)}\\
B_3 &= \frac{\partial B_1}{\sin(\theta)\partial\phi} = \cos(\theta_d)\sin(\phi - \phi_d) && \text{(B.13)}\\
C_3 &= \frac{\partial C_1}{\sin(\theta)\partial\phi} = \cos(\phi - \phi_d) && \text{(B.14)}
\end{aligned}$$

Finally, we can write the expressions to the three components of the magnetic field, using equations B.4, and the partial derivatives above:

$$B_r = M_r \frac{\frac{3D_1\ F_1}{l^2} - A_1}{l^3} + M_\theta \frac{\frac{3D_1\ F_2}{l^2} + B_1}{l^3} + M_\phi \frac{\frac{3D_1\ F_3}{l^2} - C_1}{l^3} \tag{B.15}$$

$$B_\theta = M_r \frac{\frac{3D_2\ F_1}{l^2} - A_2}{l^3} + M_\theta \frac{\frac{3D_2\ F_2}{l^2} + B_2}{l^3} + M_\phi \frac{\frac{3D_2\ F_3}{l^2} - C_2}{l^3} \tag{B.16}$$

$$B_\phi = M_r \frac{\frac{3D_3\ F_1}{l^2} - A_3}{l^3} + M_\theta \frac{\frac{3D_3\ F_2}{l^2} + B_3}{l^3} + M_\phi \frac{\frac{3D_3\ F_3}{l^2} - C_3}{l^3} \tag{B.17}$$

Where, $D_1 = r - r_d A_1$, $D_2 = -r_d A_2$, $D_3 = -r_d A_3$, $F_1 = rA_1 - r_d$, $F_2 = -rB_1$ and $F_3 = rC_1$.

Appendix C

The inverse problem

The inverse problem is an algebraic formulation of the problem that consists in obtaining the parameters of some model (SH or ESD) from measured values of B_r, B_θ, and B_ϕ. It is written as

$$\tilde{b} = \tilde{D}x + \tilde{\nu} \tag{C.1}$$

where $\tilde{b}$ is the vector that contains the observations, x is the vector of parameters (unknowns), $\tilde{\nu}$ is the noise vector (of mean zero and covariance matrix W^{-1}), and $\tilde{D}$ is the function matrix that relates the vectors $\tilde{b}$ and x.

The matrix $\tilde{D}$, in the case of spherical harmonics is composed by the factors that are multiplying the gauss coefficients, in equations A.9, A.10,A.11. In the case of the equivalent dipole sources, the matrix $\tilde{D}$ is composed by the partial factors multiplying M_r, M_θ and M_ϕ in equations B.15, B.16, and B.17.

To normalize the vector $\tilde{\nu}$, we multiply the equation C.1 by $W^{\frac{1}{2}}$, giving

$$b = Dx + \nu \tag{C.2}$$

The inverse problem is solved when we find the minimum of $L(x) = \nu^T \nu$, that corresponds to the equation,

$$D^T b = D^T D x \tag{C.3}$$

Conjugate gradient approach

In fact, the computation of $D^T D$ from equation C.3 can be very heavy, and it is better to use the conjugate gradient approach. The minimum of L is reached when it's gradient is zero, $\nabla L = 0$, that means $Dx - b = 0$.

The process is iterative, in each step k, a search direction p_k is generated, and a scalar, α_k, is sought that minimizes $L(x_k + \alpha_k p_k)$. The new solution is $x_{k+1} = x_k + \alpha_k p_k$.

The expression of α_k is

$$\alpha_k = \frac{r_k^T r_k}{p_k^T D^T D p_k} \tag{C.4}$$

Where r_k is

$$r_k = D^T b - D^T D x_k \tag{C.5}$$

Using the matrix identity $p_k^T D^T D p_k = (D p_k)^T D p_k$ in equation C.4, we use directly the D matrix instead of the product $D^T D$ (called the design matrix approach).

Bibliography

Aharonson, O., Zuber, M. T., and Solomon, S. C. (2004). Crustal remanence in an internally magnetized non-uniform shell a possible source for Mercury's magnetic field. *Earth Planet. Sci. Lett.*, 218:261–268.

Alexeev, I. I., Belenkaya, E. S., Slavin, J. A., Korth, H., Anderson, B. J., Baker, D. N., Boardsen, S. A., Johnson, C. L., Purucker, M. E., Sarantos, M., and Solomon, S. C. (2010). Mercury's magnetospheric magnetic field after the first two MESSENGER flybys. *Icarus*, 209:23–39.

Amit, H., Christensen, U. R., and Langlais, B. (2011). The influence of degree-1 mantle heterogeneity on the past dynamo of Mars. *Phys. Earth Planet. Inter.*, 189:63–79.

Amit, H. and Olson, P. (2008). Geomagnetic dipole tilt changes induced by core flow. *Phys. Earth Planet. Inter.*, 166:226–238.

Anderson, B. J., Acuña, M. H., Korth, H., Purucker, M. E., Johnson, C. L., Slavin, J. A., Solomon, S. C., and McNutt, R. L. (2008). The Structure of Mercury's Magnetic Field from MESSENGER's First Flyby. *Science*, 321:82–85.

Anderson, B. J., Acuña, M. H., Korth, H., Slavin, J. A., Uno, H., Johnson, C. L., Purucker, M. E., Solomon, S. C., Raines, J. M., Zurbuchen, T. H., Gloeckler, G., and McNutt, R. L. (2010). The Magnetic Field of Mercury. *Space Sci. Rev.*, 152:307–339.

Anderson, B. J., Acuña, M. H., Lohr, D. A., Scheifele, J., Raval, A., Korth, H., and Slavin, J. A. (2007). The Magnetometer Instrument on MESSENGER. *Space Sci. Rev.*, 131:417–450.

Anderson, B. J., Johnson, C. L., and Korth, H. (2013). A magnetic disturbance index for Mercury's magnetic field derived from MESSENGER Magnetometer data. *Geochem. Geophys. Geosyst.*, 14:3875–3886.

Anderson, B. J., Johnson, C. L., Korth, H., Purucker, M. E., Winslow, R. M., Slavin, J. A., Solomon, S. C., McNutt, R. L., Raines, J. M., and Zurbuchen, T. H. (2011). The Global Magnetic Field of Mercury from MESSENGER Orbital Observations. *Science*, 333:1859–1862.

Anderson, B. J., Johnson, C. L., Korth, H., Winslow, R. M., Borovsky, J. E., Purucker, M. E., Slavin, J. A., Solomon, S. C., Zuber, M. T., and McNutt, Jr., R. L. (2012). Low-degree structure in Mercury's planetary magnetic field. *J. Geophys. Res.*, 117:E00L12.

Anderson, J. D., Colombo, G., Espsitio, P. B., Lau, E. L., and Trager, G. B. (1987). The mass, gravity field, and ephemeris of Mercury. *Icarus*, 71:337–349.

Aurnou, J., Andreadis, S., Zhu, L., and Olson, P. (2003). Experiments on convection in Earth's core tangent cylinder. *Earth Planet. Sci. Lett.*, 212:119–134.

Benkhoff, J., van Casteren, J., Hayakawa, H., Fujimoto, M., Laakso, H., Novara, M., Ferri, P., Middleton, H. R., and Ziethe, R. (2010). BepiColombo - Comprehensive exploration of Mercury: Mission overview and science goals. *Planet. Space Sci.*, 58:2–20.

Benz, W., Anic, A., Horner, J., and Whitby, J. A. (2007). The Origin of Mercury. *Space Sci. Rev.*, 132:189–202.

Bida, T. A., Killen, R. M., and Morgan, T. H. (2000). Discovery of calcium in Mercury's atmosphere. *Nature*, 404:159–161.

Broadfoot, A. L., Shemansky, D. E., and Kumar, S. (1976). Mariner 10 - Mercury atmosphere. *Geophys. Res. Lett.*, 3:577–580.

Cain, J. C., Wang, Z., Kluth, C., and Schmitz, D. R. (1989). Derivation of a geomagnetic model to n = 63. *Geophys. J.*, 97:431–441.

Cameron, A. G. W., Benz, W., Fegley, Jr., B., and Slattery, W. L. (1988). *The strange density of Mercury - Theoretical considerations*, pages 692–708.

Cao, H., Aurnou, J. M., Wicht, J., Dietrich, W., Soderlund, K. M., and Russell, C. T. (2014). A dynamo explanation for mercury's anomalous magnetic field. *Geophys. Res. Lett.*, 41.

Cao, H., Russell, C. T., Christensen, U. R., Dougherty, M. K., and Burton, M. E. (2011). Saturn's very axisymmetric magnetic field: No detectable secular variation or tilt. *Earth Planet. Sci. Lett.*, 304:22–28.

Christensen, U. R. (2006). A deep dynamo generating Mercury's magnetic field. *Nature*, 444:1056–1058.

Christensen, U. R. (2011). Geodynamo models: Tools for understanding properties of Earth's magnetic field. *Phys. Earth Planet. Inter.*, 187:157–169.

Christensen, U. R. and Aubert, J. (2006). Scaling properties of convection driven dynamos in rotating spherical shells and application to planetary magnetic fields. *Geophys. J. Int.*, 166:97–114.

Christensen, U. R., Aubert, J., and Hulot, G. (2010). Conditions for Earth-like geodynamo models. *Earth and Planetary Science Letters*, 296:487–496.

Christensen, U. R. and Tilgner, A. (2004). Power requirement of the geodynamo from ohmic losses in numerical and laboratory dynamos. *Nature*, 429:169–171.

Christensen, U. R., Wardinski, I., and Lesur, V. (2012). Timescales of geomagnetic secular acceleration in satellite field models and geodynamo models. *Geophys. J. Int.*, 190:243–254.

Christensen, U. R. and Wicht, J. (2008). Models of magnetic field generation in partly stable planetary cores: Applications to Mercury and Saturn. *Icarus*, 196:16–34.

Connerney, J. E. P., Acuna, M. H., and Ness, N. F. (1987). The magnetic field of Uranus. *J. Geophys. Res.*, 92:15329–15336.

Connerney, J. E. P., Acuna, M. H., and Ness, N. F. (1991). The magnetic field of Neptune. *J. Geophys. Res.*, 96:19023.

Connerney, J. E. P. and Ness, N. F. (1988). *Mercury's magnetic field and interior*, pages 494–513.

Connerney, J. E. P., Ness, N. F., and Acuna, M. H. (1982). Zonal harmonic model of Saturn's magnetic field from Voyager 1 and 2 observations. *Nature*, 298:44–46.

Cowling, T. G. (1934). The stability of gaseous stars. *Monthly Notices of the Royal Astronomical Society*, 94:768–782.

Dietrich, W. and Wicht, J. (2013). A hemispherical dynamo model: Implications for the Martian crustal magnetization. *Phys. Earth Planet. Inter.*, 217:10–21.

Domingue, D. L., Koehn, P. L., Killen, R. M., Sprague, A. L., Sarantos, M., Cheng, A. F., Bradley, E. T., and McClintock, W. E. (2007). Mercury's Atmosphere: A Surface-Bounded Exosphere. *Space Sci. Rev.*, 131:161–186.

Dyment, J. and Arkani-Hamed, J. (1998). Equivalent source magnetic dipoles revisited. *Geophys. Res. Lett.*, 25(11):2003–2006.

Emilia, D. A. (1973). Equivalent sources used as an analytic base for processing total magnetic field profiles. *Geophysics*, 38:339.

Glassmeier, K.-H., Grosser, J., Auster, U., Constantinescu, D., Narita, Y., and Stellmach, S. (2007). Electromagnetic Induction Effects and Dynamo Action in the Hermean System. *Space Sci. Rev.*, 132:511–527.

Gold, R. E., Solomon, S. C., McNutt, R. L., Santo, A. G., Abshire, J. B., Acuña, M. H., Afzal, R. S., Anderson, B. J., Andrews, G. B., Bedini, P. D., Cain, J., Cheng, A. F., Evans, L. G., Feldman, W. C., Follas, R. B., Gloeckler, G., Goldsten, J. O., Hawkins, III, S. E., Izenberg, N. R., Jaskulek, S. E., Ketchum, E. A., Lankton, M. R., Lohr, D. A., Mauk, B. H., McClintock, W. E., Murchie, S. L., Schlemm, II, C. E., Smith, D. E., Starr, R. D., and Zurbuchen, T. H. (2001). The MESSENGER mission to Mercury: scientific payload. *Planet. Space Sci.*, 49:1467–1479.

Gubbins, D. (2004). *Time Series Analysis and Inverse Theory for Geophysicists*. pp. 272. ISBN 0521819652. Cambridge, UK: Cambridge University Press, April 2004.

Harder, H. and Schubert, G. (2001). Sulfur in Mercury's Core? *Icarus*, 151:118–122.

Harmon, J. K. (2007). Radar Imaging of Mercury. *Space Sci. Rev.*, 132:307–349.

Harmon, J. K., Perillat, P. J., and Slade, M. A. (2001). High-Resolution Radar Imaging of Mercury's North Pole. *Icarus*, 149:1–15.

Harmon, J. K., Slade, M. A., Vélez, R. A., Crespo, A., Dryer, M. J., and Johnson, J. M. (1994). Radar mapping of Mercury's polar anomalies. *Nature*, 369:213–215.

Hauck, S. A., Margot, J.-L., Solomon, S. C., Phillips, R. J., Johnson, C. L., Lemoine, F. G., Mazarico, E., McCoy, T. J., Padovan, S., Peale, S. J., Perry, M. E., Smith, D. E., and Zuber, M. T. (2013). The curious case of Mercury's internal structure. *J. Geophys. Res.*, 118:1204–1220.

Heimpel, M. H., Aurnou, J. M., Al-Shamali, F. M., and Gomez Perez, N. (2005). A numerical study of dynamo action as a function of spherical shell geometry. *Earth and Planetary Science Letters*, 236:542–557.

Heyner, D., Wicht, J., Gómez-Pérez, N., Schmitt, D., Auster, H.-U., and Glassmeier, K.-H. (2011). Evidence from Numerical Experiments for a Feedback Dynamo Generating Mercury's Magnetic Field. *Science*, 334:1690–1693.

Holme, R. and Bloxham, J. (1996). The magnetic fields of Uranus and Neptune: Methods and models. *J. Geophys. Res.*, 101:2177–2200.

Hulot, G. and Le Mouël, J. L. (1994). A statistical approach to the Earth's main magnetic field. *Phys. Earth Planet. Inter.*, 82:167–183.

Hunten, D. M., Shemansky, D. E., and Morgan, T. H. (1988). *The Mercury atmosphere*, pages 562–612.

Johnson, C. L., Purucker, M. E., Korth, H., Anderson, B. J., Winslow, R. M., Al Asad, M. M. H., Slavin, J. A., Alexeev, I. I., Phillips, R. J., Zuber, M. T., and Solomon, S. C. (2012). MESSENGER observations of Mercury's magnetic field structure. *J. Geophys. Res.*, 117:E00L14.

Katanforoush, A. and Shahshahani, M. (2003). Distributing Points on the Sphere. *Experimental Mathematics*, 12:199–209.

Kutzner, C. and Christensen, U. R. (2002). From stable dipolar towards reversing numerical dynamos. *Phys. Earth Planet. Inter.*, 131:29–45.

Langel, R. A. (1987). *The Main Field. In: Geomagnetism, Vol. I, pp. 249–512*. ed. J. A. Jacobs, Academic Press.

Langlais, B. and Purucker, M. (2007). A polar magnetic paleopole associated with Apollinaris Patera, Mars. *Planet. Space Sci.*, 55:270–279.

Langlais, B., Purucker, M. E., and Mandea, M. (2004). Crustal magnetic field of Mars. *J. Geophys. Res.*, 109:E02008.

Lewis, J. S. (1972). Metal/silicate fractionation in the Solar System. *Earth and Planet. Sci. Lett.*, 15:286–290.

Lhuillier, F., Aubert, J., and Hulot, G. (2011). Earth's dynamo limit of predictability controlled by magnetic dissipation. *Geophys. J. Int.*, 186:492–508.

Margot, J. L., Peale, S. J., Jurgens, R. F., Slade, M. A., and Holin, I. V. (2007). Large Longitude Libration of Mercury Reveals a Molten Core. *Science*, 316:710–714.

Maus, S., Rother, M., Stolle, C., Mai, W., Choi, S., Lühr, H., Cooke, D., and Roth, C. (2006). Third generation of the Potsdam Magnetic Model of the Earth (POMME). *J. Geophys. Res.*, 7:7008.

Mayhew, M. A. (1979). Inversion of satellite magnetic anomaly data. *J. Geophys.*, 45:119–128.

McAdams, J. V., Bryan, C. G., Moessner, D. P., Page, B. R., Stanbridge, D. R., and Williams, K. E. (2014). Orbit design and navigation through the end of MESSENGER's extended mission at Mercury. *24th Space Flight Mechanics Meeting, American Astronautical Society/American Institute of Aeronautics and Astronautics, paper AAS 14-369, 20 pp., Santa Fe, NM*, page 20pp.

Melosh, H. J. and McKinnon, W. B. (1988). *The tectonics of Mercury*, pages 374–400.

Merrill, R. T., McElhinny, W., and McFadden, P. (1998). *The Magnetic Field of the Earth: Paleomagnetism, the Core, and the Deep Mantle*. International geophysics series. Academic Press.

Murray, B. C., Belton, M. J. S., Danielson, G. E., Davies, M. E., Gault, D., Hapke, B., O'Leary, B., Strom, R. G., Suomi, V., and Trask, N. (1974). Mariner 10 Pictures of Mercury: First Results. *Science*, 184:459–461.

Ness, N. F., Behannon, K. W., Lepping, R. P., and Whang, Y. C. (1975). The magnetic field of Mercury. I. *J. Geophys. Res.*, 80:2708–2716.

Ness, N. F., Behannon, K. W., Lepping, R. P., Whang, Y. C., and Schatten, K. H. (1974).

Magnetic Field Observations near Mercury: Preliminary Results from Mariner 10. *Science*, 185:151–160.

Nimmo, F. and Watters, T. R. (2004). Depth of faulting on Mercury: Implications for heat flux and crustal and effective elastic thickness. *Geophys. Reas. Lett.*, 31:2701.

O'Shaughnessy, D. J., McAdams, J. V., Bedini, P. D., Calloway, A. B., Williams, K. E., and Page, B. R. (2014). MESSENGER's use of solar sailing for cost and risk reduction. *Acta Astronautica*, 93:483–489.

Philpott, L. C., Johnson, C. L., Winslow, R. M., Anderson, B. J., Korth, H., Purucker, M. E., and Solomon, S. C. (2014). Constraints on the secular variation of Mercury's magnetic field from the combined analysis of MESSENGER and Mariner 10 data. *Geophys. Res. Lett.*, 41:6627–6634.

Pike, R. J. (1976). Crater dimensions from Apollo data and supplemental sources. *Moon*, 15:463–477.

Pike, R. J. (1988). *Geomorphology of impact craters on Mercury*, pages 165–273.

Plagemann, S. (1965). Model of the Internal Constitution and Temperature of the Planet Mercury. *J. Geophys. Res.*, 70:985–993.

Potter, A. and Morgan, T. (1985). Discovery of sodium in the atmosphere of Mercury. *Science*, 229:651–653.

Potter, A. E. and Morgan, T. H. (1986). Potassium in the atmosphere of Mercury. *Icarus*, 67:336–340.

Press, W. H., Flannery, B. P., Teukolsky, S. A., and Vetterling, W. T. (1989). *Numerical recipes in Pascal. The art of scientific computing*.

Purucker, M., Langlais, B., Olsen, N., Hulot, G., and Mandea, M. (2002). The southern edge of cratonic North America: Evidence from new satellite magnetometer observations. *Geophys. Res. Lett.*, 29:56–1 – 56–4.

Purucker, M., Ravat, D., Frey, H., Voorhies, C., Sabaka, T., and Acuña, M. (2000). An altitude-normalized magnetic map of Mars and its interpretation. *Geophys. Res. Lett.*, 27:2449–2452.

Purucker, M. E., Head, III, J. W., and Wilson, L. (2012). Magnetic signature of the lunar South Pole-Aitken basin: Character, origin, and age. *J. Geophys. Res.*, 117:5001.

Purucker, M. E., Langel, R. A., Rajaram, M., and Raymond, C. (1998). Global magnetization models with a priori information. *J. Geophys. Res.*, 103:2563–2584.

Purucker, M. E., Sabaka, T. J., and Langel, R. A. (1996). Conjugate gradient analysis: A new tool for studying satellite magnetic data sets. *Geophys. Res. Lett.*, 23:507–510.

Purucker, M. E., Sabaka, T. J., Solomon, S. C., Anderson, B. J., Korth, H., Zuber, M. T., and Neumann, G. A. (2009). Mercury's internal magnetic field: Constraints on large- and small-scale fields of crustal origin. *Earth and Planet. Sci. Lett.*, 285:340–346.

Rivoldini, A. and Van Hoolst, T. (2013). The interior structure of Mercury constrained by the low-degree gravity field and the rotation of Mercury. *Earth Planet. Sci. Lett.*, 377:62–72.

Russell, C. T. (1977). On the relative locations of the bow shocks of the terrestrial planets. *Geophys. Res. Lett.*, 4:387–390.

Russell, C. T., Baker, D. N., and Slavin, J. A. (1988). *The magnetosphere of Mercury*, pages 514–561.

Santo, A. G., Gold, R. E., McNutt, R. L., Solomon, S. C., Ercol, C. J., Farquhar, R. W., Hartka, T. J., Jenkins, J. E., McAdams, J. V., Mosher, L. E., Persons, D. F., Artis, D. A., Bokulic, R. S., Conde, R. F., Dakermanji, G., Goss, M. E., Haley, D. R., Heeres, K. J., Maurer, R. H., Moore, R. C., Rodberg, E. H., Stern, T. G., Wiley, S. R., Williams, B. G., Yen, C.-w. L., and Peterson, M. R. (2001). The MESSENGER mission to Mercury: spacecraft and mission design. *Planet. Space Sci.*, 49:1481–1500.

Schubert, G., Chan, K. H., Liao, X., and Zhang, K. (2004). Planetary dynamos: effects of electrically conducting flows overlying turbulent regions of magnetic field generation. *Icarus*, 172:305–315.

Siscoe, G. L., Ness, N. F., and Yeates, C. M. (1975). Substorms on Mercury. *J. Geophy. Res.*, 80:4359–4363.

Slavin, J. A., Acuña, M. H., Anderson, B. J., Baker, D. N., Benna, M., Boardsen, S. A., Gloeckler, G., Gold, R. E., Ho, G. C., Korth, H., Krimigis, S. M., McNutt, R. L., Raines, J. M., Sarantos, M., Schriver, D., Solomon, S. C., Trávníček, P., and Zurbuchen, T. H. (2009). MESSENGER Observations of Magnetic Reconnection in Mercury's Magnetosphere. *Science*, 324:606–610.

Slavin, J. A., Acuña, M. H., Anderson, B. J., Baker, D. N., Benna, M., Gloeckler, G., Gold, R. E., Ho, G. C., Killen, R. M., Korth, H., Krimigis, S. M., McNutt, R. L., Nittler, L. R., Raines, J. M., Schriver, D., Solomon, S. C., Starr, R. D., Trávníček, P., and Zurbuchen, T. H. (2008). Mercury's Magnetosphere After MESSENGER's First Flyby. *Science*, 321:85–.

Slavin, J. A., Krimigis, S. M., Acuña, M. H., Anderson, B. J., Baker, D. N., Koehn, P. L., Korth, H., Livi, S., Mauk, B. H., Solomon, S. C., and Zurbuchen, T. H. (2007). MESSENGER: Exploring Mercury's Magnetosphere. *Space Sci. Rev.*, 131:133–160.

Smith, D. E., Zuber, M. T., Phillips, R. J., Solomon, S. C., Hauck, S. A., Lemoine, F. G., Mazarico, E., Neumann, G. A., Peale, S. J., Margot, J.-L., Johnson, C. L., Torrence, M. H., Perry, M. E., Rowlands, D. D., Goossens, S., Head, J. W., and Taylor, A. H. (2012). Gravity Field and Internal Structure of Mercury from MESSENGER. *Science*, 336:214–217.

Solomon, S. C., McNutt, R. L., Gold, R. E., Acuña, M. H., Baker, D. N., Boynton, W. V., Chapman, C. R., Cheng, A. F., Gloeckler, G., Head, III, J. W., Krimigis, S. M., McClintock, W. E., Murchie, S. L., Peale, S. J., Phillips, R. J., Robinson, M. S., Slavin,

J. A., Smith, D. E., Strom, R. G., Trombka, J. I., and Zuber, M. T. (2001). The MESSENGER mission to Mercury: scientific objectives and implementation. *Planet. Space Sci.*, 49:1445–1465.

Sprague, A., Warell, J., Cremonese, G., Langevin, Y., Helbert, J., Wurz, P., Veselovsky, I., Orsini, S., and Milillo, A. (2007). Mercury's Surface Composition and Character as Measured by Ground-Based Observations. *Space Sci. Rev.*, 132:399–431.

Stanley, S., Bloxham, J., Hutchison, W. E., and Zuber, M. T. (2005). Thin shell dynamo models consistent with Mercury's weak observed magnetic field [rapid communication]. *Earth Planet. Sci. Lett.*, 234:27–38.

Stanley, S., Elkins-Tanton, L., Zuber, M. T., and Parmentier, E. M. (2008). Mars' Paleomagnetic Field as the Result of a Single-Hemisphere Dynamo. *Science*, 321:1822–1825.

Stevenson, D. J. (1980). Saturn's luminosity and magnetism. *Science*, 208:746–748.

Stevenson, D. J. (1982). Reducing the non-axisymmetry of a planetary dynamo and an application to Saturn. *Geophys. Astrophys. Fluid Dyn.*, 21:113–127.

Stevenson, D. J. (1987). Mercury's magnetic field - A thermoelectric dynamo? *Earth Planet. Sci. Lett.*, 82:114–120.

Strom, R. G. and Sprague, A. L. (2003). *Exploring Mercury. The iron planet*. Springer. ISBN 1-85233-731-1.

Strom, R. G., Trask, N. J., and Guest, J. E. (1975). Tectonism and volcanism on Mercury. *J. Geophys. Res.*, 80:2478–2507.

Takahashi, F. and Matsushima, M. (2006). Dipolar and non-dipolar dynamos in a thin shell geometry with implications for the magnetic field of Mercury. *Geophys. Res. Lett.*, 33:10202.

Thébault, E., Schott, J. J., and Mandea, M. (2006). Revised spherical cap harmonic analysis (R-SCHA): Validation and properties. *J. Geophys. Res.*, 111.

Thomas, P. G. (1997). Are there other tectonics than tidal despinning, global contraction and Caloris related events on Mercury? A review of questions and problems. *Planet. Space Sci.*, 45:3.

Thomas, P. G., Masson, P., and Fleitout, L. (1988). *Tectonic history of Mercury*, pages 401–428.

Tsyganenko, N. A. and Sitnov, M. I. (2005). Modeling the dynamics of the inner magnetosphere during strong geomagnetic storms. *J. Geophys. Res.*, 110:A03208.

Uno, H., Anderson, B. J., Korth, H., Johnson, C. L., and Solomon, S. C. (2009). Modeling Mercury's internal magnetic field with smooth inversions. *Earth Planet. Sci. Lett.*, pages 328–339.

van Hoolst, T., Sohl, F., Holin, I., Verhoeven, O., Dehant, V., and Spohn, T. (2007). Mercury's Interior Structure, Rotation, and Tides. *Space Sci. Rev.*, 132:203–227.

Verhoeven, O., Tarits, P., Vacher, P., Rivoldini, A., and van Hoolst, T. (2009). Composition and formation of Mercury: Constraints from future electrical conductivity measurements. *Planet. Space Sci.*, 57:296–305.

Vilim, R., Stanley, S., and Hauck, S. A. (2010). Iron snow zones as a mechanism for generating Mercury's weak observed magnetic field. *J. Geophy. Res. (Planets)*, 115:11003.

von Frese, R. R. B., Hinze, W. J., and Braile, L. W. (1981). Spherical earth gravity and magnetic anomaly analysis by equivalent point source inversion. *Earth Planet. Sci. Lett.*, 53:69–83.

Whaler, K. A. and Purucker, M. E. (2005). A spatially continuous magnetization model for Mars. *J. Geophys. Res.*, 110:9001.

Whang, Y. C. (1977). Magnetospheric magnetic field of Mercury. *J. Geophys. Res.*, 82:1024–1030.

Wicht, J. and Heyner, D. (2014). Mercury's magentic field in the messenger era. In Shuanggen, J., editor, *Planetary Geodesy and Remote Sensing*, pages 223 – 262. CRC Press.

Wicht, J., Mandea, M., Takahashi, F., Christensen, U. R., Matsushima, M., and Langlais, B. (2007). The Origin of Mercury's Internal Magnetic Field. *Space Sci. Rev.*, 132:261–290.

Wurz, P. and Blomberg, L. (2001). Particle populations in Mercury's magnetosphere. *Planet. Space Sci.*, 49:1643–1653.

LE CHAMP MAGNÉTIQUE DE MERCURE TEL QUE MESURÉ PAR LA SONDE MESSENGER

Les mesures du champ magnétique herméen acquises au-dessus de l'hémisphère Nord par la sonde MESSENGER fournissent des informations cruciales sur le champ magnétique de la planète. La méthode des Time-Dependent Equivalent Source Dipole est développée afin de modéliser le champ magnétique et sa variation séculaire avec des mesures distribuées sur une région restreinte. Les tests avec des données synthétiques à la fois sur des grilles régulières et aux positions de la sonde confirment la validité de la méthode. Elle est appliquée à des mesures de MESSENGER acquises sur presque trois années terrestres. En excluant les termes de variation séculaire, des modèles journaliers sidéraux et solaires du champ magnétique herméen sont calculés. Un champ zonal dominant avec des structures de petite échelle, non-axisymétriques, et en rotation avec le Soleil dans un référentiel centré sur Mercure est trouvé dans les modèles basés sur un jour sidéral. Lorsque l'on modélise le champ durant un jour solaire complet, ces structures de petite échelle diminuent et le champ devient encore plus axisymétrique. Cependant, la comparaison des différents modèles jour solaire révèle une forte variabilité. L'absence de structures non-axisymétriques cohérentes modélisées par notre méthode, pourtant développée pour permettre de modéliser de telles structures, prouve la structure de grande échelle et quasi axisymétrique du champ magnétique interne de Mercure.

Mots clés : Champ magnétique planétaire, Mercure, mission MESSENGER, Méthode TD-ESD, Modèle journalier sidéral, Modèle journalier solaire, Analyse de données, Mesures satellitaires.

THE MAGNETIC FIELD OF MERCURY AS MEASURED BY THE MESSENGER SPACECRAFT

Studying planetary magnetic fields may bring clues for understanding the physical processes of a planetary interior. Mercury is the only terrestrial planet (except the Earth) that has a core dynamo that generates a global magnetic field. Hermean magnetic field measurements acquired over the northern hemisphere by the MESSENGER spacecraft provide crucial information on the magnetic field of the planet. The Time-Dependent Equivalent Source Dipole method is developed here to model magnetic field and possible secular variation with measurements distributed over a limited spatial region. Tests with synthetic data distributed on regular grids as well as at spacecraft positions confirm the validity of the method. The method is applied to almost three terrestrial years of MESSENGER measurements. Ignoring the secular variation terms, sidereal and solar day Hermean field models are computed and interpreted. A dominantly zonal field with small-scale non axisymmetric features co-rotating with the Sun in Mercury Body Fixed is found in the sidereal day models. When modeling the field during one complete solar day, these small-scale features decrease and the field becomes even more axisymmetric. However, comparing different solar day models reveal a strong variability. The lack of any coherent non-axisymmetric feature recovered by our method, which was designed to allow for such small-scale structures, provides strong evidence for the large-scale and close-to-axisymmetry structure of the internal magnetic field of Mercury.

Key-words: Planetary magnetic field, Mercury, MESSENGER mission, Sidereal day model, Solar day model, Axisymmetric field, Data analysis, Satellite measurements.